REPORT DOCUMENTATION PAGE

Form Approved OMB NO. 0704-0188

1. REPORT DATE (DD-MM-YYYY)	2. REPORT TYPE	3. DATES COVERED (From - To)
12-01-2022	Final Report	1-Jun-2019 - 31-May-2020

4. TITLE AND SUBTITLE
Final Report: Organically Controlled Crystal Growth and Phase Selection in Ecologically Diverse, Ultrahard Bio-composites

5a. CONTRACT NUMBER
W911NF-19-1-0347

5b. GRANT NUMBER

5c. PROGRAM ELEMENT NUMBER
611102

6. AUTHORS

5d. PROJECT NUMBER

5e. TASK NUMBER

5f. WORK UNIT NUMBER

7. PERFORMING ORGANIZATION NAMES AND ADDRESSES
University of California - Riverside
200 University Office Building

Riverside, CA 92521 -0001

8. PERFORMING ORGANIZATION REPORT NUMBER

9. SPONSORING/MONITORING AGENCY NAME(S) AND ADDRESS (ES)
U.S. Army Research Office
P.O. Box 12211
Research Triangle Park, NC 27709-2211

10. SPONSOR/MONITOR'S ACRONYM(S)
ARO

11. SPONSOR/MONITOR'S REPORT NUMBER(S)
73232-LS-H.3

12. DISTRIBUTION AVAILIBILITY STATEMENT
Approved for public release; distribution is unlimited.

13. SUPPLEMENTARY NOTES
The views, opinions and/or findings contained in this report are those of the author(s) and should not contrued as an official Department of the Army position, policy or decision, unless so designated by other documentation.

14. ABSTRACT

15. SUBJECT TERMS

16. SECURITY CLASSIFICATION OF:			17. LIMITATION OF ABSTRACT	15. NUMBER OF PAGES	19a. NAME OF RESPONSIBLE PERSON
a. REPORT	b. ABSTRACT	c. THIS PAGE			David Kisailus
UU	UU	UU	UU		19b. TELEPHONE NUMBER 951-827-4310

RPPR Final Report
as of 19-Jan-2022

Agency Code: 21XD

Proposal Number: 73232LSH **Agreement Number: W911NF-19-1-0347**
INVESTIGATOR(S):

Name: David Kisailus
Email: kisailus@ucr.edu
Phone Number: 9518274310
Principal: Y

Organization: **University of California - Riverside**
Address: 200 University Office Building, Riverside, CA 925210001
Country: USA
DUNS Number: 627797426 EIN: 956006142
Report Date: 31-Aug-2020 Date Received: 12-Jan-2022
Final Report for Period Beginning 01-Jun-2019 and Ending 31-May-2020
Title: Organically Controlled Crystal Growth and Phase Selection in Ecologically Diverse, Ultrahard Bio-composites
Begin Performance Period: 01-Jun-2019 **End Performance Period:** 31-May-2020
Report Term: 0-Other
Submitted By: David Kisailus Email: kisailus@ucr.edu
Phone: (951) 827-4310
Distribution Statement: 1-Approved for public release; distribution is unlimited.

STEM Degrees: **STEM Participants:**

Major Goals: The overall objectives of the project are to investigate the multiscale organic and mineral components of the radular teeth and, if time allows, the supporting flexible styli from an ecologically diverse selection of chiton. These investigations will include chemical, molecular (i.e., protein) and phase composition in order to reveal how the organic substructure regulates (i) pathways for mineral transport, (ii) phase selection and (iii) mineral nucleation and growth. The information gleaned from these investigations will be used to provide both design and synthesis platforms for advanced materials. Based on our preliminary data, we believe that through the careful control of organic synthesis and hierarchical assembly, the local and global architectures of inorganic / organic composite can be modulated to increase the damage tolerance of these ultrahard materials while also providing utility. We will examine the teeth and stylus from C. stelleri (both from Monterey, CA and Hokkaido, Japan), C. articulatus and C. japonicus as outlined according to the following objectives:
1. Resolve the multiscale (nano to mm-scale) structural features of the mature monocuspid and tricuspid teeth of chitons using microscopy and spectroscopy.
2. Probe the immature teeth from the chitons in order to derive microstructural and phase evolution pathways. Investigate the underlying organic framework (structural and chemical) that controls phase selection and regulates nucleation and growth of mineral in the teeth.
3. Conduct comparative genome, transcriptome and proteome analyses in order to understand a universal biomineralization system in chitons controlled by functional proteins (e.g., ion transporter, mineral nucleating, etc.). If time allows, confirm protein functions using localization studies and gene knock down.
4. Perform bio-inspired syntheses and in-vitro crystallization studies that validate organic-mineral interactions and translate to material architectures with potential for unique or enhanced performance.

Accomplishments: During this project, we were initially making progress in staying on schedule and achieving the milestones outlined in the proposal. However, during the later half of the year, the labs were shut down due to COVID-19. Regardless, we managed to finish one manuscript on using two complementary quantum magnetic microscopy methods, based on nitrogen-vacancy centers in diamond, to spatially map the mineral phases ferrihydrite and magnetite in the developing teeth of Acanthopleura hirtosa. We also are getting close to finishing another manuscript that focuses on the macrostructural architecture, the regional organic and inorganic materials and elemental distribution and subsequent nano-mechanical properties of the stylus from the Northern Pacific dwelling Cryptochiton stelleri. In this work, we used a combination of μ-CT imaging, optical and electron microscopy, as well as elemental analysis, to reveal that the stylus is a highly contoured tube, mainly composed of alpha-chitin fibers, with a complex density distribution. Nanoindentation reveals regiospecific and graded mechanical properties that can be correlated with both the elemental composition and material distribution. Finite

element modeling shows that the unique macroscale architecture, material distribution and elemental gradients have been optimized to preserve the structural stability of this flexible, yet robust functionally-graded fiber-reinforced composite tube, providing effective function during rasping. Beyond this, we uncovered that the stylus is likely a conduit through which mineral is transported into the tooth. In addition, we have spent a significant amount of time (while the labs were open) investigating the mechanisms of organically assisted/templating of iron oxides and their subsequent phase transformation from ferrihydrite to magnetite.

Training Opportunities: 1. Mr. Taifeng Wang, was a Ph.D. student working on the project. He was mentored by Kisailus.

2. Dr. Anna Pohl was a postdoc partially supported on this project. She was mentored by Kisailus.
We have had both high school and community college students tour our lab in the past year (until February 2020).

3. Julia M. McCoey and Robert W. de Gille were Ph.D. students who I helped to mentor during this project. They are at the University of Melbourne.

Dr. Michiko Nemoto is a former Kisailus post-doc and now a collaborator in this project. She is now a professor at Okayama University. She was mentored as a professor by Kisailus.

RPPR Final Report
as of 19-Jan-2022

Results Dissemination: Publications:
“Multiscale toughening mechanisms in biological materials and bioinspired designs,” W. Huang, D. Restrepo, J.Y. Jung, F.Y. Su, Z. Liu, R.O. Ritchie, J. McKittrick, P. Zavattieri, D. Kisailus, Advanced Materials, 31 (43) (2019) 1901561. DOI: 10.1002/adma.201901561

“Quantum magnetic imaging of iron biomineralisation in teeth of the chiton Acanthopleura hirtosa," J. McCoey, M. Matsuoka, R. de Gille, L. Hall, J. Shaw, J.P. Tetienne, D. Kisailus, L. Hollenberg, D. Simpson, Small Methods, 4 (3) (2019) 2070010. DOI: 10.1002/smtd.201900754

One manuscript is in review:
“Radular Stylus of Cryptochiton stelleri: A Multifunctional Lightweight and Flexible Fiber-Reinforced Composite,” Anna Pohl, Steven A. Herrera, David Restrepo, Ryo Negishi, Jae-Young Jung, Chris Salinas, Richard Wuhrer, Tomoko Yoshino, Joanna McKittrick, Atsushi Arakaki, Michiko Nemoto, Pablo Zavattieri, David Kisailus, Journal of the Mechanical Behavior of Biomedical Materials, in review.

One additional manuscript is in preparation.

Presentations:

“Synthesis, Phase Transformation and Structural Development in Magnetic Biocomposites”, Invited talk. Materials Research Society Spring Meeting, Phoenix, AZ, April 15, 2020.

“Biological Crystallization of Ultrahard Teeth and Translation to Multi-functional Materials”, Invited talk. The Minerals, Metals and Materials Society Annual Meeting, San Diego, CA, February 26, 2020.

“Multiscale Architectures in the Exoskeletal Armor of a Crush Resistant Insect”, Invited talk. The Minerals, Metals and Materials Society Annual Meeting, San Diego, CA, February 24, 2020.

“Biologically Inspired Multi-Functional Materials,” Invited seminar. Lawrence Livermore National Labs. Livermore, CA. February 14, 2020.

“The Tooth-Stylus-Belt Radula System of Chitons: an Inspiration for Multimaterial and Multifunctional Structures,” Gordon Research Conference on Multifunctional Materials. Ventura, CA. January 19-24, 2020.

“Phase Transformation of Iron-based Mineral in the Ultrahard and Wear-resistant Teeth of Cryptochiton Stelleri,” Gordon Research Conference on Multifunctional Materials. Ventura, CA. January 19-24, 2020.

“Biological Synthesis and Mechanics of Ecologically Diverse Ultrahard Teeth of Chitons,” Invited talk. 8th International Conference on Mechanics of Biological Materials. Waikoloa Beach, Hawaii. December 15 – 19, 2019.

“Biological Synthesis and Mechanics of Ecologically Diverse Ultrahard Teeth of Chitons,” Invited talk. Joint Conference of the 12th International Marine Biotechnology Conference and the 12th Asia Pacific Marine Biotechnology Conference. Shizuoka, Japan. September 9 – 13, 2019.

“Biologically Inspired Multi-Functional Composites,” Invited talk. 10th Pacific Rim International Conference on Advanced Materials and Processing (PRICM10). Xian, China. August 18-22, 2019.

“Biological Crystallization of Ultrahard Teeth and Translation to Multi-Functional Materials,” Invited talk. 19th International Conference on Crystal Growth and Epitaxy (ICCGE-19). Keystone, Colorado, July 28–August 2, 2019.

“Biological Crystallization of Ultrahard Teeth and Translation to Multi-Functional Materials,” Invited talk. Collaborative Conference on Materials Research. Seoul, South Korea. June 25-29, 2019.

Honors and Awards: Nothing to Report

Protocol Activity Status:

Technology Transfer: Nothing to Report

RPPR Final Report
as of 19-Jan-2022

PARTICIPANTS:

Participant Type: PD/PI
Participant: David Kisailus
Person Months Worked: 1.00 **Funding Support:**
Project Contribution:
National Academy Member: N

Participant Type: Graduate Student (research assistant)
Participant: Taifeng Wang
Person Months Worked: 12.00 **Funding Support:**
Project Contribution:
National Academy Member: N

Participant Type: Postdoctoral (scholar, fellow or other postdoctoral position)
Participant: Anna Pohl
Person Months Worked: 3.00 **Funding Support:**
Project Contribution:
National Academy Member: N

ARTICLES:

Publication Type: Journal Article Peer Reviewed: Y **Publication Status:** 1-Published
Journal: Advanced Materials
Publication Identifier Type: DOI Publication Identifier: 10.1002/adma.201901561
Volume: 31 Issue: 43 First Page #: 1901561
Date Submitted: 1/12/22 12:00AM Date Published: 7/1/19 7:00AM
Publication Location:
Article Title: Multiscale Toughening Mechanisms in Biological Materials and Bioinspired Designs
Authors: Wei Huang, David Restrepo, Jae?Young Jung, Frances Y. Su, Zengqian Liu, Robert O. Ritchie, Joanna
Keywords: Biological materials; multiscale; toughening mechanisms; computational modeling; bioinspired designs
Abstract: Biological materials found in Nature such as nacre and bone are well recognized as light weight, strong and tough structural materials. The remarkable toughness and damage tolerance of such biological materials are conferred through hierarchical assembly of their multiscale (i.e., atomic- to macro-scale) architectures and components. In the current work, the toughening mechanisms of different organisms at multi-length scales are identified and summarized: macromolecular deformation, chemical bond breakage and biomineral crystal imperfections at the atomic scale; biopolymer fibril reconfiguration/deformation and biomineral nanoparticle/nanoplatelet/nanorod translation and crack reorientation at the nanoscale; crack deflection and twisting by characteristic features such as tubules and lamellae at the microscale; structure and morphology optimization at the macroscale.
Distribution Statement: 1-Approved for public release; distribution is unlimited.
Acknowledged Federal Support: **Y**

RPPR Final Report
as of 19-Jan-2022

Publication Type: Journal Article Peer Reviewed: Y **Publication Status:** 1-Published
Journal: Small Methods
Publication Identifier Type: DOI Publication Identifier: 10.1002/smtd.201900754
Volume: 4 Issue: 3 First Page #: 1900754
Date Submitted: 1/12/22 12:00AM Date Published: 1/1/20 8:00AM
Publication Location:
Article Title: Quantum Magnetic Imaging of Iron Biomineralization in Teeth of the Chiton
Authors: Julia M. McCoey, Mirai Matsuoka, Robert W. Gille, Liam T. Hall, Jeremy A. Shaw, Jean?Philippe Tetienı
Keywords: biomineralisation, diamond, magnetic imaging, chiton, nitrogen-vacancy
Abstract: Iron is critical for life. Nature capitalises on the physical attributes of iron biominerals for functional, structural and sensory applications. Iron biomineralisation is well exemplified by the magnetite-bearing radula of chitons, the hardest known biomineral of any animal. Although magnetism is an integral property of iron biominerals, limited information exists on the magnetic state, structure and orientation of these nanoscale materials during mineralisation. The advent of quantum based magnetic microscopy provides a new avenue to probe these biological systems directly, providing detailed magnetic information of the iron oxide structures. Here we apply two complementary quantum magnetic microscopy methods, based on nitrogen-vacancy centers in diamond, to spatially map the mineral phases ferrihydrite and magnetite in the developing teeth of Acanthopleura hirtosa.
Distribution Statement: 1-Approved for public release; distribution is unlimited.
Acknowledged Federal Support: **Y**

Partners

,

Julia M. McCoey and Robert W. de Gille were Ph.D. students who I helped to mentor during this project. They are a

I certify that the information in the report is complete and accurate:
Signature: David Kisailus
Signature Date: 1/12/22 11:54PM

ARO Final Report

Organically Controlled Crystal Growth and Phase Selection in Ecologically Diverse, Ultrahard Bio-composites

Period of Performance: June 1, 2019 - May 31, 2020

PI: David Kisailus, UC Riverside
Program Manager: Dr. Stephanie McElhinny, Biochemistry, Life Sciences Division

Abstract

During this project, we were initially making progress in staying on schedule and achieving the milestones outlined in the proposal. However, during the later half of the year, the labs were shut down due to COVID-19. Regardless, we managed to finish one manuscript on using two complementary quantum magnetic microscopy methods, based on nitrogen-vacancy centers in diamond, to spatially map the mineral phases ferrihydrite and magnetite in the developing teeth of Acanthopleura hirtosa. We also are getting close to finishing another manuscript that focuses on the macrostructural architecture, the regional organic and inorganic materials and elemental distribution and subsequent nano-mechanical properties of the stylus from the Northern Pacific dwelling *Cryptochiton stelleri*. In this work, we used a combination of μ-CT imaging, optical and electron microscopy, as well as elemental analysis, to reveal that the stylus is a highly contoured tube, mainly composed of alpha-chitin fibers, with a complex density distribution. Nanoindentation reveals regiospecific and graded mechanical properties that can be correlated with both the elemental composition and material distribution. Finite element modeling shows that the unique macroscale architecture, material distribution and elemental gradients have been optimized to preserve the structural stability of this flexible, yet robust functionally-graded fiber-reinforced composite tube, providing effective function during rasping. Beyond this, we uncovered that the stylus is likely a conduit through which mineral is transported into the tooth. In addition, we have spent a significant amount of time (while the labs were open) investigating the mechanisms of organically assisted/templating of iron oxides and their subsequent phase transformation from ferrihydrite to magnetite.

Overall objectives

The overall objectives of the project are to investigate the multiscale organic and mineral components of the radular teeth and, if time allows, the supporting flexible styli from an ecologically diverse selection of chiton. These investigations will include chemical, molecular (i.e., protein) and phase composition in order to reveal how the organic substructure regulates (i) pathways for mineral transport, (ii) phase selection and (iii) mineral nucleation and growth. The information gleaned from these investigations will be used to provide both design and synthesis platforms for advanced materials. Based on our preliminary data, we believe that through the

careful control of organic synthesis and hierarchical assembly, the local and global architectures of inorganic / organic composite can be modulated to increase the damage tolerance of these ultrahard materials while also providing utility. We will examine the teeth and stylus from *C. stelleri* (both from Monterey, CA and Hokkaido, Japan), *C. articulatus* and *C. japonicus* as outlined according to the following objectives:

1. Resolve the multiscale (nano to mm-scale) structural features of the mature monocuspid and tricuspid teeth of chitons using microscopy and spectroscopy.
2. Probe the immature teeth from the chitons in order to derive microstructural and phase evolution pathways. Investigate the underlying organic framework (structural and chemical) that controls phase selection and regulates nucleation and growth of mineral in the teeth.
3. Conduct comparative genome, transcriptome and proteome analyses in order to understand a universal biomineralization system in chitons controlled by functional proteins (e.g., ion transporter, mineral nucleating, etc.). If time allows, confirm protein functions using localization studies and gene knock down.
4. Perform bio-inspired syntheses and in-vitro crystallization studies that validate organic-mineral interactions and translate to material architectures with potential for unique or enhanced performance.

Throughout this brief project, we have made significant progress towards our objectives, even with the COVID-19 interruptions.

Accomplishments of Specific objectives:

1. Resolve the multiscale (nano to mm-scale) structural features of the mature monocuspid and tricuspid teeth of chitons using microscopy and spectroscopy.

During the past year, we used microscopic techniques to investigate the tooth architectures within the teeth of both *C. stelleri* and *C. articulatus*.

We had already known that the shell region of the tooth from C. stelleri consists of magnetite nanorods that are primarily aligned with the long axis of the cusp as well as magnetite nanoparticles on the outermost region of the leading edge. In the past year, we have conducted additional analysis of the structural features of these teeth using primarily TEM with some SEM. The SEM micrograph of the leading edge of the tooth shows that the particles are only on the first 2 µm of the tooth.

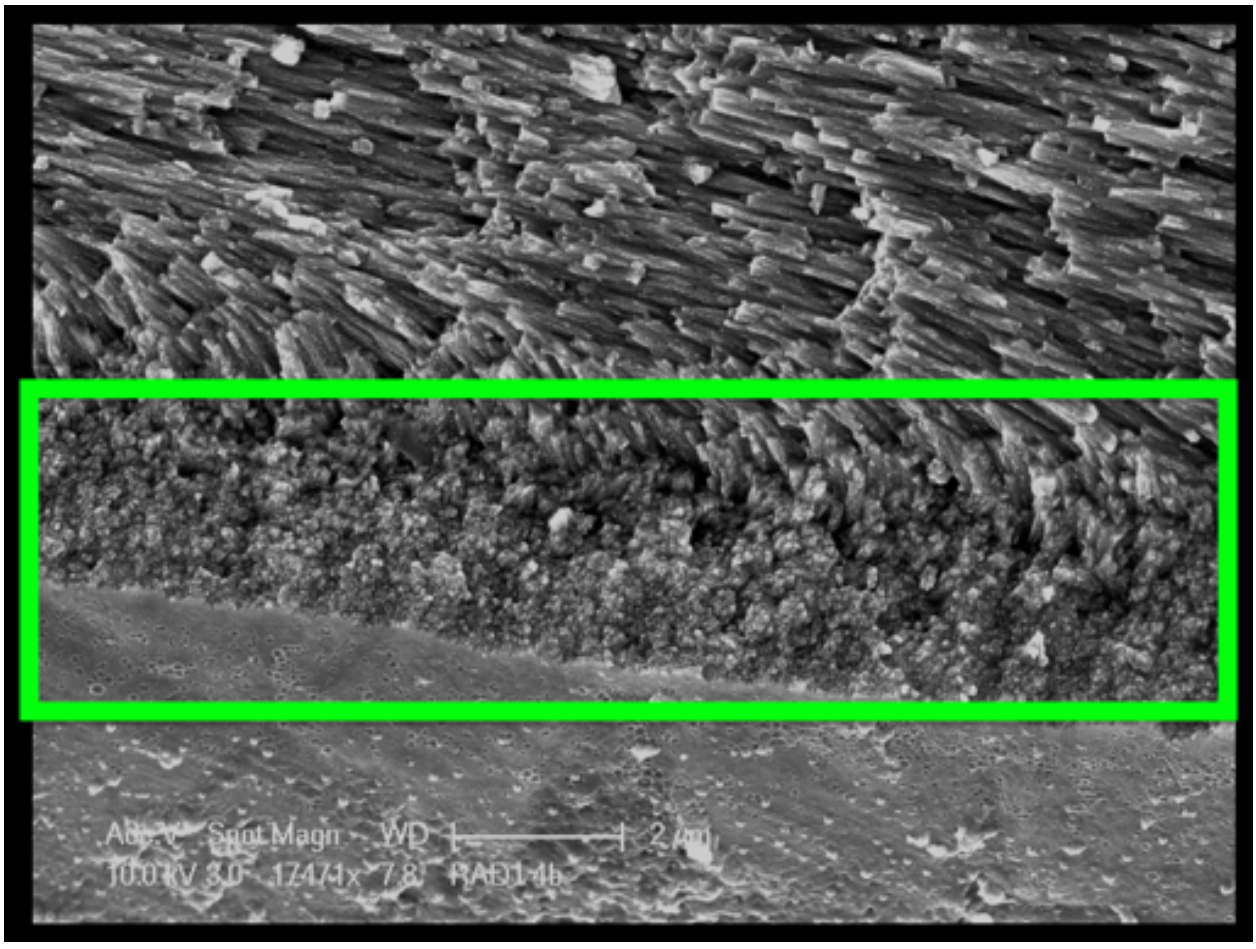

[SEM of leading edge of C. stelleri fully mineralized tooth, highlighting particle region.]

TEM analyses of FIB-sectioned teeth within this particle region actually showed a number of structural features that were previously unknown. First, there seems to be a gradient of particle

sizes, increasing from the leading edge (~ 8nm) inwards to the interface with the rod region (~60 nm).

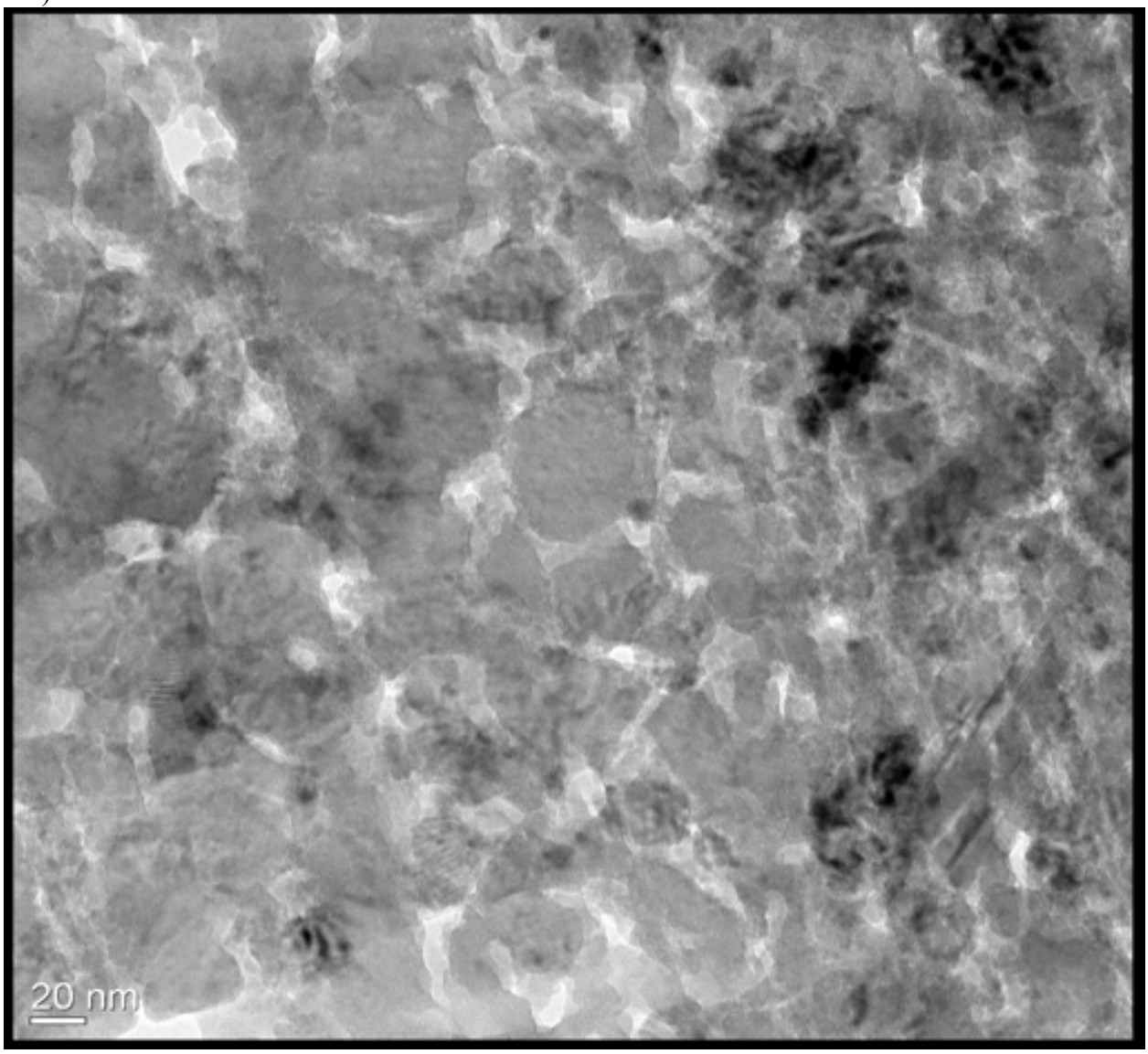

[TEM of leading edge of C. stelleri fully mineralized tooth, highlighting particle region. Left side is deeper within tooth with larger particles, while right side of micrograph is towards the outer periphery of the tooth.]

Further analyses within this particle region underscored the presence of pores around the particles. This, in combination with previous observations of chitin in immature teeth suggests organic material (likely chitin with protein) that acts as a template, but with no apparent orientation.

In addition, the observation of this particle coating on the edge of a structure that is subjected to high stresses is not unique. We have observed this in other organisms, specifically the dactyl club of the mantis shrimp. Modeling of the role of these coatings, where the elastic modulus ratio between organic and mineral determines the depth at which stress can penetrate. The models show that when the modulus ratio is greater than 1:100 (i.e., modulus of organic to modulus of mineral),

all stress is confined to the surface. Thus, the organic phase is critical in not only templating the formation of mineral via heterogeneous nucleation, but also in protecting the inside of the tooth against high stresses that occur during feeding.

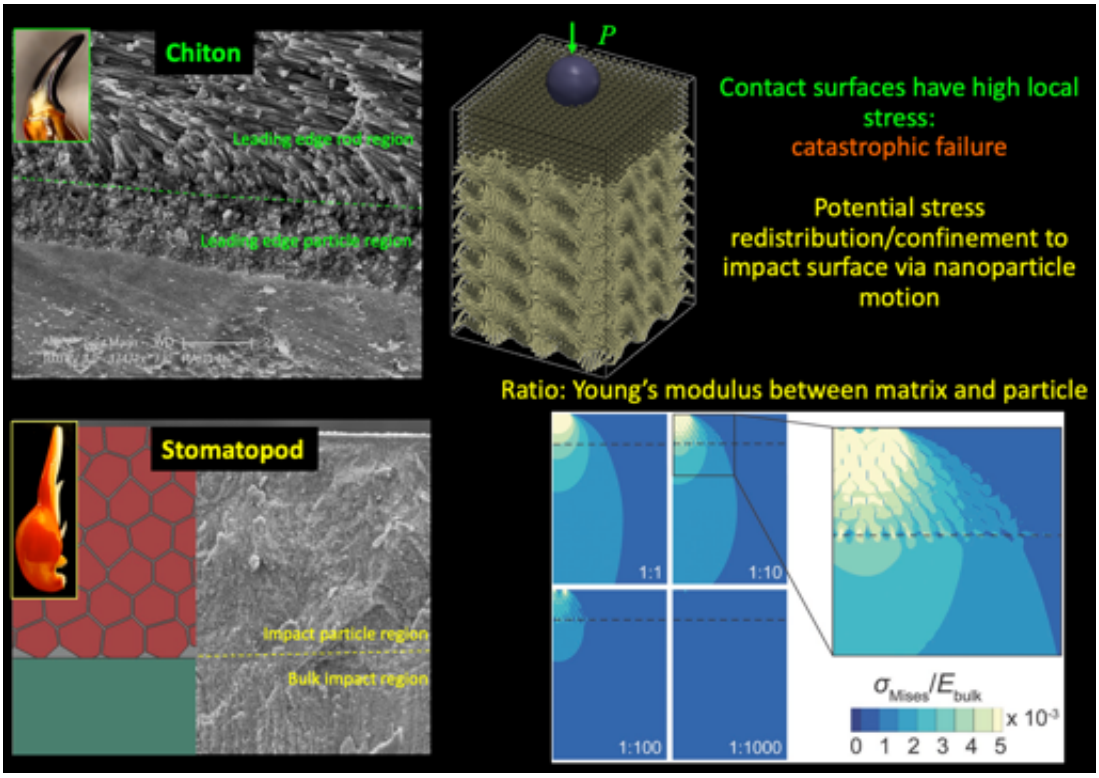

[Role of particle region in chiton tooth highlighted by modeling.]

However, higher resolution micrographs of the particle region in the tooth of C. stelleri shows that some of the particles may not be fully dense, while still showing a high level of crystallinity.

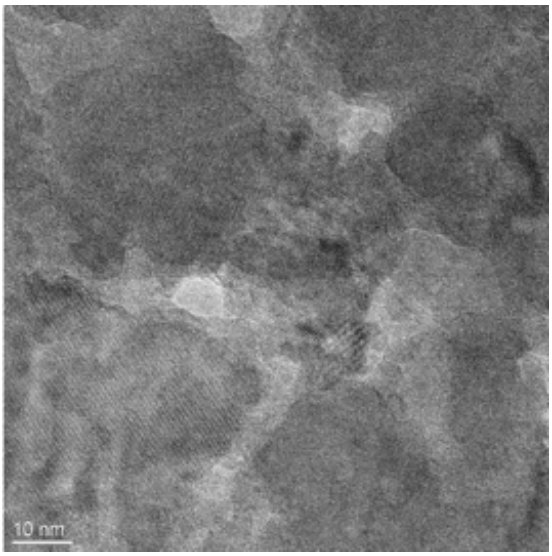

[HRTEM micrograph of particle region of C. stelleri, highlighting porous particles.]

Based on our hypothesis that proteins are co-located with chitin fibers and subsequently template the nucleation and growth of mineral, it is likely that these proteins are either occluded within the mineral phase or are phase separated from the mineral. This may yield a bi-continuous structure of protein-mineral.

Further structural analyses of the fully mineralized rod region of the teeth of C. stelleri also showed similar gaps between rods. A transverse section of the rod region from a FIB-sectioned tooth reveals not only that the rods are not smooth (i.e., contain nanoasperities), but also some of the rough surfaces of the rods are fused together in a common crystallographic orientation between two rods. The presence of these nanoasperities and fused "mineral bridges" is likely to provide not only strength, but toughness to this biological composite. Interestingly, this feature is seen in the inner layer of the California red abalone shell (i.e., the nacreous layer of $CaCO_3$), again, suggesting a convergent design feature.

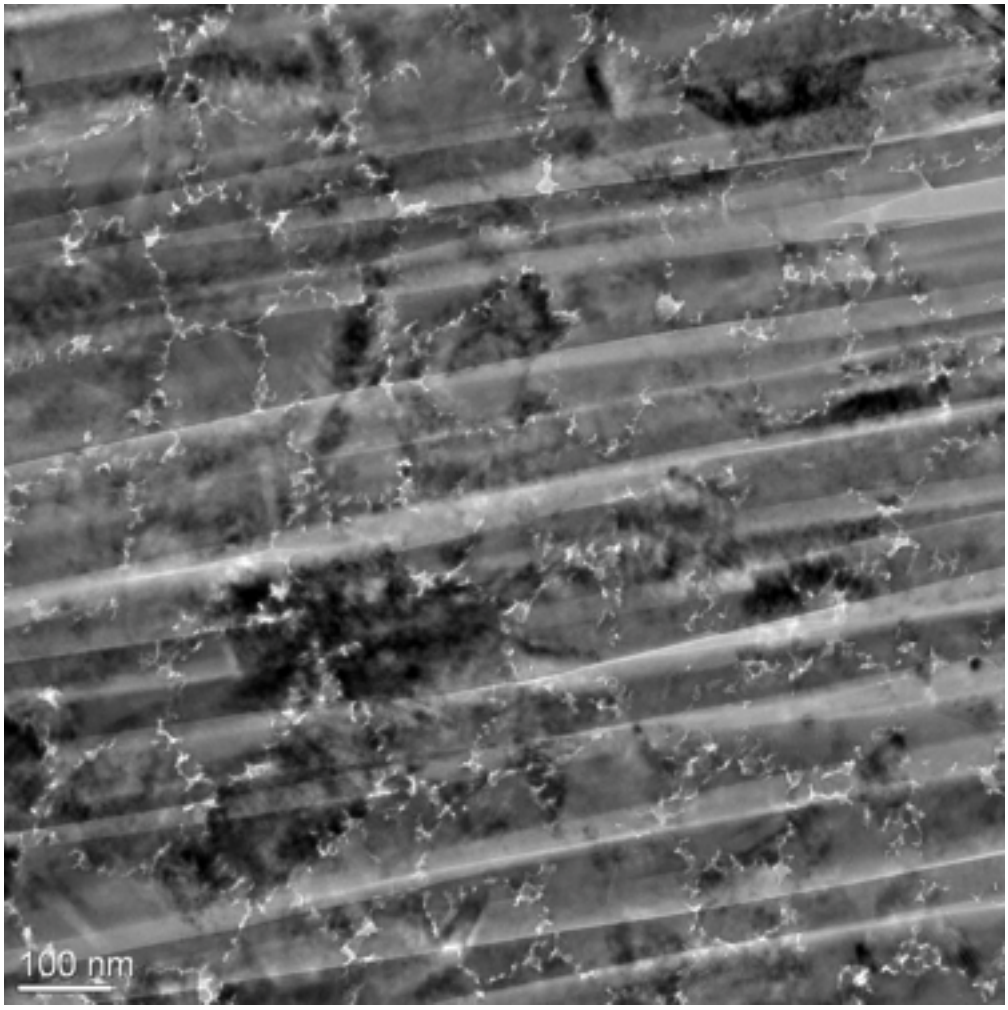

[TEM micrograph of transverse section of rod region of C. stelleri, highlighting rough surfaces/nanoasperities on rods.]

This provides strong evidence of a solution phase process that persists after the initial nucleation and phase transformation of the iron oxide mineral, which enables additional mineral to add to

existing rods and fuse neighboring rods together. Remnant pores underscore that organic phase is on the periphery of each nanorod, likely as a template that guides the orientation of the rods.

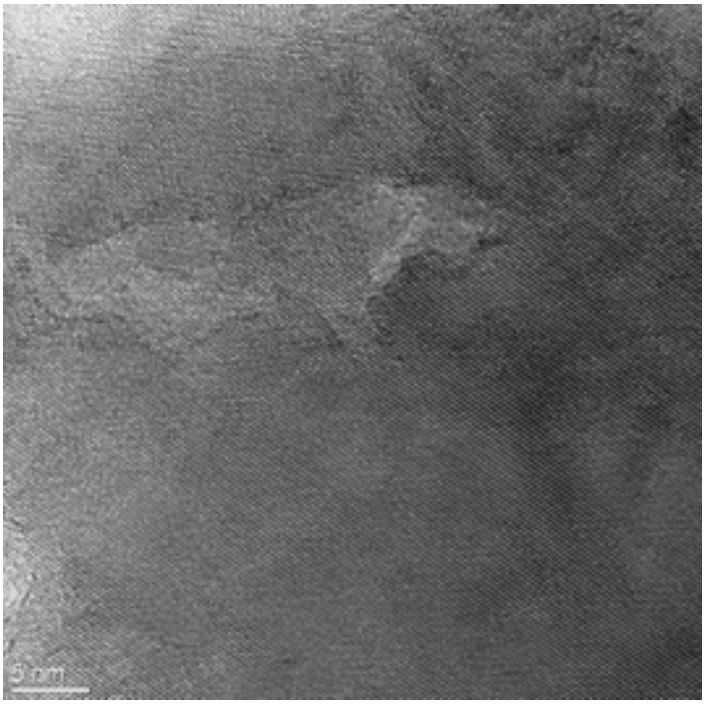

[HRTEM micrograph of transverse section of rod region of C. stelleri, where two nanoasperities join neighboring rods with same crystallographic alignment.]

Structural features of the mature monocuspid teeth of C. articulatus

Here, we have initiated the investigation of the structural features of C. articulatus, a chiton found off the western coast of the Mexican mainland.

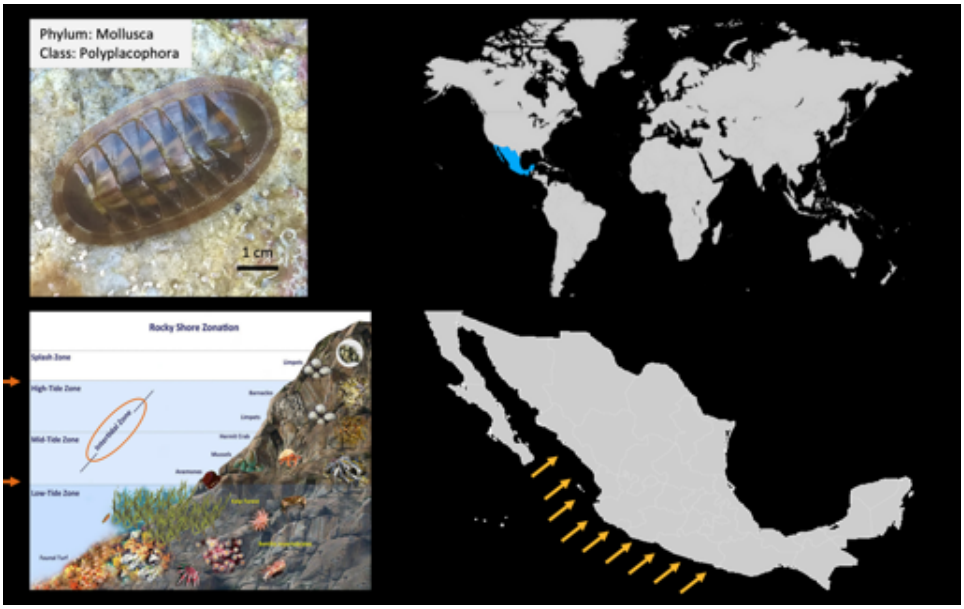

[*Chiton articulatus* and its location.]

This chiton feeds on more hard, encrusted algae and has a different morphology than C. stelleri.

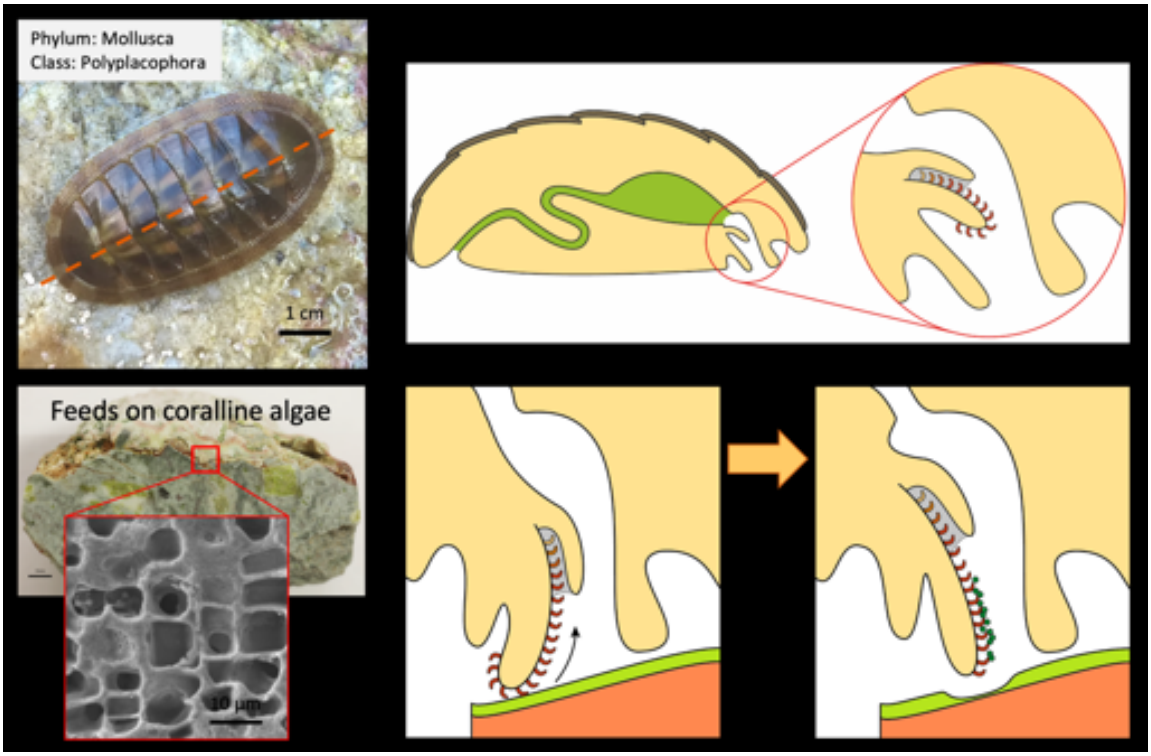

[*Chiton articulatus* and the coralline algae that it feeds on. The mechanism of feeding is similar to other chitons, but the morphology of the teeth and its radula differ from C. stelleri].

C. articulatus were collected in Sinaloa, Mexico by Kisailus and their radulae were extracted and transported to the USA to Kisailus' lab. Imaging of the radula highlights that it has more than 80 rows of teeth, with approximately more than 20 teeth utilized in rasping. The primary teeth used in rasping, the major lateral teeth, are supported by adjacent teeth. The major lateral cusps in *C. articulatus* are monocuspid.

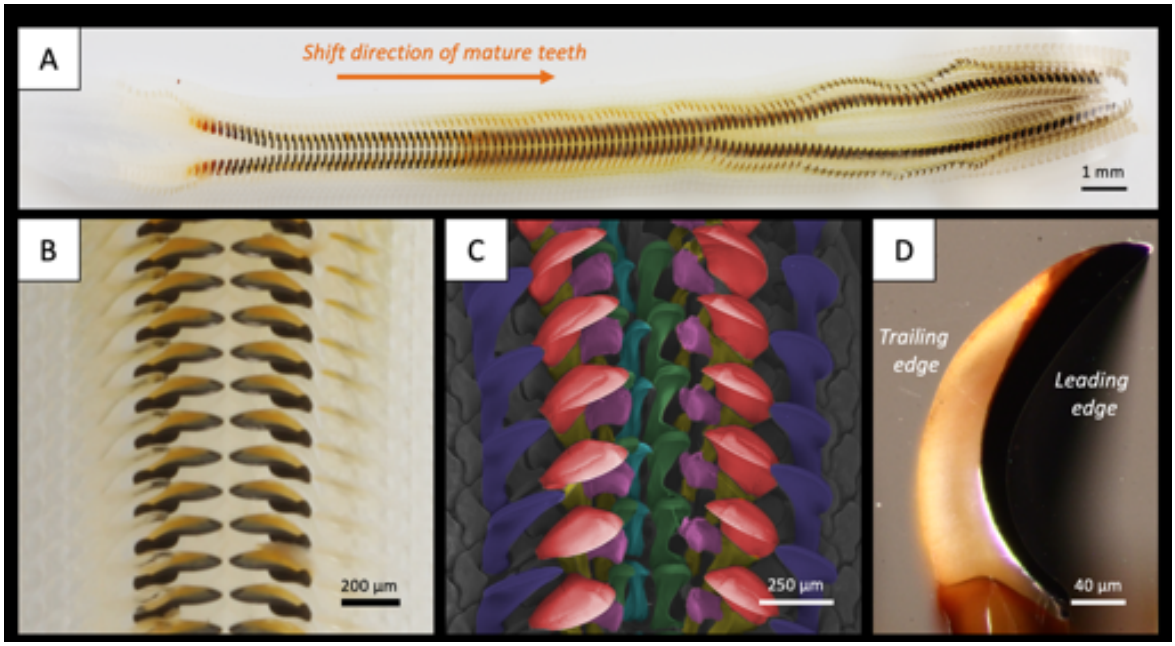

[A. Imaging of the radula highlights that it has more than 80 rows of teeth. B. Mature monocuspid teeth. C. False colored imaging highlighting teeth in red. D. Optical longitudinal section of one cusp, highlighting a multiregional mineralized structure.]

A longitudinal section of the fully mineralized cusp was prepared and examined using microbeam diffraction at Brookhaven National Lab. It was determined that indeed the tooth consists of multiple crystalline mineral and organic phases: magnetite (Fe_3O_4), lepidocrocite (FeOOH), goethite (FeOOH), hydroxyapatite ($Ca_{10}(PO_4)_6(OH)_2$) and chitin $(C_8H_{13}O_5N)_n$.

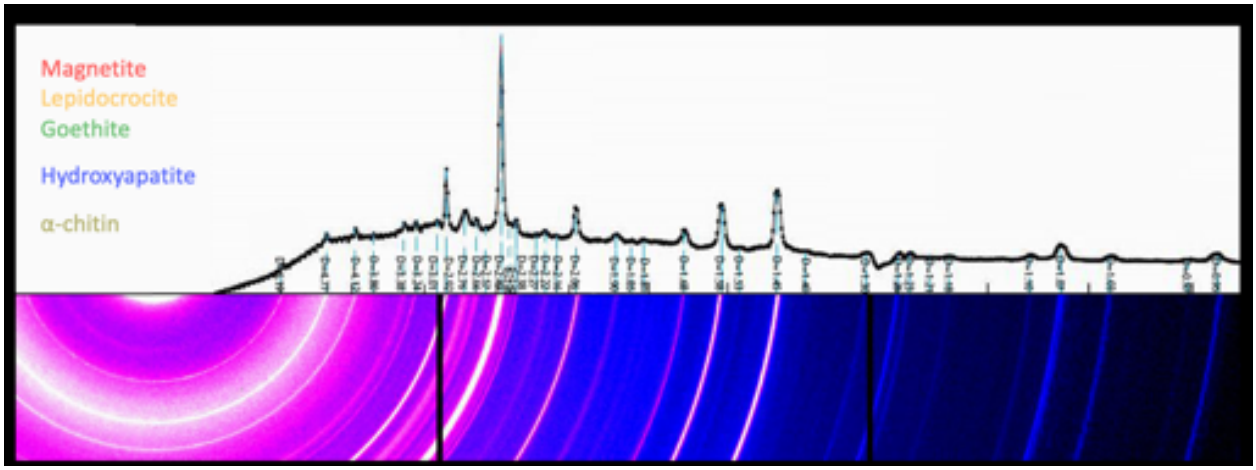

[Microbeam diffraction of fully mineralized tooth of *C. articulatus* revealing multiple mineral phases and alpha-chitin.

Further examination of the tooth was conducted by Raman spectroscopy. A line scan through the tip of the tooth revealed the location of these phases. A back scattered SEM shows a highly mineralized phase on the leading edge of the tooth, which was determined to be the magnetite phase. Behind the leading edge are two metastable and hydrated phases of iron oxide,

lepidocrocite and goethite. The trailing edge of the tooth consists of hydroxyapatite, as a backing layer.

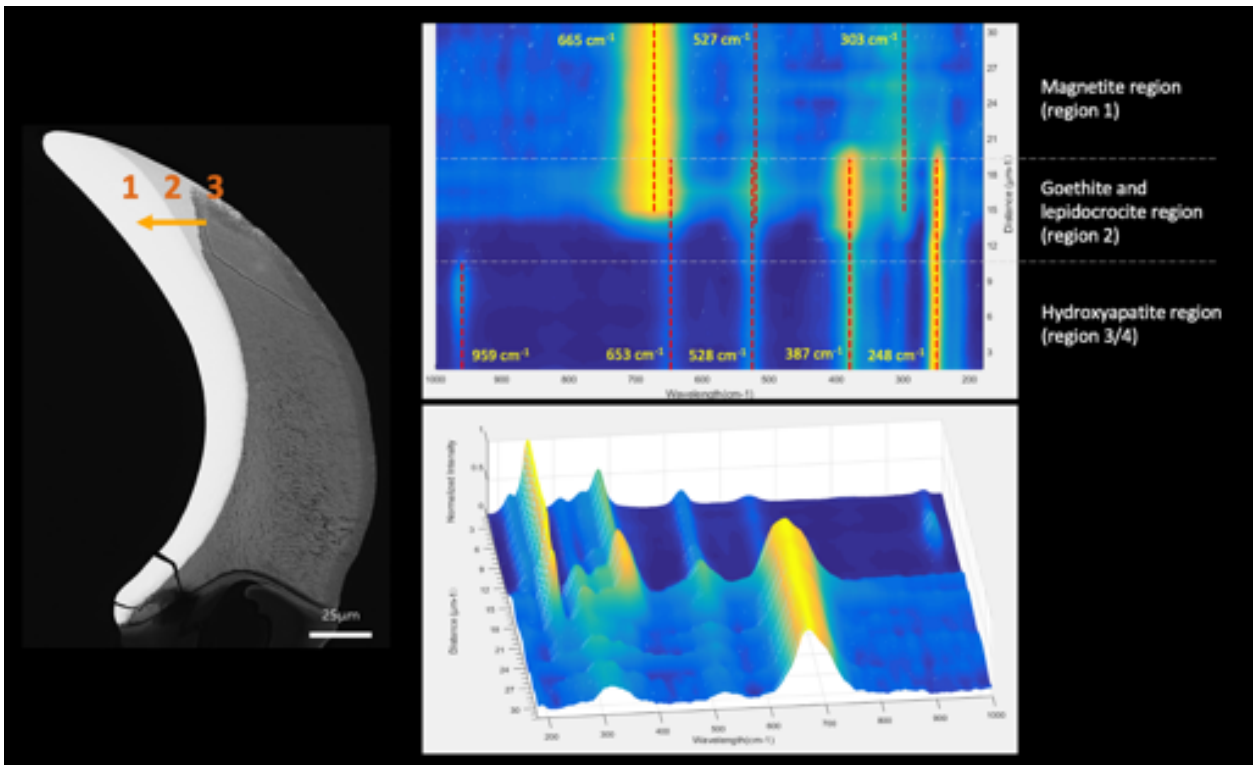

[Back scattered SEM of tooth of C. articulatus. Raman line scan as shown in BSE micrograph. Data reveals multiple phases and their locations.]

In the coming year, we plan to examine more details of the nano and microstructures within these teeth.

2. Probe the immature teeth from the chitons in order to derive microstructural and phase evolution pathways. Investigate the underlying organic framework (structural and chemical) that controls phase selection and regulates nucleation and growth of mineral in the teeth.

During the past year, we have started to examine the immature teeth from *C. stelleri*. Details of our work follows.

Tooth #4: Analyses of microtomed sections of tooth #4 near the leading edge revealed clusters of particles arranged in a linear fashion. We believe these are guided by the chitinous fibers that are pre-assembled before mineralization occurs. Of note, however, is that upon performing electron diffraction of what appear to be aggregated particles, we notice that it diffracts much like a highly aligned mesocrystal (not quite single crystalline). We will continue to investigate this in the coming year.

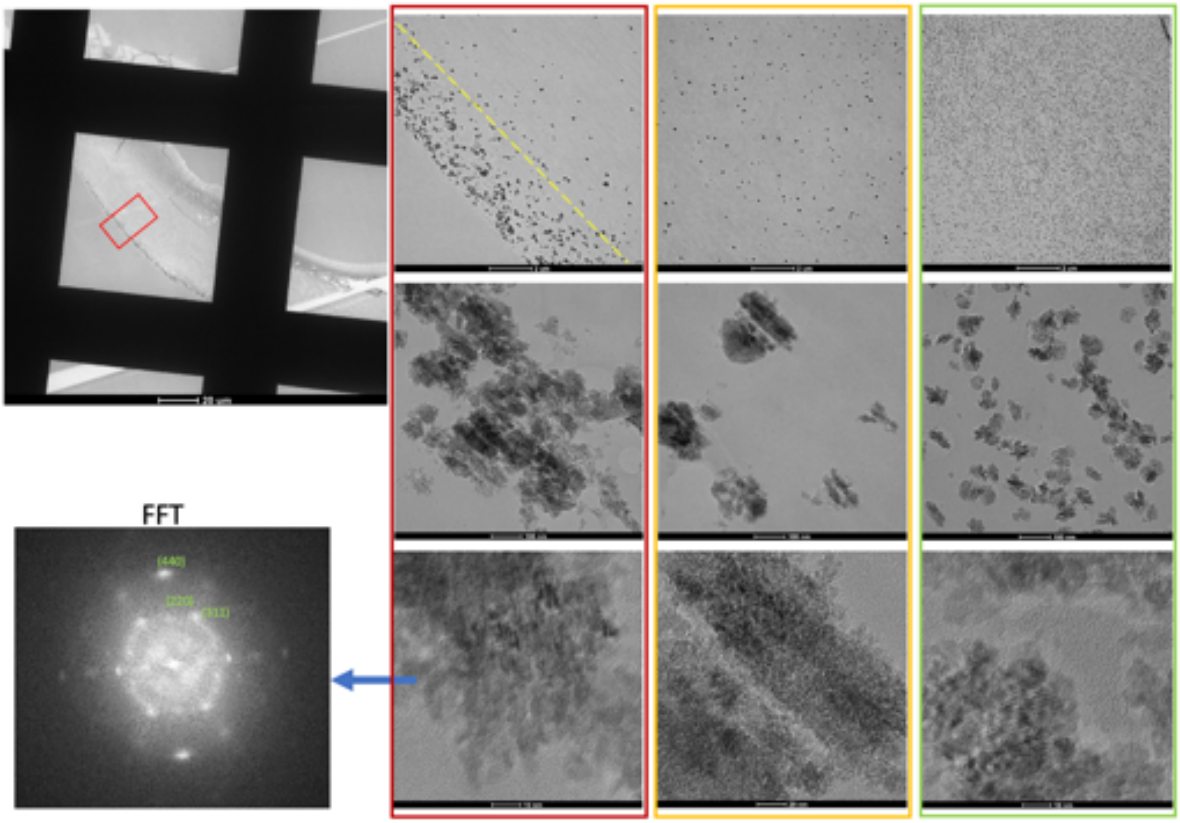

[TEM analysis of tooth #4 along midpoint of leading edge. Red column highlights aggregated and aligned clusters of particles. Fast Fourier Transform of one cluster of aggregates "diffracts" as a mesocrystal.]

As the nanoparticle aggregates were clearly ordered in tooth #4 and were magnetite in phase, we decided to look back at an earlier stage tooth, #2, to look at the ordering of these similar particles. We were not surprised to find that within tooth #2, the particles were not yet transformed to magnetite and were thus, still ferrihydrite. However, these particles of ferrihydrite, which are always found as random aggregates (***in any other natural system as well as in geologic form***), were highly ordered as well (i.e., mesocrystals!).

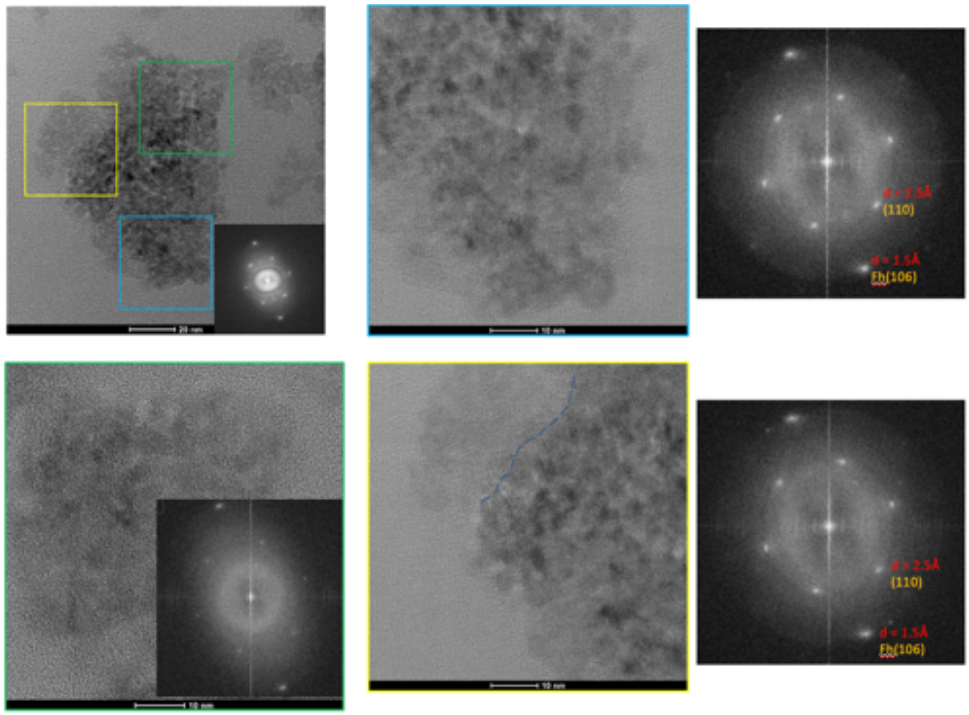

[TEM analysis of tooth #2 along midpoint of leading edge. Bright field TEM shows large (60-80nm aggregate particles consisting of smaller (~ 5nm) primary domains. Fast Fourier Transform clusters of aggregates "diffracts" as a mesocrystal of ferrihydrite.]

Interestingly, when we performed HRTEM, we found that the crystalline domains of ferrihydrite maintained continuous ordering even though different domains were separated by what appear to be amorphous regions.

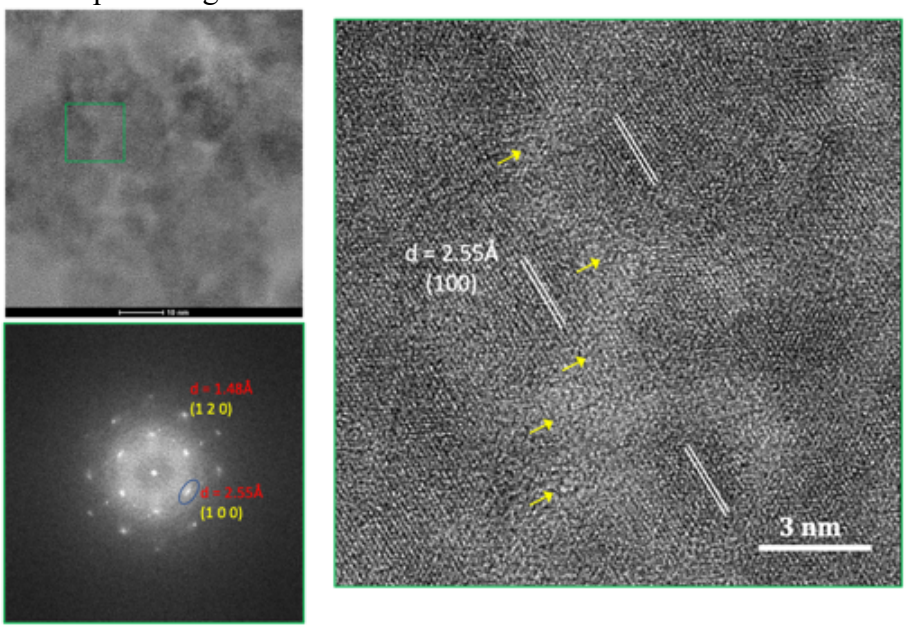

[HRTEM analysis of tooth #2 within one secondary (60-80nm aggregate) particle. Arcs in diffraction suggest mesocrystalline order. Yellow arrows on right show amorphous regions separating aligned crystal domains.]

Based on our observations of Mesocrystalline ferrihydrite in tooth #2, we examined a similar region in tooth #4 (i.e., midpoint of tooth along leading edge in rod region). Here, we found that 1 single secondary particle (~ 100 nm diameter) contained both ferrihydrite and magnetite phases, yet diffracted like a mesocrystal. Thus, this provided the impetus to suggesting a phase transformation pathway that has not been previously observed. We will continue this work in the coming year.

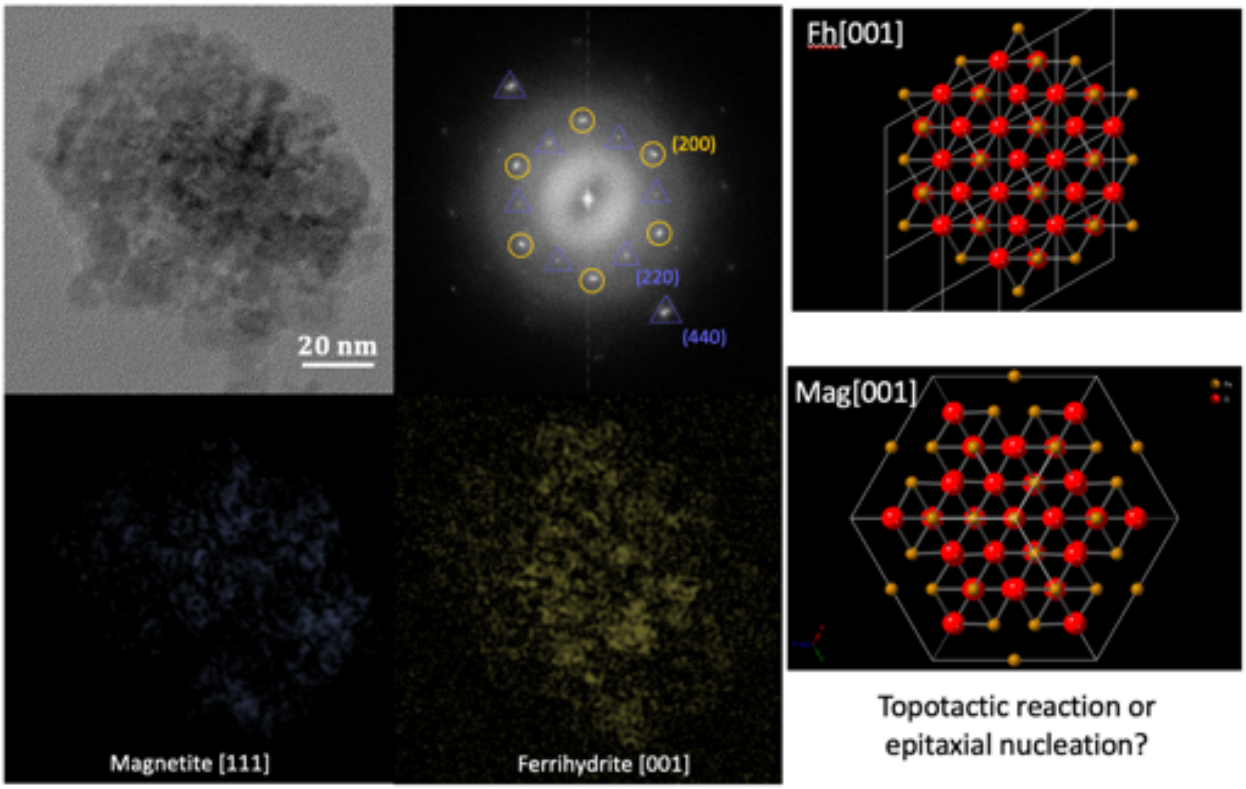

[TEM analysis of tooth #4 within one secondary (100 nm aggregate) particle. Both magnetite and ferrihydrite diffraction spots are observed and suggest both phases co-exist. Inverse FFT show where the suggested phases are located within the particle. On the right, we surmise there may be a solid state phase transformation with little or no change in Gibbs Free energy. We continue to investigate this.]

Tooth #5: SEM analyses of nanoparticles in the rod region here show that the chitinous fibers that are believed to control and guide the growth of mineral are possibly occluded within the rods, but certainly are at the periphery of each nanorod. Smaller domains of crystal grow around these nanorods as "nanoasperities" which control the roughness of neighboring rods and also lead to fused rods via mineral bridges.

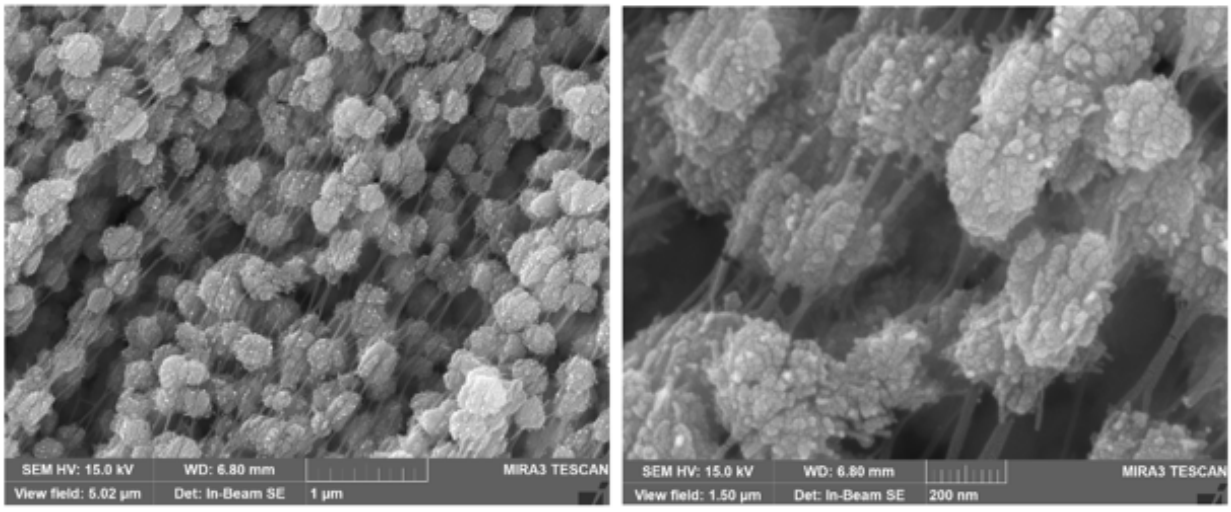

[SEM imaging showing aligned aggregates on chitinous fibers. High magnification imaging (right) shows the chitin fibers "embedded" within particles.]

Based on this, we used a STEM based, high angle annular dark field imaging technique to investigate the particles more closely. What we found is that larger chitinous fibers bifurcate many of the secondary particles while we do observe larger primary particles on their periphery. Also of note, are smaller gaps between some domains and even pore-like structures.

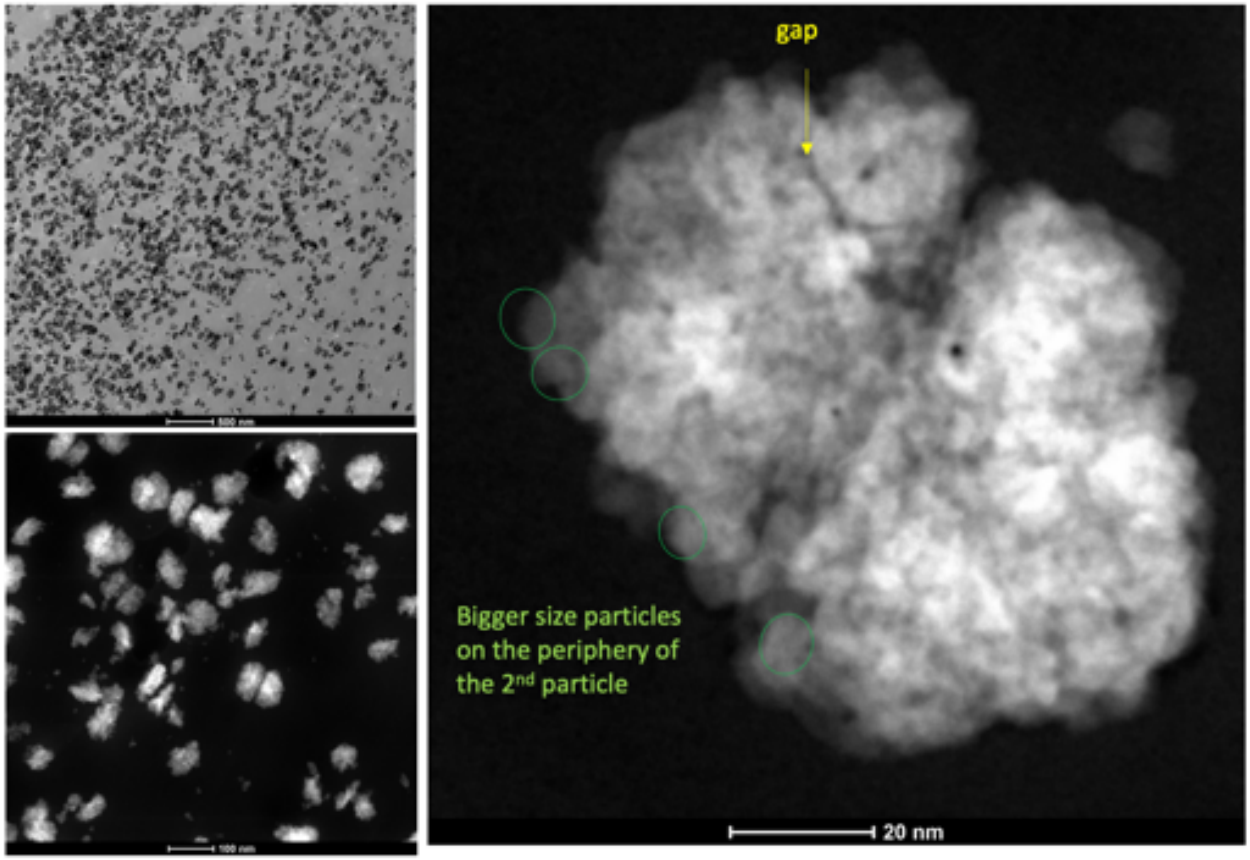

[STEM-HAADF imaging of particles in tooth #5.]

Since chitinous fibers are likely used as structural scaffolding and will be co-located with proteins that control nucleation and growth of the mineral, we performed EDS analyses on the same region. As expected, the particles showed the presence of Fe and O. However, within the particles, we observed nitrogen, phosphorus, magnesium and sulfur. Based on this, it is likely that the morphology of the particles, and perhaps even the ordering (i.e. mesocrystallinity) is guided by peptides that are phosphorylated. It also suggests that the occluded organic may increase the toughness and hardness of these biominerals. Again, more work is needed here.

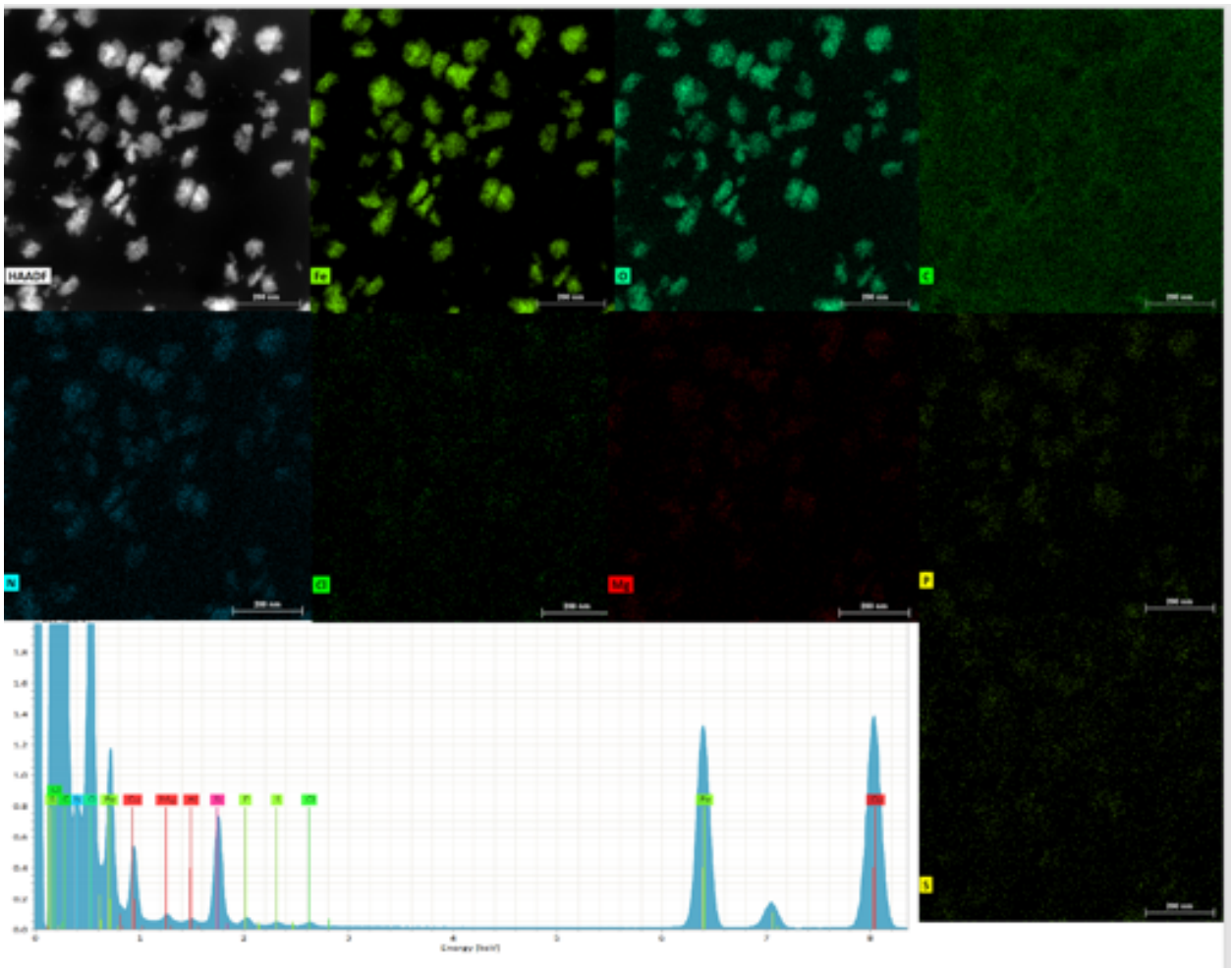

[EDS analysis of particles from tooth #5.]

However, the insights provided here have helped us to write a review paper in Advanced Materials. The review is far too long to add to this report, but here is the citation:

"Multiscale toughening mechanisms in biological materials and bioinspired designs," W. Huang, D. Restrepo, J.Y. Jung, F.Y. Su, Z. Liu, R.O. Ritchie, J. McKittrick, P. Zavattieri, **D. Kisailus**, *Advanced Materials*, **31 (43)** (2019) 1901561. DOI: 10.1002/adma.201901561

Tooth #6: Additional analysis of tooth #6, ~ 5 µm in from the leading edge, demonstrated that the aforementioned clusters of particles now show signs of crystal faceting, even though they appear

to be consisting of aggregated primary particles. This does suggest that primary particles attach along specific crystallographic planes that ultimately lead to the faceting of low energy planes.

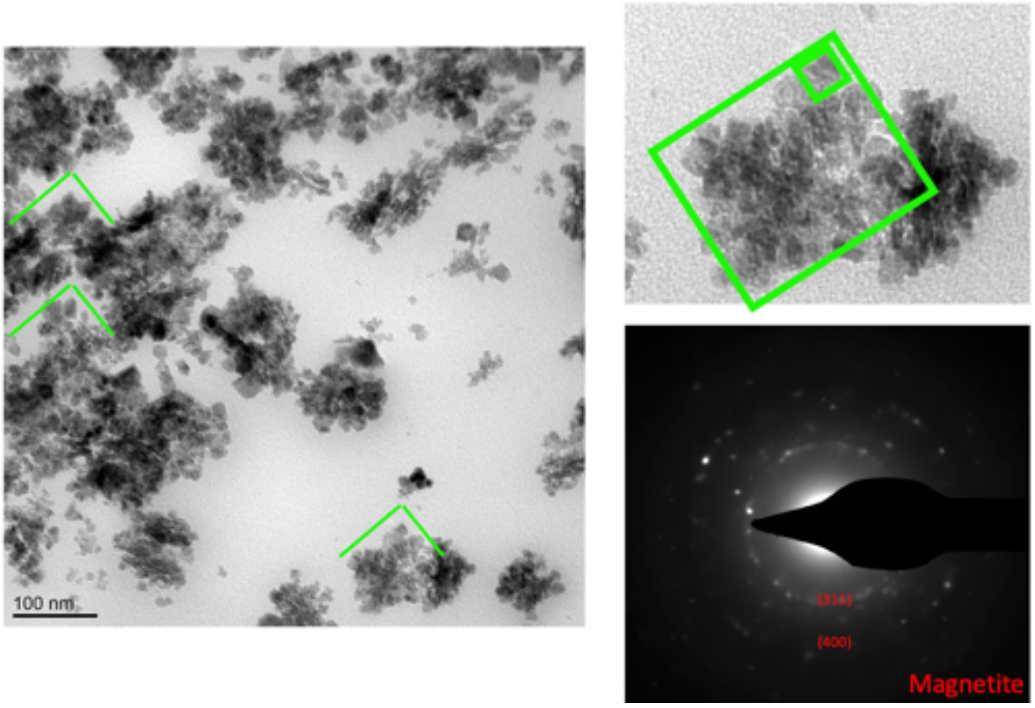

[TEM analysis of tooth #6, 5 µm in from the leading edge showing onset of faceting in magnetite aggregates.]

Deeper within the tooth (i.e., 10µm from the leading edge), larger domains now appear at the periphery of aggregates. These larger domains are likely single crystal magnetite. The source of the nutrient may be from the dissolution of smaller crystallites or more ferrous iron from either the epithelial tissue or from the stylus-tooth junction. More analyses are needed here.

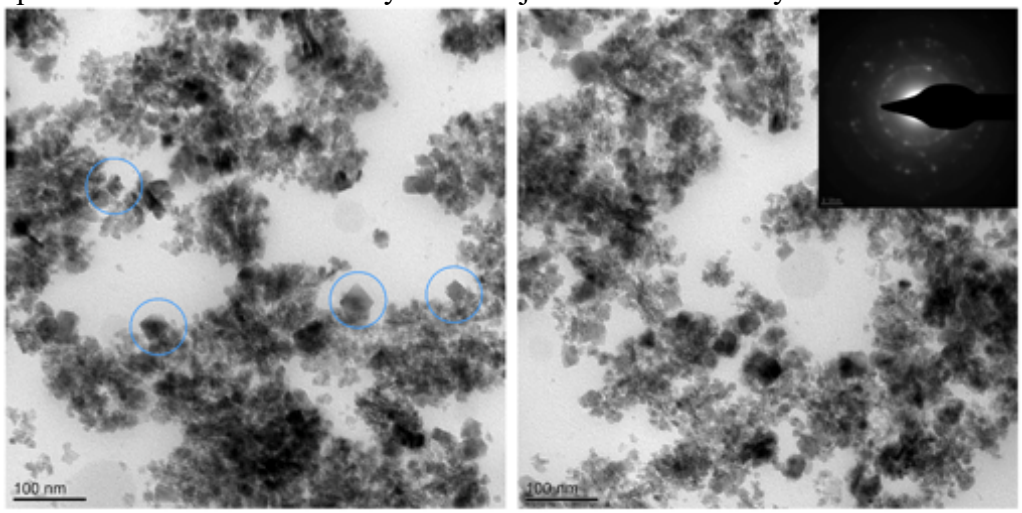

[TEM analysis of tooth #6, 10µm in from the leading edge showing large facets of magnetite blue circles.]

Utilizing a new method to investigate chiton:

Finally, over the past year, I have collaborated with a group from University of Melbourne to image magnetic domains within the chiton teeth. Here, we applied two complementary quantum magnetic microscopy methods, based on nitrogen-vacancy centers in diamond, to spatially map the mineral phases ferrihydrite and magnetite in the developing teeth of *Acanthopleura hirtosa*. The images reveal previously undiscovered long-range magnetic order, established at the onset of magnetite mineralization. This is in contrast to electron microscopy studies that show no strong common crystallographic orientation. The implications of these results are important, not just for the insights gained in biomineralization of the target organism, but also for the study of a broad range of iron minerals in the physical and biological sciences. The result of this work has lead to a paper in Small Methods and is attached here:

Quantum Magnetic Imaging of Iron Biomineralisation in Teeth of the Chiton *Acanthopleura hirtosa*

Julia M. McCoey, Mirai Matsuoka, Robert W. de Gille, Liam T. Hall, Jeremy A. Shaw, Jean-Philippe Tetienne, David Kisailus, Lloyd C. L. Hollenberg, and David A. Simpson**

J. M. McCoey, M. Matsuoka, R. W. de Gille, Dr. L. T. Hall, Dr. J.-P. Tetienne, Prof. L. C. L. Hollenberg, Dr. D. A. Simpson
School of Physics, The University of Melbourne, Parkville, 3010, VIC, Australia

Dr. J. A. Shaw
Centre for Microscopy, Characterisation and Analysis, University of Western Australia, Perth, 6009, WA, Australia

Prof. D. Kisailus
Department of Chemical and Environmental Engineering, Bourns Hall B357, Riverside, CA 92521, USA

E-mail: simd@unimelb.edu.au & jmccoey@unimelb.edu.au

Keywords: biomineralisation, diamond, magnetic imaging, chiton, nitrogen-vacancy

Iron is critical for life. Nature capitalises on the physical attributes of iron biominerals for functional, structural and sensory applications. Iron biomineralisation is well exemplified by the magnetite-bearing radula of chitons, the hardest known biomineral of any animal. Although magnetism is an integral property of iron biominerals, limited information exists on the magnetic state, structure and orientation of these nanoscale materials during mineralisation. The advent of

quantum based magnetic microscopy provides a new avenue to probe these biological systems directly, providing detailed magnetic information of the iron oxide structures. Here we apply two complementary quantum magnetic microscopy methods, based on nitrogen-vacancy centers in diamond, to spatially map the mineral phases ferrihydrite and magnetite in the developing teeth of *Acanthopleura hirtosa*. The images reveal previously undiscovered long-range magnetic order, established at the onset of magnetite mineralisation. This is in contrast to electron microscopy studies that show no strong common crystallographic orientation. The implications of these results are important, not just for the insights gained in biomineralisation of the target organism, but also for the study of a broad range of iron minerals in the physical and biological sciences.

1. Introduction

Chitons represent an ideal model system to study iron biomineralisation. Anatomically, they possess eight hard dorsal plates and a soft body, with a ventrally-facing mouth (**Figure** 1a). Chitons require structurally hard teeth because of their feeding habits. They are omnivorous grazers, rasping food from rocky substrates with their radula, a tongue-like organ with rows of curved teeth. The fully developed teeth possess material properties equivalent to the hardest structural ceramics.[1] These abrasion- and load-resistant properties are due to the biogenic magnetite capping the tooth cusp.[2] In chitons, a single radula contains rows of teeth, with each tooth row progressing in discrete stages from an unmineralised to a fully mineralised state.[3]

The major iron minerals that compose the structure of mature teeth in the Australian chiton *Acanthopleura hirtosa*[4] are magnetite, goethite, and calcium apatite (Figure 1b). While the mechanical properties and mineral composition of mature chiton teeth have been studied extensively in multiple species[1, 5, 6], little is known about the growth and transformation of the iron biomineral phases and their organisation at the early stages of mineralisation.

To investigate the magnetic organisation of the iron biominerals at the early stages of development, a quantum-based magnetic imaging approach[7, 8] is employed that combines high-resolution spatial imaging with quantitative mapping of static and fluctuating magnetic fields to study in-situ mineral phases. Our diamond-based magnetic microscope provides subcellular magnetic profiling while distinguishing the magnetic signals from magnetite and ferrihydrite.

2. Results

2.1. Magnetite imaging via static magnetic field

To image the spatial distribution of iron-containing minerals, we designed and constructed a quantum-based magnetic microscope, which exploits the magnetic sensitivity of atomic defects in diamond.[9] Our system consists of an inverted optical wide-field microscope with a diamond sensing chip containing a 2D array of negatively charged nitrogen-vacancy (NV) centers engineered approximately 6-8 nm beneath the diamond surface (Figure 1c), see methods. The NV centre in diamond is an atomic point defect consisting of a substitutional nitrogen atom and an adjacent vacancy aligned along one of four possible <111> crystallographic orientations. The NV centre can exist in the neural or negatively charged state. A simplified schematic of the electronic structure of the negatively charged NV center, referred to as NV from herein is shown in Figure 1d. The NV centre possesses two unpaired electrons resulting in a spin 1 system with a diamond crystal field splitting of 2.87 GHz separating the $|0\rangle \rightarrow |\pm1\rangle$ ground spin states. The $|\pm1\rangle$ ground spin states Zeeman split in the presence of a the local magnetic field by, $\Delta E = 2\gamma B_{NV}$, where γ is the NV gyromagnetic ratio = 2.8 MHz G^{-1}. The NV centres are conveniently spin polarised at room

temperature into the $m_s = 0$ ground spin state using green (532 nm) laser light.[9] The spin-dependent NV fluorescence (637-800 nm) can be imaged onto a sCMOS camera, allowing optically detected magnetic resonance (ODMR) of the ground state energy levels to be performed at each imaging pixel of the sensing array.[10, 11] A separate imaging protocol based on the measurement of the spin relaxation time (T_1) of the NV spins is used for sensing fluctuating magnetic fields.[12, 13] In this protocol, the NV spins are polarised using pulsed green excitation and then left to evolve in the dark for a variable time, τ, before optical spin readout. Both quantum sensing protocols are used to image the magnetic properties of chiton teeth before, during and post the onset of mineralisation: ODMR is used to image the static vector magnetic fields from magnetite (Figure 1e) via the Zeeman splitting of the ground state energy levels. While quantum relaxation microscopy is used to image the magnetic fluctuations from superparamagnetic ferrihydrite (Figure 1f) by monitoring changes in the NV spin lattice relaxation time. Imaging may be performed consecutively without any adjustment of the sample or microscope setup.

Acanthopleura hirtosa radulae were set in resin and sectioned for imaging as shown in **Figure 2**a. Correctly orienting the section through the tooth is crucial to achieve an accurate interpretation of the tooth structure. Critically, this is the first study to use X-ray tomography during the sample preparation workflow, facilitating the targeted collection of tooth sections from known orientations. This provides absolute certainty when interpreting ODMR data with respect to the tooth's microstructure across various length scales and places the observed information in precise context with the tooth's functional properties. Because the radula provides a series of progressive

snapshots of tooth development, we sectioned multiple teeth from the same radula. Teeth are numbered from less mineralised to more mineralised, with the first tooth that displays orange colouration being tooth zero. Sections were cut to show the tooth preceding mineralisation (tooth -1), at the onset of mineralisation (tooth 0), and more advanced stages of mineralisation where phase transformations to magnetite have occurred (teeth 3 and 4) (Figure 2b and c).

The microtomed tooth sections were mounted on the diamonds for imaging, see methods. At room temperature, magnetite particles are ferrimagnetic and therefore present a stable static magnetic field that can be imaged via ODMR (Figure 2d). The magnetic field strength from the magnetite nanoparticles can be measured via the Zeeman splitting of the NV energy levels obtained from the ODMR spectrum at each pixel, resulting in a 2D magnetic field map. A weak uniform background field of 30 G was applied to the sample to obtain the magnetic field map in Figure 2d. The background field was sufficient to separate the four NV orientations, but an order of magnitude below the magnetic coercivity of the magnetite nanoparticles, H_c ~ 800-900 G for particles > 30 nm.[14] The background magnetic field contribution is removed by subtracting the average magnetic field from a 20 μm^2 region off the tooth, see methods for more information. All teeth were imaged in this mode, see supplementary information. No static magnetic signals were detected from tooth -1, indicating no ferrimagnetic magnetite nanoparticles, consistent with this stage of tooth development in *A. hirtosa.*[15] Magnetic signals corresponding to the posterior surface of tooth 0 were resolved, see supplementary information, and the strength of the static magnetic signal increases for both tooth 3 and 4 as shown in Figure 2e and f, recall that these magnetic images represent the magnitude of the magnetic field along a given NV axis.

2.2. Vector magnetic imaging of magnetite

To determine the magnitude and direction of the magnetite's magnetisation, we measure the full magnetic field vector at each imaging pixel. To implement this capability, we apply a weak and uniform background field of 30 G sequentially along each NV axis using a three-axis Helmholtz coil. This permits measurement of the magnetic field projection along each of the four NV crystallographic axes. We used the magnetic field projections along three NV axes to reconstruct the x, y and z projections (**Figure 3**a and b) of the vector field.

The vector magnetic field maps show long-range magnetic order extending over the entire tooth section, with a broadly uniform magnetite magnetisation, oriented perpendicular to the plane of the section (Figure 3c). This long-range magnetic order is surprising, because at this stage of mineralisation, the magnetite particles are small and disconnected, without any orientational organisation evident in their individual visible structure alone, see supplementary information. Therefore, the long-range magnetic ordering indicates either that crystals were actively aligned by the underlying organic matrix, or that the particles were magnetically coupled as they transitioned into a ferrimagnetic state. Disturbances in the magnetic field due to fractures in the tooth from sectioning are also clearly resolvable (Figure 3d and e). A simplified magnetic model of tooth architecture supports the out of plane magnetisation finding, see supplementary information. Full vector maps of tooth 4 are also provided in the supplementary information with both teeth exhibiting similar magnetic profiles.

Previous work has identified anisotropy of magnetisation in the mature tricuspid teeth of *Acanthochiton rubrolinestus*,[16, 17] where the length and width of the teeth are more easily magnetised than the thickness.[18] Our vector magnetic microscopy images provide the first

evidence of magnetic organisation at the subcellular level in the chiton radula. We demonstrate that for *A. hirtosa,* in the early stages of tooth development, the magnetite nanoparticles are magnetised perpendicular to the plane of the section, i.e. across the tooth width.

Biomineralisation has, in multiple instances, been shown to occur via non-classical routes, including mesocrystalline intermediate stages and crystallization by particle attachment.[19] The possibility of a mesocrystalline formation mechanism was first raised for chiton biomineralisation upon the discovery of grain substructure in mature *A. hirtosa* teeth.[20] Our results support the presence of a magnetic mesocrystalline phase in the tooth cusp, preceding the ordered rods of magnetite in a mature tooth,[21] as overall order is seen in the magnetic vector maps on a scale larger than any individual faceted crystal. It has been proposed that the collective magnetic field produced by the cumulative fields of aligned nanocrystals in a mesocrystalline colloid could assist the formation of a magnetic solid.[22] It is conceivable, therefore, that the magnetic field produced by the alignment of the early magnetite nanoparticles may assist in the synthesis of the magnetite rods.

2.3. Magnetic microscopy of ferrihydrite

Prior to magnetite crystallisation, iron is present but not in a ferrimagnetic form. The first iron mineral to be deposited within the tooth is 6-line ferrihydrite, the predominant form of iron within ferritin.[23, 24] Ferrihydrite is a ferric oxyhydroxide and superparamagnetic at room temperature.[25] Ferrihydrite particles are less than 10 nm in size,[26] with a superparamagnetic fluctuation spectrum of order 1 GHz, see supplementary information Fig. S4 – S6. This magnetic fluctuation frequency conveniently overlaps with the NV transition energies from the $|0\rangle$ to $|\pm1\rangle$ states at zero magnetic

field. By monitoring the spin relaxation rate ($1/T_1$) of the NV centers across the full field of view,[27] see methods, we can detect and map the fluctuating magnetic fields from ferrihydrite directly, in a technique we term quantum relaxation microscopy (QRM).

Using QRM, we find the ferrihydrite concentration increases with development (**Figure 4**a), in agreement with studies across chiton species.[28] In teeth -1 and 0, where little or no magnetite is present, ferrihydrite is detected along the posterior face of the tooth cusp. In the more mature teeth (3 and 4), the bulk of ferrihydrite is on the anterior side of the magnetite, with a thin layer of ferrihydrite coating the outer, posterior side of the magnetite (Figure 4b and c).

As a mineral phase mapping technique, QRM is highly effective. Elemental mapping across whole *A. hirtosa* teeth has not previously been performed with any other technique; however, elemental and mineral phase locations have been investigated in other species. Energy dispersive spectroscopy and Raman spectroscopy have been used in combination with secondary electron microscopy to locate ferrihydrite and magnetite regions in the immature unicuspid teeth of *Acanthopleura echinate.*[29] Though not an imaging technique, the *A. echinata* results indicate multiple fronts of mineralisation, showing parallels with the present study. The QRM images show that by tooth 4, two distinct regions of ferrihydrite border the bulk of the magnetite region. In addition to the ferrihydrite band that appears on the posterior tooth cusp by tooth 4, the interior band extends further in towards the core of the tooth cusp. This contrasts with the ferrihydrite pattern in the tricuspid teeth of *Cryptochiton stelleri* observed via micro X-ray fluorescence (μXRF).[21] These similarities and differences may be related to the mineralisation strategy employed; *A. echinata* and *A. hirtosa* form an apatite core while *C. stelleri* has a hydrated iron phosphate core. Because of the variation in these mineralisation strategies, it would be worthwhile

in future studies to examine multiple species with the high resolution, whole tooth mapping that QRM provides. The iron biominerals within chiton teeth studied here present two distinct magnetic signatures; however, more advanced stages of mineralisation will contain new biomineral phases such as goethite and lepidocrocite. Diamond-based electron spin resonance spectroscopy techniques[30, 31] may allow these specific mineral phases to be mapped and imaged in more mature teeth.

3. Conclusion

The application of quantum-based magnetic microscopy to biological systems presents several key advantages when compared to existing magnetic imaging techniques. Widefield magnetic microscopy allows for rapid acquisition and high throughput when compared to scanning probe techniques such as MFM and transmission electron microscopy (TEM). Nitrogen-vacancy centers provide full vector magnetic imaging capability, which is extremely difficult to achieve in MFM or superconducting quantum interference device (SQUID) systems. Furthermore, studies of long-range magnetic order now become possible as the field of view is increased significantly in comparison to existing methods such as TEM. In our current configuration the magnetic imaging resolution is limited by the diffraction limit of light to ~300 nm^2. The lateral resolution is dictated by the magnetic signal fall-off, for static magnetic signals the resolution is governed by the size of the particles contributing to the signal, for magnetite nanoparticles in chiton teeth this equates to the thickness of the microtomed slice 500 -1000 nm. For the superparamagnetic imaging, the magnetic signal fall-off is steeper and ultimately limited by the T_1 time of the NV ensembles. For the diamond sensor used in this work, the lateral resolution is approx. 100 nm. It should be noted that the superior spatial resolution and magnetic sensitivity of quantum-based magnetic microscopy is offset by the fact that it is a 2D imaging technique, unlike PET, MRI and CT. There

is opportunity to extend the imaging technique to 3D via multiple sectioning at the expense of time. Quantum-based magnetic microscopy does however compliment the vast array of techniques used to study biological samples such as TEM[32], X-ray magnetic circular dichroism[33], XRF[21], positron emission tomography/CT[34] and photoacoustic imaging[35]. Inevitably, it will be the combination of these imaging techniques which is needed to elucidate the complex relationship between the magnetic properties, the crystalline structure of iron biominerals and the underlying organic matrix.

The precise mechanisms governing the attachment of ferrihydrite to the organic matrix and the subsequent phase transformation remain active areas of research. The magnetic images presented in this work reveal previously undiscovered long-range magnetic order at the onset of magnetite mineralisation, in contrast to electron microscopy studies that show no strong common crystallographic orientation. A complete picture of mineralisation must now consider the development of magnetic order and its possible effects on the nanoscale assembly of magnetite. We anticipate that the magnetic profiling techniques demonstrated in the present study will become valuable tools for probing such interactions in concert with the current suite of high-resolution electron and X-ray microscopy techniques. Given the interest in biomimetic materials, future work may exploit quantum magnetic microscopy for real time imaging of magnetite assembly using synthetic approaches adapted from biological systems. The unique combination of vector magnetic imaging and QRM on a bio-compatible platform opens a pathway toward mineral-specific imaging of a vast range of biological systems.

5. Experimental Section

Materials: The diamond imaging sensor used in this work is engineered from electronic grade Type IIa <111> diamond (Element 6). The diamonds were thinned, cut and re-polished to a 1 × 2 × 0.1 mm^3 crystal (DDK, USA). NV defects were engineered via ion implantation of ^{15}N atoms at an energy of 4 keV and dose of 1×10^{13} ions cm^{-2}. Molecular dynamic simulations indicate a NV depth range between 5-10 nm.[36] The implanted sample was annealed at 1000 °C for three hours and acid treated to remove any unwanted surface contamination. The density of NV centers post annealing was 1×10^{11} NV cm^{-2}.

Sample preparation: Fresh specimens of the chiton *A. hirtosa*[4] were collected and dissected as described previously.[37] Care was taken to avoid exposing the samples to any strong magnetic field from collection to measurement. Briefly, radulae were excised and fixed in 2.5% glutaraldehyde, buffered in 0.1 M phosphate at pH 7.2 (osmotic pressure adjusted to 900 $mmol \cdot kg^{-1}$ using sucrose). Radulae were then fixed, dehydrated, and infiltrated in epoxy resin using microwave-assisted chemical fixation (Pelco, Biowave).

To facilitate the collection of histological sections from precise orientations through the teeth, resin blocks were first scanned using X-ray micro-computed tomography (μCT). Scans were conducted at 80kV and 82 μA using a Versa 520 XRM (Zeiss, Pleasanton, USA) running Scout and Scan software (v11.1.5707.17179, Zeiss). A total of 401 projections were collected over 360°, each with a 1 second exposure. 2x binning was used to achieve a suitable signal to noise ratio and 0.4x optical magnification was used to achieve an isotropic voxel resolution of 12.8 μm. Raw data were

reconstructed using XMReconstructor software (v11.1.5707.17179, Zeiss) following a standard center shift and beam hardening correction. The standard 0.7 kernel size recon filter setting was also used. Reconstructed data were observed (TXM3D Viewer, Zeiss) to determine the position of the major lateral teeth relative to the resin block and a razor blade was used to then mark the resin at the correct plane of orientation to produce a longitudinal cut through the middle of each tooth.

Resin blocks were then trimmed at this orientation using a glass knife on an ultramicrotome (EM UC6, Leica Microsystems). Once the correct position was reached, 1 µm sections were cut with a diamond knife (Histo, Diatome) onto filtered DI water. Sections were transferred using a wooden applicator stick to a drop of ~70 °C filtered DI water (situated in a Petri dish placed on a hotplate). Sections were left to warm for 1-2 mins on the water drop to assist with smoothing the section. Sections were transferred using a wooden applicator stick to a drop of filtered DI water on the imaging slide. An eyelash mounted on a wooden applicator stick was used to position the section onto the diamond chip and a paper wick was then used to remove excess water from the slide; finally, the sample was air dried.

Optical Imaging: Samples were diamond-imaged in wide-field on a modified Nikon inverted microscope (Ti-U). Optical excitation from a 532 nm Verdi laser was focused (f = 300 mm) onto an acousto-optic modulator (Crystal Technologies Model 3520–220) and then expanded and collimated (Thorlabs beam expander GBE05-A) to a beam diameter of 10 mm. The collimated beam was focused using a wide-field lens (f = 300 mm) to the back aperture of the Nikon x60 (1.4 NA) oil immersion objective via a Semrock dichroic mirror (Di02-R561-25 × 36). The beam was first centred to the objective, then translated until the beam totally internally reflected within the

diamond. The NV fluorescence was filtered using two bandpass filters before being imaged using a tube lens (f = 300 mm) onto a sCMOS camera (Neo, Andor). Microwave excitation to drive the NV spin probes was applied via an omega gold resonator (diameter = 0.8 mm) lithographically patterned onto a glass coverslip directly under the diamond imaging chip. The microwave signal from an Agilent microwave generator (N5182A) was switched using a Minicircuits RF switch (ZASWA-2-50DR+). The microwaves were amplified (Amplifier Research 20S1G4) before being sent to the microwave resonator. A Spincore Pulseblaster (ESR-PRO 500 MHz) was used to control the timing sequences of the excitation laser, microwaves and sCMOS camera and the images where obtained and analysed using custom LabVIEW code. The excitation power density used for imaging was 30 W mm^{-2} and all images were taken in an ambient environment at room temperature.

Quantum relaxation microscopy: To implement quantum relaxation microscopy the spin lattice relaxation time (T_1) of the NV centers was determined by optically polarising the NV spins into the $m_s = 0$ ground state, then allowing the spins to evolve (in the dark) for a time τ, before sampling their spin polarisation with an additional optical pulse. Interactions between the NV centers and neighbouring electronic, nuclear and surface spins species cause the NV net magnetization to relax from the $m_s = 0$ state to a mixture of the three ground triplet states. The e^{-1} time of the decay is the T_1 time of the NV centers. In this work we normalised the T_1 decay with an identical pulse sequence with a single π pulse applied prior to the spin readout. This provides common mode rejection of noise sources from the NV imaging array. The quantum relaxation microscopy image analysis was performed using custom LabVIEW code.

Electromagnet: Magnetic fields were applied with a custom 3D Helmholtz coil to control both the strength and the direction of the magnetic fields. Copper enamelled wires (ECW0.71) were wound 200-time rounds on each cylindrical side of the Helmholtz coil. To reduce temperature increasing caused by the Joule heating of the copper wires, the coil was manufactured from aluminium and a computer water cooling system (EK CoolStream PE 240 Dual Radiator, EK Vardar 120mm Fan F4-120 2200RPM, and EK-XRES 100 SPC-60 MX PWM Pump/Reservoir Combo) was installed, with water running through a path inside the coil. The power supplier (Hameg HMP2030) was used for generating a static magnetic field.

Image analysis: Custom LabVIEW code was written for image analysis. To produce static magnetic field images, NV fluorescence images were binned 4x4, and ODMR spectra across the two peaks corresponding to the aligned NV axis were obtained for each binned pixel of the image stack. The spectra were fitted with single Lorentzian and the magnetic field strength determined from the peak splitting. The background magnetic field was removed by calculating the average of the 20 × 20 μm area outside of the tooth. This value was subtracted across the full field of view. The resulting magnetic field signal at each binned pixel was saved as an image, and a colour scale applied with ImageJ (Fiji distribution, ImageJ 1.51h). To produce the quantum relaxation images, the NV fluorescence images were binned 4x4, and the T_1 decay curves were obtained for each binned pixel of the image stack. The T_1 decay rate ($1/T_1$) was determined at each binned pixel by fitting the data to a stretched exponential of the form $y = A\,exp^{\left(t/T_1\right)^p} + c$, where A is the amplitude of the exponential decay, T_1 is the spin lattice relaxation time, p is the stretched exponential power (p = 1 represents a single exponential decay) and c is the offset. Near surface NV centers are known to exhibit a distribution of T_1 times from the NV ensemble depending on

their proximity to the surface and local spin environment. This distribution leads to a non-exponential T_1 decay which is characterised well by a stretched exponential function. The T_1 rate at each pixel binned pixel was saved as an image, and a colour scale applied with ImageJ (Fiji distribution, ImageJ 1.51h).

Supporting Information

Supporting Information is available from the Wiley Online Library or from the author.

Acknowledgements
This work was supported by the Australian Research Council (ARC) through Grants No. FL130100119, DE170100129. J.-P.T. and L. T. Hall acknowledges support from the University of Melbourne through an Early Career Researcher Grants. The authors acknowledge the facilities, and the scientific and technical assistance of Microscopy Australia at the Centre for Microscopy, Characterisation & Analysis, The University of Western Australia, a facility funded by the University, State and Commonwealth Governments.

The authors declare no competing financial interest.

Received: ((will be filled in by the editorial staff))
Revised: ((will be filled in by the editorial staff))
Published online: ((will be filled in by the editorial staff))

References

1. Weaver, J. C.; Wang, Q.; Miserez, A.; Tantuccio, A.; Stromberg, R.; Bozhilov, K. N.; Maxwell, P.; Nay, R.; Heier, S. T.; DiMasi, E.; Kisailus, D., *Materials Today* **2010,** *13* (1), 42-52.
2. Lowenstam, H., *Science* **1967,** *156* (3780), 1373-1375.
3. Joester, D.; Brooker, L. R., *Iron Oxides: From Nature to Applications* **2016**.
4. Blainville, H. M., *Manuel de malacologie et de conchyliologie: contenant [etc.]*. **1825**; Vol. 1.
5. Saunders, M.; Kong, C.; Shaw, J. A.; Clode, P. L., *Microscopy and microanalysis : the official journal of Microscopy Society of America, Microbeam Analysis Society, Microscopical Society of Canada* **2011,** *17* (2), 220-5.
6. Wang, C.; Li, Q.; Wang, S.; Qu, S.; Wang, X., *Materials Science and Engineering: C* **2014,** *37*, 1-8.
7. Steinert, S.; Dolde, F.; Neumann, P.; Aird, A.; Naydenov, B.; Balasubramanian, G.; Jelezko, F.; Wrachtrup, J., *Rev. Sci. Instrum.* **2010,** *81* (4), 043705.
8. Le Sage, D.; Arai, K.; Glenn, D.; DeVience, S.; Pham, L.; Rahn-Lee, L.; Lukin, M.; Yacoby, A.; Komeili, A.; Walsworth, R., *Nature* **2013,** *496* (7446), 486-489.
9. Doherty, M. W.; Manson, N. B.; Delaney, P.; Jelezko, F.; Wrachtrup, J.; Hollenberg, L. C. L., *Physics Reports* **2013,** *528* (1), 1-45.

10. Simpson, D. A.; Tetienne, J.-P.; McCoey, J. M.; Ganesan, K.; Hall, L. T.; Petrou, S.; Scholten, R. E.; Hollenberg, L. C. L., *Sci Rep* **2016,** *6*, 22797.
11. Tetienne, J.-P.; Dontschuk, N.; Broadway, D. A.; Stacey, A.; Simpson, D. A.; Hollenberg, L. C. L., *Science Advances* **2017,** *3* (4), 1602429.
12. Cole, J. H.; Hollenberg, L. C. L., *Nanotechnology* **2009,** *20* (49), 495401.
13. Hall, L. T.; Cole, J. H.; Hill, C. D.; Hollenberg, L. C. L., *Phys. Rev. Lett.* **2009,** *103* (22), 220802.
14. Dar, M. I.; Shivashankar, S. A., *RSC Advances* **2014,** *4* (8), 4105-4113.
15. Kim, K.-S.; Macey, D.; Webb, J.; Mann, S., *Proceedings of the Royal Society of London. B. Biological Sciences* **1989,** *237* (1288), 335-346.
16. Jian-Gao, Z.; Xia, Q.; Wei, L.; Chuan-Lin, L.; Wen-Shan, Z., *Chinese Physics Letters* **2000,** *17* (7), 542.
17. Han, Y.; Liu, C.; Zhou, D.; Li, F.; Wang, Y.; Han, X., *Bioelectromagnetics* **2011,** *32* (3), 226-233.
18. Qian, X.; Zhao, J. g.; Liu, C. l.; Guo, C. h., *Bioelectromagnetics: Journal of the Bioelectromagnetics Society, The Society for Physical Regulation in Biology and Medicine, The European Bioelectromagnetics Association* **2002,** *23* (6), 480-484.
19. Bergström, L.; Sturm, E. V.; Salazar-Alvarez, G.; Cölfen, H., *Accounts of chemical research* **2015,** *48* (5), 1391-1402.
20. Saunders, M.; Kong, C.; Shaw, J. A.; Macey, D. J.; Clode, P. L., *Journal of structural biology* **2009,** *167* (1), 55-61.
21. Wang, Q.; Nemoto, M.; Li, D.; Weaver, J. C.; Weden, B.; Stegemeier, J.; Bozhilov, K. N.; Wood, L. R.; Milliron, G. W.; Kim, C. S.; DiMasi, E.; Kisailus, D., *Advanced Functional Materials* **2013,** *23* (23), 2908-2917.
22. Lu, Y.; Yin, Y.; Xia, Y., *Adv. Mater.* **2001,** *13* (6), 415-420.
23. Pan, Y.; Brown, A.; Brydson, R.; Warley, A.; Li, A.; Powell, J., *Micron* **2006,** *37* (5), 403-411.
24. Cowley, J.; Janney, D. E.; Gerkin, R.; Buseck, P. R., *Journal of structural biology* **2000,** *131* (3), 210-216.
25. Guyodo, Y.; Banerjee, S. K.; Penn, R. L.; Burleson, D.; Berquo, T. S.; Seda, T.; Solheid, P., *Physics of the Earth and Planetary Interiors* **2006,** *154* (3-4), 222-233.
26. Janney, D. E.; Cowley, J. M.; Buseck, P. R., *Clays and Clay Minerals* **2000,** *48* (1), 111-119.
27. Steinert, S.; Ziem, F.; Hall, L.; Zappe, A.; Schweikert, M.; Aird, A.; Balasubramanian, G.; Hollenberg, L.; Wrachtrup, J., *Nat. Commun.* **2013,** *4*, 1607.
28. Gordon, L. M.; Román, J. K.; Everly, R. M.; Cohen, M. J.; Wilker, J. J.; Joester, D., *Angewandte Chemie International Edition* **2014,** *53* (43), 11506-11509.
29. Brooker, L.; Lee, A.; Macey, D.; Van Bronswijk, W.; Webb, J., *Marine Biology* **2003,** *142* (3), 447-454.
30. Hall, L. T.; Kehayias, P.; Simpson, D. A.; Jarmola, A.; Stacey, A.; Budker, D.; Hollenberg, L. C. L., *Nature Communications* **2016,** *7*, 10211.
31. Simpson, D. A.; Ryan, R. G.; Hall, L. T.; Panchenko, E.; Drew, S. C.; Petrou, S.; Donnelly, P. S.; Mulvaney, P.; Hollenberg, L. C. L., *Nature Communications* **2017,** *8* (1), 458.
32. Zhou, Z.; Tian, R.; Wang, Z.; Yang, Z.; Liu, Y.; Liu, G.; Wang, R.; Gao, J.; Song, J.; Nie, L., *Nature communications* **2017,** *8*, 15468.

33. Iacocca, E.; Liu, T.-M.; Reid, A.; Fu, Z.; Ruta, S.; Granitzka, P.; Jal, E.; Bonetti, S.; Gray, A.; Graves, C., *Nature communications* **2019,** *10* (1), 1756.
34. Liu, Y.; Lv, X.; Liu, H.; Zhou, Z.; Huang, J.; Lei, S.; Cai, S.; Chen, Z.; Guo, Y.; Chen, Z., *Nanoscale* **2018,** *10* (8), 3631-3638.
35. Liu, Y.; Kang, N.; Lv, J.; Zhou, Z.; Zhao, Q.; Ma, L.; Chen, Z.; Ren, L.; Nie, L., *Adv. Mater.* **2016,** *28* (30), 6411-6419.
36. Lehtinen, O.; Naydenov, B.; Börner, P.; Melentjevic, K.; Müller, C.; McGuinness, L. P.; Pezzagna, S.; Meijer, J.; Kaiser, U.; Jelezko, F., *Phys. Rev. B* **2016,** *93* (3), 035202.
37. Shaw, J. A.; Macey, D. J.; Clode, P. L.; Brooker, L. R.; Webb, R. I.; Stockdale, E. J.; Binks, R. M., *American Malacological Bulletin* **2008,** *25* (1), 35-42.
38. Tetienne, J.-P.; Broadway, D.; Lillie, S.; Dontschuk, N.; Teraji, T.; Hall, L.; Stacey, A.; Simpson, D.; Hollenberg, L., *Sensors* **2018,** *18* (4), 1290.
39. Gossuin, Y.; Gillis, P.; Hocq, A.; Vuong, Q. L.; Roch, A., *Wiley Interdisciplinary Reviews: Nanomedicine and Nanobiotechnology* **2009,** *1* (3), 299-310.

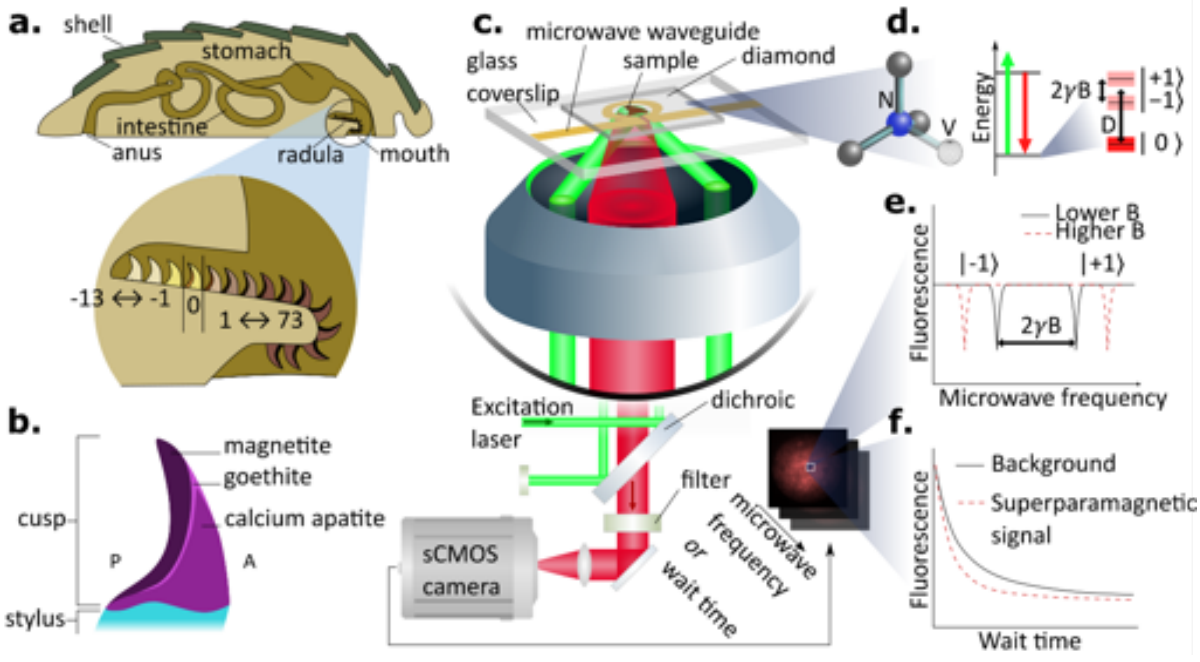

Figure 1. Quantum magnetic microscopy for studying iron-based biomineralisation. a, Chiton sagittal section. Enlargement shows the radula – an organ hosting rows of teeth which develop in a conveyor belt-like fashion. The entire tooth development (87 tooth rows in *A. hirtosa*) is seen in

one radula. b, The fully mature tooth cusp mineral structure of *A. hirtosa*, median longitudinal cut. c, Optical set-up of quantum magnetic microscope. The diamond sensing chip is excited via total internal reflection and the resulting fluorescence image is captured on an sCMOS camera. d, Schematic of the crystalline structure of the nitrogen vacancy (NV) center in diamond, and relevant energy levels. e, Optically detected magnetic resonance schematic for imaging ferrimagnetic (magnetite) minerals. f, Quantum relaxation microscopy schematic for imaging superparamagnetic (ferrihydrite) minerals.

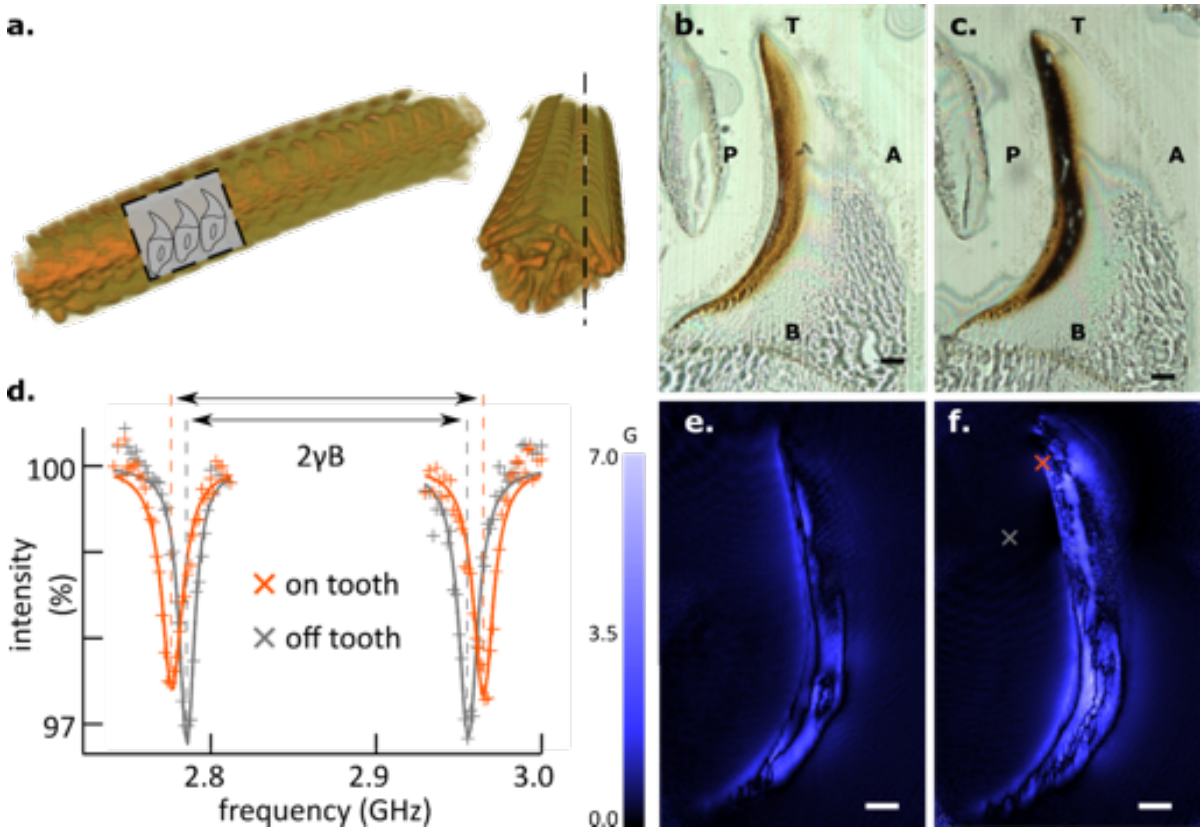

Figure 2. Sample sectioning and magnetic imaging. a, Radula set in resin, and microCT to facilitate longitudinal sectioning, dotted line. One micron thick slices of b, tooth 3, c, tooth 4, were mounted on the diamond sensing chip, scale bar 20 μm. d, Optically detected magnetic resonance (ODMR) spectra were measured at each imaging pixel across the entire tooth section. The separation of the ODMR transitions is proportional to local magnetic field $\Delta f = 2\gamma B$, where the gyromagnetic ratio of the NV center $\gamma 0 = 2.8$ MHz G-1. e and f, show the magnitude of the measured magnetic field projection along a single NV axis at 109.5° from the normal for tooth 3 and 4, respectively. Crosses in f correspond to ODMR spectra in d.

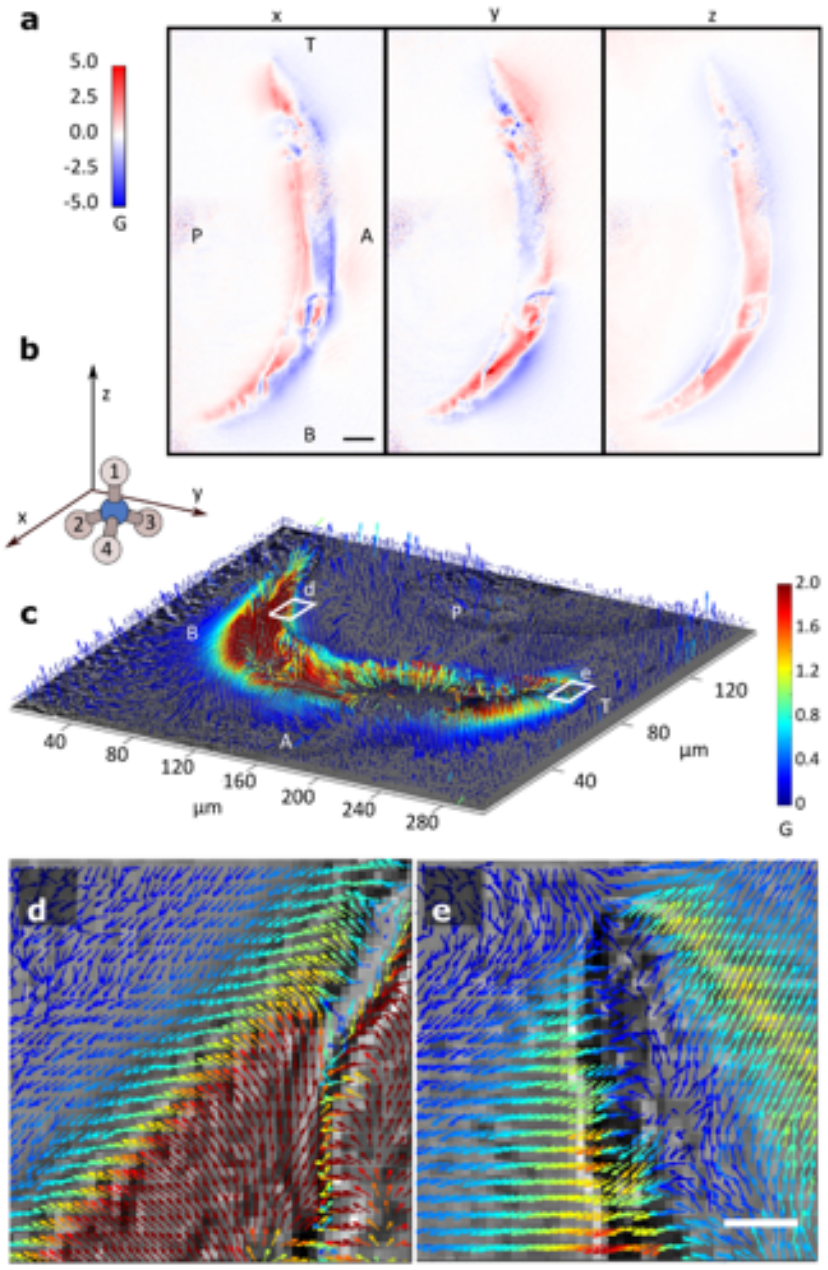

Figure 3. Vector magnetic field imaging of chiton teeth. a, maps of the x, y and z, (out-of-plane) components of the magnetic field, reconstructed from the four NV axes' maps. Letters indicate A anterior, P posterior, T tip, B base. b, Relative orientations of the diamond crystal axes and cartesian axes, as in c. c, Magnetic vector reconstruction of whole tooth cusp section of tooth 3. Colour scale represents magnitude of the magnetic field and the arrow direction represents magnetic field vector. To aid in visibility of signal from noise, a filter was applied reducing arrow length of noisy vectors. The vector reconstruction is performed by measuring the magnetic field projection along three known crystallographic directions of NV centers in diamond. The vector reconstruction is performed at each imaging pixel with a spatial resolution dictated by the

diffraction limit of the microscope, 300 nm. d, e, High resolution vector magnetic field maps of the x and y field components reveal long-range ordering along the tooth cusp, from base to tip, scale bar 2µm.

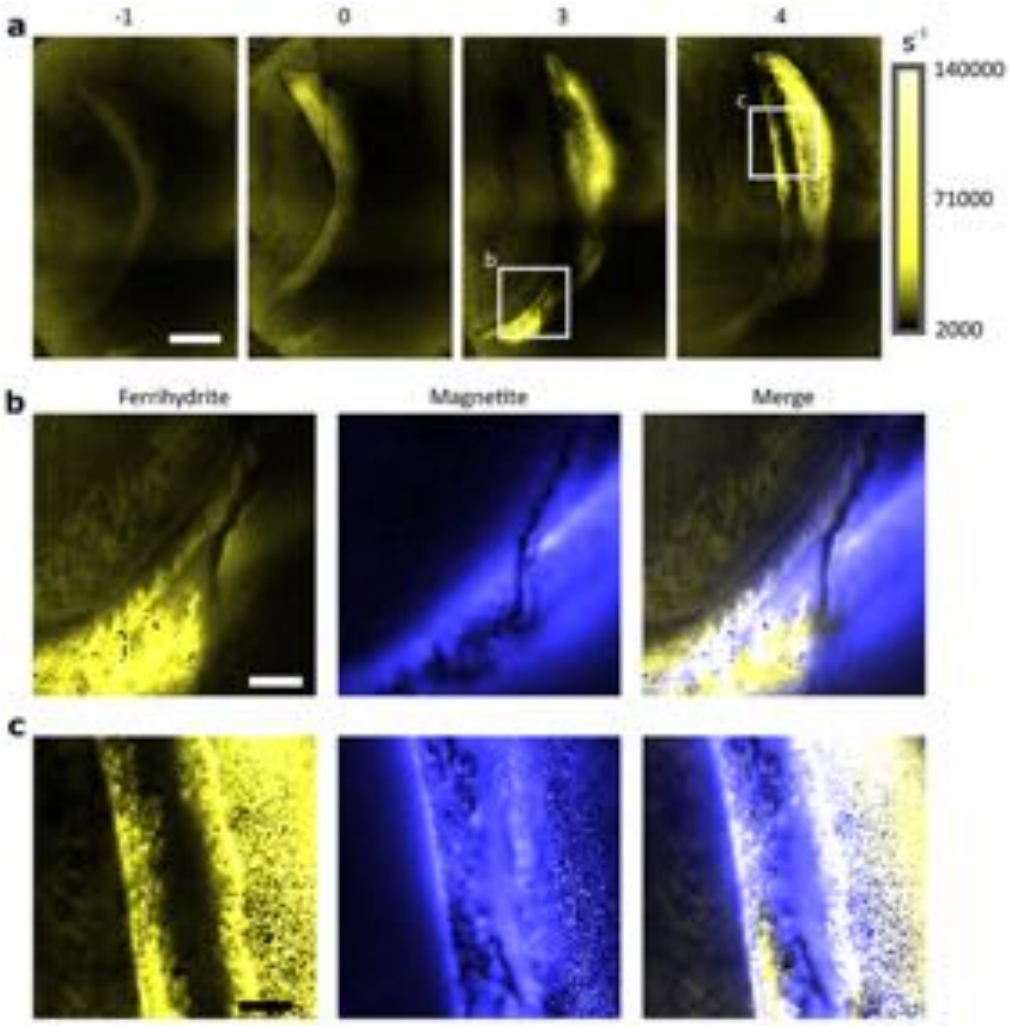

Figure 4. Superparamagnetic microscopy of chiton teeth. a, Quantum relaxometry images (1/T1) of the NV center in diamond showing the regions of superparamagnetic ferrihydrite. As the tooth develops, the total concentration and spatial distribution of ferrihydrite increases. Scale bar: 40 µm. b and c, show high resolution magnetic maps of ferrihydrite (1/T1) - yellow and magnetite (ODMR) - blue in various sections of the tooth. Areas of co-localisation (white) reveal regions undergoing magnetic phase transformation. Scale bar: 10 µm

A quantum-based magnetic imaging technique for characterising iron biominerals is reported. Chitons - marine molluscs - are an ideal model of the poorly understood process of iron biomineralisation. By applying diamond magnetic microscopy, the key components of chiton teeth, namely magnetite, and its precursor, ferrihydrite, are mapped with submicron resolution. Significantly, long-range magnetic order at early stages of tooth development is revealed.

Keyword: biomineralisation, diamond, magnetic imaging, chiton, nitrogen-vacancy

Julia M. McCoey*, Mirai Matsuoka, Robert W. de Gille, Liam T. Hall, Jeremy A. Shaw, Jean-Philippe Tetienne, David Kisailus, Lloyd C. L. Hollenberg, and David A. Simpson*

Quantum Magnetic Imaging of Iron Biomineralisation in Teeth of the Chiton *Acanthopleura hirtosa*

ToC figure

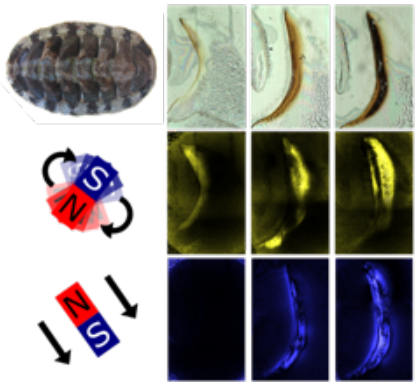

Supporting Information

Quantum Magnetic Imaging of Iron Biomineralisation in Teeth of the Chiton *Acanthopleura hirtosa*

Julia M. McCoey, Mirai Matsuoka, Robert W. de Gille, Liam T. Hall, Jeremy A. Shaw, Jean-Philippe Tetienne, David Kisailus, Lloyd C.L. Hollenberg, David A. Simpson**

Optically detected magnetic resonance at and before magnetite mineralisation

Optically detected magnetic resonance (ODMR) studies were performed across four teeth from rows -1, 0, 3 and 4, with 0 being defined as the onset of mineralisation. (**Figure** S1 a-d). Magnetic field maps of teeth -1 and 0 show very weak magnetic signals (Figure S1 e,f) when compared to the magnetic maps of teeth 3 and 4 (Figure S1 g,h). Figure S1 i,j show the magnetic field profile on a scale a factor of 10 less than tooth 3 and 4. A signal is detected along the posterior edge of the tooth cusp in row 0, consistent with the orange colouration and the emergence of magnetite, however an ODMR magnetic signal could not be detected for teeth in row -1, as expected.

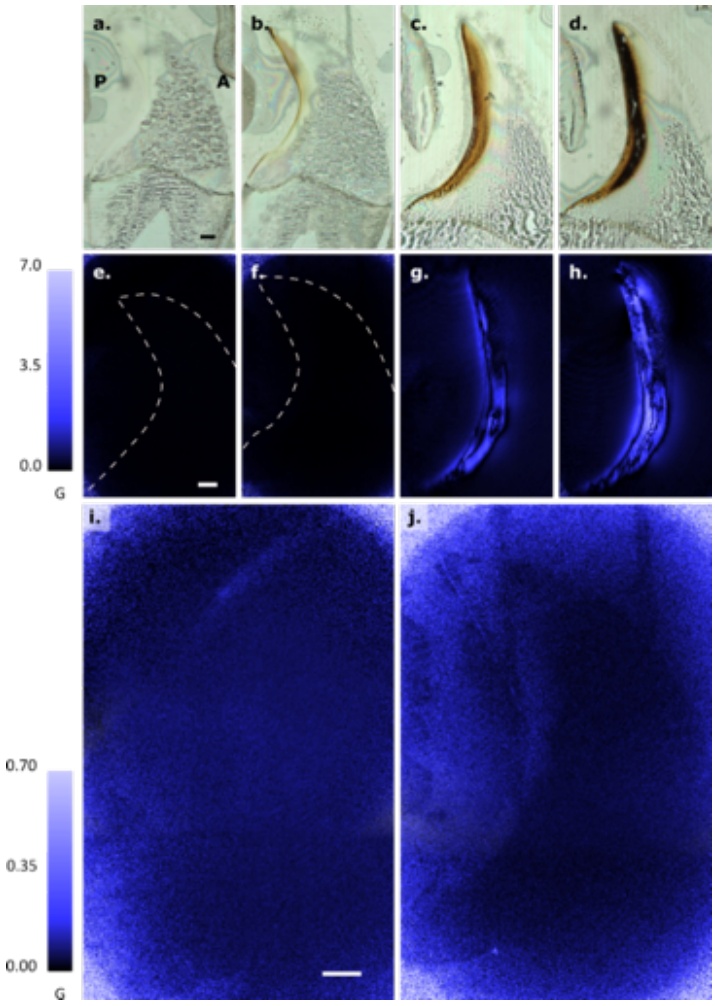

Figure S1| Progression of magnetite mineralisation. A: anterior, P: posterior. Light micrographs of radula sections from *A. hirtosa*, **a**, tooth -1 **b**, tooth 0, **c**, tooth 3 **d**, tooth 4, scale bar 20 micron. Magnitude of magnetic field, **e**, tooth -1, **f**, tooth 0, **g**, tooth 3, **h**, tooth 4, scale bar 20 micron. On oversaturated scale, magnitude of magnetic field strength of **i**, tooth -1, **j**, tooth 0, scale bar 20 micron.

Vector reconstruction and magnetisation Figure simulation

The magnetic field vector reconstruction shown in Figure 3 of the manuscript for tooth 3 is consistent with that obtained for the proceeding tooth 4 as shown in S2. The images from both teeth appear consistent with the magnetite magnetisation being out of plane. To reach a quantitative understanding of the apparent magnetic field distribution measured Figure S2, we constructed a simple magnetic model to simulate the magnetic fields from the layer of magnetite nanoparticles. We include in the model the NV response to magnetic fields, the optical readout and the spectral fitting as detailed in[38]. The magnetic model consisted of magnetic cubes laid within a polygon approximating the shape of the magnetite region of the tooth. The magnitude of the magnetisation was arbitrary, and the direction of magnetisation set out of plane, i.e. perpendicular to the tooth section. The simulation was carried out with 3788 magnetic cubes, each 0.5×0.5×0.5 μm, distributed within a polygon (area 5377.5 μm^2), in the x-y plane, and with a height in the z direction of 1 μm (two layers of cubes) to simulate the microtome slice thickness. Each cube has a magnetisation of 3×10^4 A m^{-1}. The results of the simulation are shown in Figure S2 along with the measured magnetic maps from tooth 3 and 4. The intact edges and central sections of the teeth are in agreement with the simulation and indicate that the teeth are magnetised along their width.

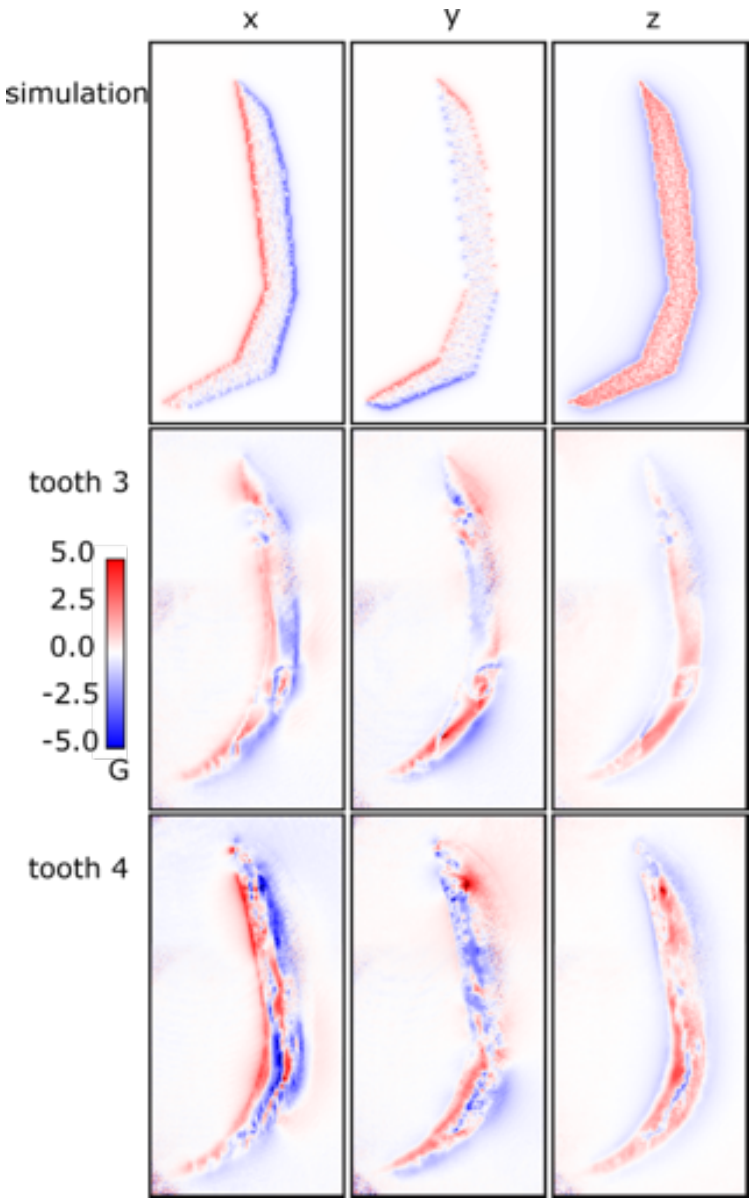

Figure S2| Simulation and maps of magnetic field vector components. Columns show the x, y, and z projections of the magnetic field sensed at the NV layer, respectively. The top row shows the results of simulation with the middle and bottom rows showing the measured data for tooth 3 and 4 respectively.

Transmission electron microscopy

The vector magnetic images shown in Figure 3 d and e of the manuscript reveal detailed magnetic order established at the onset of mineralisation. TEM images from the teeth post mineralisation are shown in **Figure** S3 and S4. The TEM images show differences in the magnetite growth direction at the base of the tooth compared to the tip which is consistent with the magnetic images. However, based on the TEM images alone, it is not possible to determine whether there is any magnetic order in the mineralisation process. The zoomed in section of the tip and mid-section

from tooth 1 provides images of individual magnetite nanoparticles which are of order 30-60 nm. As described below, at room temperature, magnetite nanoparticles of this size are ferrimagnetic and provide static magnetic signals which can be measured using the ODMR imaging protocol.

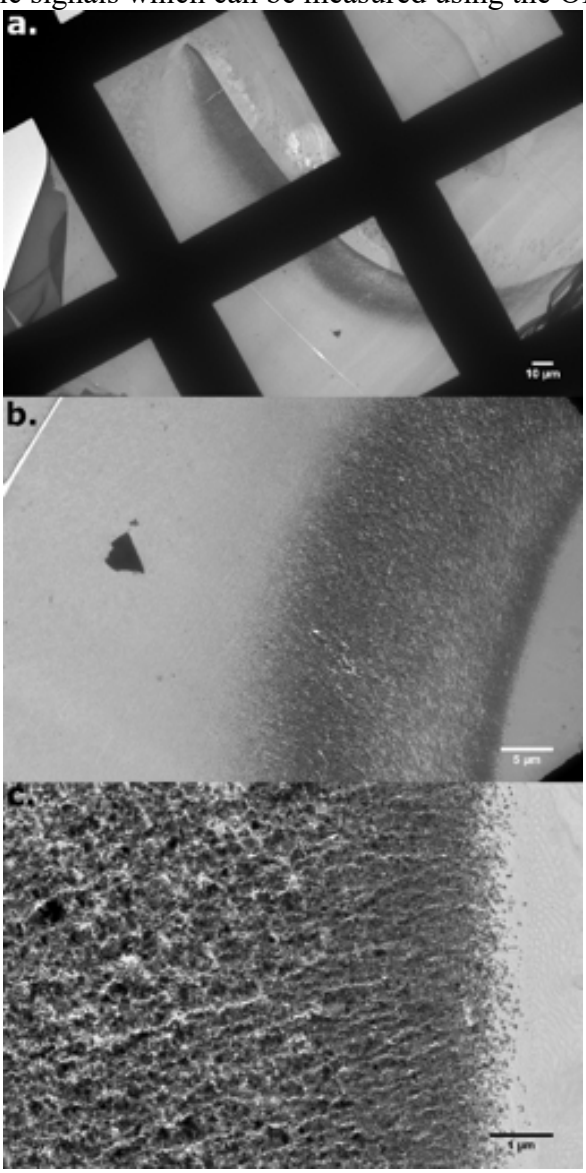

Figure S3| Transmission electron microscopy of tooth 4. **a**, Whole sagittal section of tooth cusp, scale bar 10 µm. **b**, Posterior face, showing magnetite band, scale bar 5 µm. **c**, Posterior face, tip region, showing magnetite grains. scale bar 1 µm.

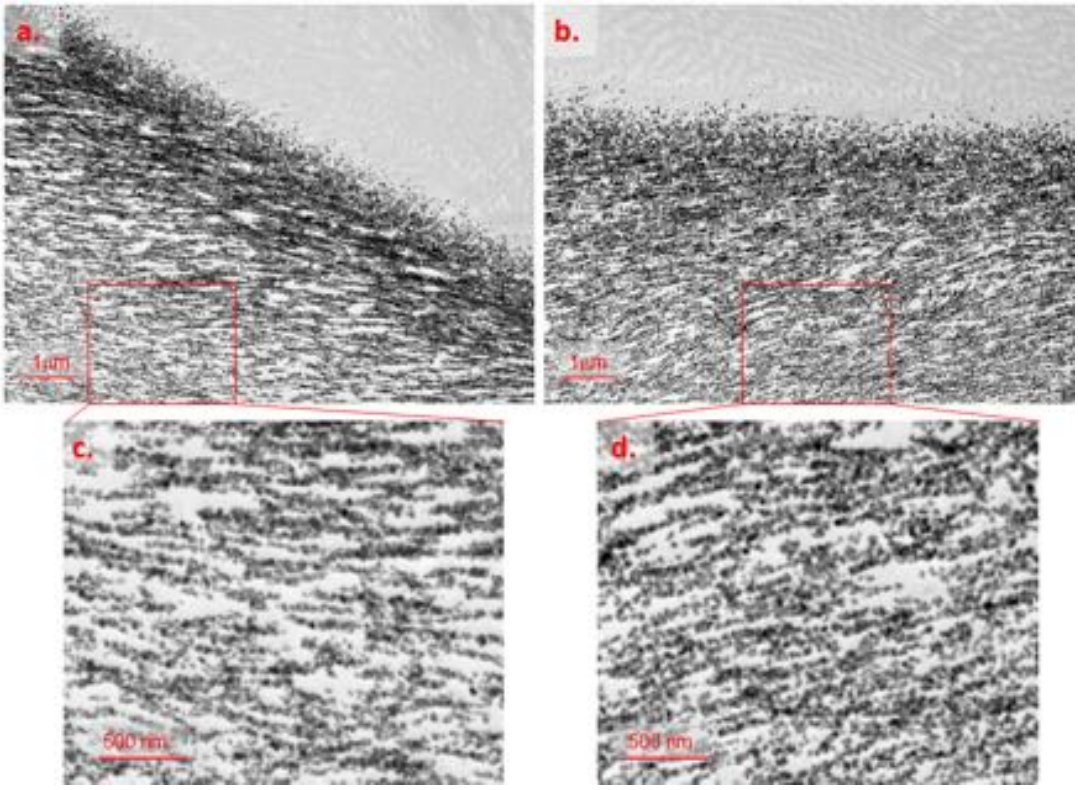

Figure S4| Transmission electron microscopy of tooth 4. **a**, **b**, Sagittal sections of tooth cusp of tooth 1. **c**, Zoomed in region of the posterior face, tip region showing discrete magnetite nanoparticles with a minimum particle size ~ 30 nm. **d**, Zoomed in region of the posterior face, mid-section of the tooth cusp.

Magnetic signals from iron biominerals

The two magnetic imaging modes used in this study are each sensitive to different magnetic signals – static and fluctuating. This allows imaging to distinguish between superparamagnetic ferrihydrite and ferrimagnetic magnetite.

Magnetisation of superparamagnetic particles reverse their direction along their easy axis after exponentially distributed waiting times:

$$f(x;\gamma) = \begin{cases} \gamma e^{-\gamma x}, & x \geq 0 \\ 0, & x < 0 \end{cases} \qquad (1)$$

where the x values are the realisations of the time between reversal events, and $\gamma = \frac{1}{\tau}$ is the mean time between these events.

For a superparamagnetic particle of volume V, anisotropy K, and temperature T, this time is defined by the Nèel relaxation time, τ, and is given by[39]

$$\tau = \tau_0 e^{KV/k_bT} \quad (2)$$

These parameters are known for magnetite and ferrihydrite, being

$$K_{magnetite} = 1.3 \times 10^4 \text{ Jm}^{-3}, t_0 = 10^{-9} \text{ s} \quad (3)$$
$$K_{ferrihydrite} = 3.5 \times 10^4 \text{ Jm}^{-3}, t_0 = 10^{-12} \text{ s}$$

Therefore, we can plot the Nèel relaxation time or magnetisation lifetime at room temperature as a function of particle size for both ferrihydrite and magnetite as shown in **Figure** S5.

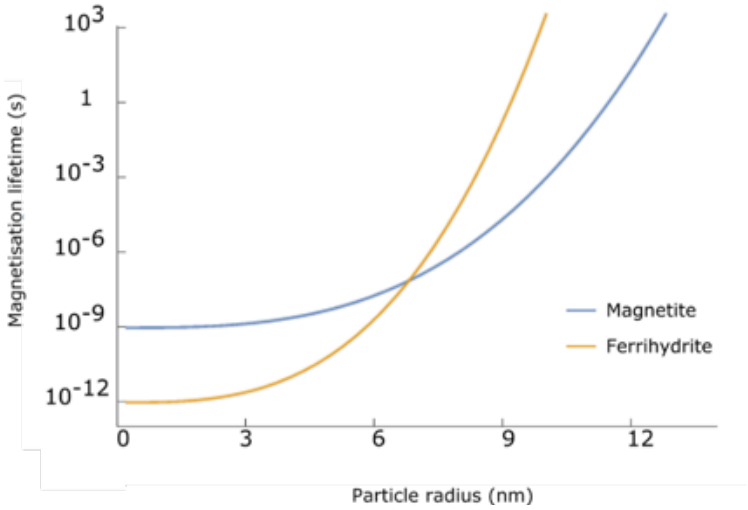

Figure S5| Magnetisation lifetime as a function of particle radius for magnetite and ferrihydrite. Blue line depicts the exponential growth in magnetisation lifetime of magnetite with particle size, while the orange line shows a similar dependence for ferrihydrite. Note: ferrihydrite nanocrystals in chiton teeth do not exceed 5 nm in radius therefore remain superparamagnetic with magnetisation lifetimes in the tens of picoseconds.

Equation (1) defines the auto-correlation function of the particle's magnetisation, so its Fourier transform is the frequency spectrum, which is a Lorentzian distribution:

$$f(x; x_0, \gamma) = \frac{1}{\pi\gamma}\left[\frac{\gamma^2}{(x - x_0)^2 + \gamma^2}\right] \quad (4)$$

where the x values are the frequency realisations. x_0 is the mean frequency.

For magnetite and ferrihydrite nanoparticles, we may take x_0 as equal to zero, as the single-domain nanoparticles are bistable fluctuators. (Additionally, for γ to be sufficiently broad to be relevant for zero-field T_1 spectroscopy, it is necessary that $\gamma >> x_0$, so it is acceptable to take x_0=0 in our case.) This gives the frequency spectra for magnetite and ferrihydrite:

$$S_{m,f}(\omega) = \frac{1}{\pi\gamma}\left[\frac{\tau^{-2}}{\omega^2 + \tau^{-2}}\right] \quad (5)$$

where τ is the respective Nèel relaxation time.

To detect the presence of these fluctuating superparamagnetic particles, we use the T_1 relaxation rate of the NV center, which is increased when coupled to such particles. Particles will couple when there is overlap between the spectra of their fluctuation frequencies and the filter function of the NV center. The filter function of the NV is given by:

$$f(\omega) = \frac{\Gamma_2}{4(\Gamma_2^2 + (\omega - \omega_0)^2)} \quad (6)$$

The amount of overlap is determined by the NV transition frequency, $\omega = D - B_0$, and the width of the spectrum as determined by the particle size (plotted against $\frac{\omega}{2\pi}$ at zero field: $B_0 = 0$.)

The relaxation rate is then given by the convolution of the spectra of the particles' fluctuation frequencies and the filter function of the NV:

$$\frac{1}{T_1} = \int_{-\infty}^{\infty} f(\omega) S(\omega) d\omega = \frac{B_x^2(\gamma + \Gamma_2)}{2((\gamma + \Gamma)^2 + \omega_0^2)} \approx \frac{B_x^2}{2\gamma} \quad (7)$$

where the approximation holds only if $\gamma \gg \omega_0, \Gamma_2$.

This is the case for ferrihydrite particles > 6 nm (**Figure** S6), and never the case for magnetite; see **Figure** S7).

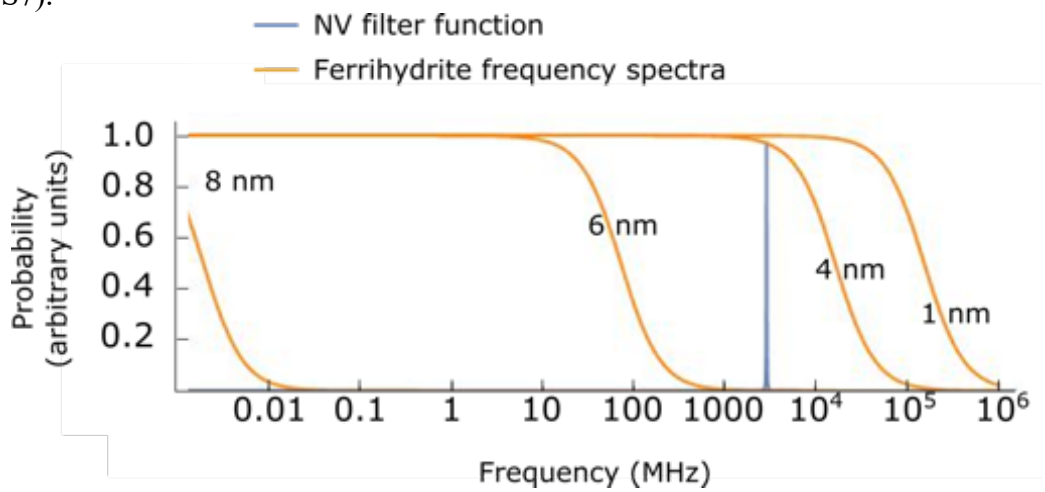

Figure S6| Probability of magnetic relaxation of ferrihydrite as a function of particle radius. Orange line depicts the Lorentzian distribution of magnetic fluctuation frequencies at particle radii of 1,4,6 and 8 nm. The blue line shows the NV filter function at zero magnetic field, i.e. 2870 MHz. There is strong overlap between the NV and ferrihydrite nanoparticles with radii less than 4 nm which is typical for ferrihydrite nanoparticles found in chiton.

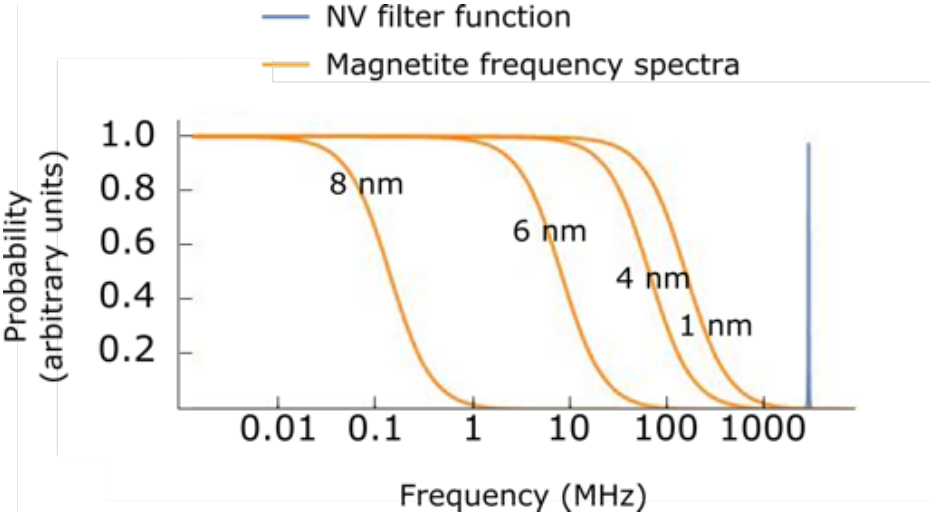

Figure S7| Probability of magnetic relaxation of magnetite as a function of particle radius. Orange line depicts the Lorentzian distribution of magnetic fluctuation frequencies at particle radii of 1,4,6 and 8 nm. The blue line shows the NV filter function at zero magnetic field, i.e. 2870 MHz. There is no overlap with the NV filter function even for particle radius of 1 nm. Therefore, magnetite will not exhibit any fluctuating magnetic signal that can be measured via quantum resonance microscopy at zero magnetic field. Note: The TEM images shown in Figure S3 and S4 indicate the magnetite nanoparticles form the onset of mineralisation are >30 nm with extremely long magnetic lifetimes.

If the NV center is coupled to many particles, this expression is averaged over the particle size, $P(R)$, and the total coupling summed over all couplings to individual particles. For a given pixel, this is predominantly determined by the iron density in that pixel. This analysis shows how NV T_1 sensing is, conveniently, sensitive to ferrihydrite magnetic fluctuation frequencies but not those of magnetite.

References

[1] J.-P. Tetienne, D. A. Broadway, S. E. Lillie, N. Dontschuk, T. Teraji, L. T. Hall, A. Stacey, D. A. Simpson, L. C. L. Hollenberg, *Sensors* **2018** 18, 1290.

[2] Gossuin Y, Gillis P, Hocq A, Vuong QL, Roch A., *Wiley Interdisciplinary Reviews: Nanomedicine and Nanobiotechnology* **2009** 1, 3.

In addition, we have looked at the structure of the stylus, the structure that connects the tooth to the radular belt. This may provide insights into the role of this structure not only for supporting the tooth, but also as a means of chemical transport. We used a combination of μ-CT imaging,

optical and electron microscopy, as well as elemental analysis, to show that the stylus is a highly contoured tube, mainly composed of alpha-chitin fibers, with a complex density distribution. Nanoindentation reveals regiospecific and graded mechanical properties that can be correlated with both the elemental composition and material distribution. Finite element modeling shows that the unique macroscale architecture, material distribution and elemental gradients have been optimized to preserve the structural stability of this flexible, yet robust functionally-graded fiber-reinforced composite tube, providing effective function during rasping. Understanding these complex fiber-based structures offers promising blueprints for lightweight, multifunctional and integrated materials. The following paper was submitted and is in review.

Radular Stylus of *Cryptochiton stelleri*: A Multifunctional Lightweight and Flexible Fiber-Reinforced Composite

Anna Pohl[1,2*], Steven A. Herrera[1*], David Restrepo[3,4], Ryo Negishi[5,6], Jae-Young Jung[7,8], Chris Salinas[1], Richard Wuhrer[9], Tomoko Yoshino[5,6], Joanna McKittrick[7], Atsushi Arakaki[5,6], Michiko Nemoto[10], Pablo Zavattieri[3], and David Kisailus[1,2#]

1. Materials Science and Engineering Program, University of California, Riverside, USA
2. Department of Chemical and Environmental Engineering, University of California, Riverside, USA
3. Lyles School of Civil Engineering, Purdue University, West Lafayette, USA
4. Department of Mechanical Engineering, The University of Texas at San Antonio, USA
5. Division of Biotechnology and Life Science, Institute of Engineering, Tokyo University of Agriculture and Technology, Tokyo, Japan
6. Institute of Global Innovation Research, Tokyo University of Agriculture and Technology, Tokyo, Japan
7. Materials Science and Engineering Program, University of California, San Diego, USA
8. Department of Orthopaedic Surgery, University of California, San Francisco, USA
9. Advanced Materials Characterization Facility, Western Sydney University, Australia
10. Graduate School of Environmental and Life Science, Okayama University, Okayama, Japan

* Co-first authors

Corresponding author
David Kisailus: david.k@uci.edu

Highlights

- Chitons have a complex tooth-stylus-belt multifunctional system
- We analyzed the kinematics of the stylus during rasping
- The stylus was found to be lightweight and has a complex multi-regional morphology
- Our study identifies the structure-function relationship of the stylus

Abstract

Chitons are herbivorous invertebrates that use rows of ultrahard magnetite-based teeth connected to a flexible belt (radula) to rasp away algal deposits growing on and within rocky outcrops along coastlines around the world. Each tooth is attached to the radula by an organic structure (stylus) that provides mechanical support during feeding. However, the underlying structures within the stylus, and their subsequent function within the chiton have yet to be investigated. Here, we investigate the macrostructural architecture, the regional material and elemental distribution and subsequent nano-mechanical properties of the stylus from the Northern Pacific dwelling *Cryptochiton stelleri*. Using a combination of μ-CT imaging, optical and electron microscopy, as well as elemental analysis, we reveal that the stylus is a highly contoured tube, mainly composed of alpha-chitin fibers, with a complex density distribution. Nanoindentation reveals regiospecific and graded mechanical properties that can be correlated with both the elemental composition and material distribution. Finite element modeling shows that the unique macroscale architecture, material distribution and elemental gradients have been optimized to preserve the structural stability of this flexible, yet robust functionally-graded fiber-reinforced composite tube, providing effective function during rasping. Understanding these complex fiber-based structures offers promising blueprints for lightweight, multifunctional and integrated materials.

Graphical abstract

Keywords

Mollusk, biocomposite, force transduction, flexible

1. Introduction

Multifunctional materials are in high demand for aerospace, automotive and biomedical industries. Such engineered structures often need to be lightweight, flexible, and tough, as well as have integrated features such as utility at high temperature or in aqueous environments, exhibit biocompatibility, or demonstrate self-healing. In many of these systems, hybrid structures that demonstrate multiple functions utilize materials with dissimilar properties. However, material failure often occurs at the interfaces between two dissimilar materials. Thus, finding an effective and reliable way to integrate dissimilar materials is a challenge (Thomopoulos et al., 2013).

Often, dissimilar material properties can be integrated by using composite materials. Fiber-reinforced composites and functionally graded materials are two common types of composites (Chung, 2010; Kar, 2016). Fiber-reinforced composites offer exceptional strength-to-weight ratios and an anisotropic structure, which can be used to increase stiffness in a preferred direction (Mallick, 2007). However, many fiber-reinforced composites are limited by the lack of control over microstructure, interfaces, and often undergo delamination (Caprino, 1984). Furthermore, integration of multiple materials into region-specific locations in composite materials still proves challenging. In functionally graded materials, two or more dissimilar materials are gradually merged and thereby incorporate different properties into one component (Pompe et al., 2003; Udupa et al., 2014). Graded composites have advantageous physical properties and are used for various applications requiring resistance to contact deformation (Chung and Das, 2008; Krumova, M, Klingshirn, C et al., 2001; Suresh, 2001), temperature-based deformation (Shao, 2005) and offer biological compatibility via coupling with ceramic or metallic implants (Pompe et al., 2003). While structurally and functionally advantageous, the manufacturing of composite materials is often complicated and requires numerous production steps.

Nature presents various effective examples of integration of different materials in hierarchically assembled, multifunctional architectures (Gorb, 2008). Thereby, failure mechanisms are circumvented and various functions are enabled. Furthermore, many biological materials are lightweight, biocompatible and often function in aqueous environments. These natural systems have evolved over hundreds of millions of years under ambient conditions and with a limited selection of materials. Many biological structures incorporate both fiber-reinforcement as well as structural and chemical gradients in order to reduce interfacial stresses that exist between materials with significantly different material properties (Naleway et al., 2015). In biomineralized structures, such as arthropod cuticles, mollusk shells, and bone (Grunenfelder et al., 2014a; Meyers et al., 2008; Meyers et al., 2013; Weaver et al., 2012; Yaraghi et al., 2016), the inorganic, stiff and hard minerals (e.g., calcium carbonate and phosphate, silica, iron oxide) are deposited around, or on flexible fibrous organic materials such as cellulose, collagen, keratin or chitin. In fact, non-mineralized biological composites such as fibrocartilage in ligaments of human femurs exist (Moffat et al., 2008). These flexible structures must balance bending and buckling resistance without significantly adding mass (Meyers et al., 2013). This combination of different material properties and the hierarchical assembly of inorganic and organic components results in materials with outstanding properties (Huang et al., 2019).

A group of organisms that produces unique multifunctional composite materials are chitons, herbivorous mollusks that live in the coastal zones worldwide, where they graze on rocks with a tongue-like organ (radula) to feed on algae growing on and inside these rocks (Brooker and Shaw, 2012; Kirschvink and Lowenstam, 1979; Lowenstam and Weiner, 1989; Nemoto et al., 2012; Nesson and Lowenstam, 1996; Wang et al., 2013). Due to their stiff and ultrahard teeth (modulus of 90 - 125 GPa and hardness 9 - 12 GPa) (Grunenfelder et al., 2014b; Weaver et al., 2010), chitons rasp away parts of the rock to access food, thereby undercutting and forming the mushroom-like rock formations (Figure 1A, inset). The radula of chitons contains three primary components that fulfill different functions: (i) ultrahard teeth that are capped with a magnetite layer, each of which are attached to (ii) a semi-flexible, yet stiff, stylus that provides force transduction to the teeth, and (iii) a long and flexible belt that provides a substrate upon which tens of rows of teeth are supported. Hence, the tooth-stylus-belt radular system of chitons is an exceptional example for the integration of dissimilar materials into a multifunctional structure.

Here, we investigate the macrostructural features and subsequent mechanics of the stylus from one such chiton, *Cryptochiton stelleri* (Figure 1A). This species lives in the North Pacific Ocean and is one of the largest and well-characterized chiton species (Ricketts et al., 1985; Towe and Lowenstam, 1967; Wang et al., 2013; Weaver et al., 2010). The radula of *C. stelleri* consists of a ribbon-like membrane that supports about 80 rows of tricuspid teeth that advance from infancy at the posterior end to fully mineralized mature teeth at the anterior end (Figure 1B). Similar radular structures have been observed in other chiton species (Brooker and Shaw, 2012; Macey and Brooker, 1996). The teeth are arranged in two rows of major lateral teeth positioned on either side of the flexible radula membrane (Figure 1C) and are supported by adjacent marginal teeth.

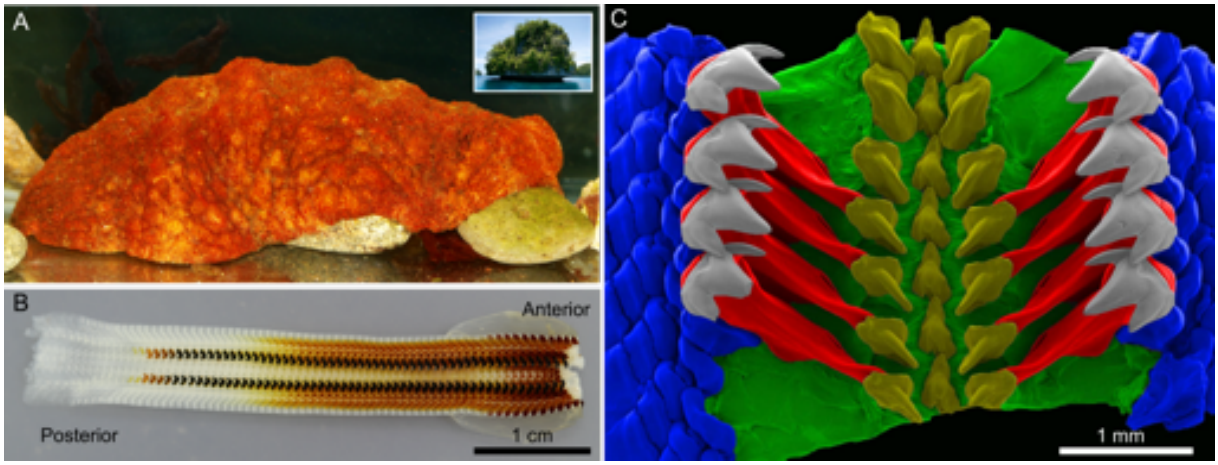

Figure 1. The tooth-stylus-belt system of chitons is a prime example of a naturally occurring multifunctional composite that demonstrates coupling of dissimilar materials. A. Cryptochiton stelleri is an herbivorous marine mollusk found in the coastal zone of the North Pacific. Inset: mushroom-shaped rock formed by the rasping action of chitons. B. The chiton radula consists of a ribbon-like membrane that houses about 80 rows of teeth at different stages of mineralization (the anterior end contains most mature teeth). C. False colored SEM micrograph showing four rows of mature teeth (at the anterior end of the radula) used in grinding rock. Two rows of major teeth are positioned on either side of the flexible radula membrane. The major lateral teeth (grey) are attached on the proximal end by styli

(red) to the radula membrane (green) and are adjacent to marginal teeth (yellow and blue).

The teeth, and thus styli, experience extensive repeated mechanical loading during rasping. Hence, the styli need to provide mechanical support and force transduction to the teeth in order for the chiton to feed. However, the morphological and microstructural features that afford this unique structure, both flexibility and stiffness, have yet to be reported. Previous results as well as scanning electron microscopy (Figure S1) reveal that the stylus is composed of continuous alpha-chitin fiber sheets that propagate from the leading edge of the stylus through the junction zone into the tooth (Wang et al., 2013; Weaver et al., 2010). Investigation of a stylus from a different species of chiton suggested an additional role as an ion transport pathway during biomineralization (Shaw et al., 2009). Here, we reveal the structure-mechanical function relationships in the stylus using a combination of video analyses, X-ray micro-computed tomography (μ-CT), nanoindentation and energy-dispersive X-ray spectroscopy (EDS). The experimental findings were implemented in finite element (FE) simulations, which identified the stress distribution in the stylus due to different tooth tip loading directions during the rasping process. The outcomes of this study are promising for the design for next-generation lightweight, flexible composite materials useful for automotive, aerospace, biotechnological or medical applications.

2. Materials and Methods

2.1. Research specimen

Cryptochiton stelleri were obtained alive from Monterey Abalone Company (Monterey, USA). The rasping behavior of these chitons was observed by analyzing the videos taken while grazing on an acrylic tank of an artificial sea water system. The radulae were dissected from the chitons and subsequently serially dehydrated in EtOH (i.e., 10%, 30%, 50%, 70%, 80%, 90%, 100%, 100%, 100%, each for 10 min). The styli of *C. stelleri* were removed from the radula using tweezers and used for analysis by μ-CT, nanoindentation, EDS and electron microscopy.

2.2. μ-CT and 3D reconstruction

An intact tooth-stylus structure was scanned using X-ray micro-computed tomography (μ-CT) (Skyscan 1172, Bruker, USA). Serially dehydrated samples (as described in 2.1) were mounted to a 1 mm diameter steel pin using Loctite super glue liquid professional (Henkel, USA) and mounted on a chuck. For the scan, a rotation step size of 0.1125° and an exposure time of 10 sec was used. The acceleration voltage was 80 kV and the isotropic voxel size was 1.4 μm. The images and three-dimensional reconstructed models were developed using Amira software (Thermo Fisher Scientific, USA). After reconstruction, cross-sectional dimensions were determined by creating triangular mesh models and saved into a 3D file extension format of the virtual reality modeling language (as known as VRL or VRLM).

2.3. Nanoindentation

Polished cross-sections of the stylus were prepared for nanoindentation by embedding the dehydrated styli in an epoxy resin (System 2000 Laminating Epoxy Resin, Fiberglast, USA). The

specimens were cut using a low-speed diamond saw (TechCut 4™, Allied High Tech Products, USA) and polished with progressively finer grades of silicon carbide paper and diamond lapping films.

Nanoindentation was performed on a longitudinal cross-section and six transverse cross-sections at defined positions along the long axis of the stylus. The samples were tested under ambient conditions in air using TI-950 nanomechanical testing system (Hysitron, USA) with a cube corner tip at a peak displacement of 250 nm. The grid size was adjusted to the size of the respective cross-section and the distance between the indents was 20 µm. The unloading curve of each indent was used to calculate the hardness and reduced modulus following the Oliver Pharr method (Pharr et al., 2009). The resulting-modulus data were plotted using MATLAB.

2.4. EDS

Elemental mapping of polished cross-sections of the stylus were performed at 15 kV in a scanning electron microscope (Mira3, Tescan, Czech Republic) equipped with a dual detector energy dispersive spectrometer (QUANTAX 400, Bruker Nano GmbH, USA).

2.5. Computational models

To create the computational models, the data from the CT-scans were segmented using Amira (Thermo Fisher Scientific, USA). Based on differences in density, separate STL files were generated as well as an STL file of the whole tooth-stylus structure. The STL file was imported into Geomagic Wrap (3D Systems, USA) for cleaning and generation of surfaces. Then, the cleaned part was exported into an .igs file and imported into Abaqus (Abaqus/Standard, Dassault Systèmes Simulia Corp, USA) for mesh generation. Finally, using an in-house MATLAB file, the mesh information was correlated with the STL files corresponding to each of the individual regions for the selection of sets and assignment of material properties. The final model used for simulations consisted of 1,431,113 tetrahedral elements, and the behavior for each of the regions was assumed linear elastic. Simulations of the tooth rasping at 8 different directions (see Figure 5A) were performed using the commercially available finite element software (Abaqus) considering load control conditions. A maximum load of 1N was applied in each direction.

3. Results and discussion

3.1. The rasping behavior of *Cryptochiton stelleri*

Video analysis of the rasping behavior of *C. stelleri* revealed that during rasping, the chiton pulls the two rows of tricuspid teeth together like a zipper, as it pulls the entire radular membrane back into the buccal cavity (Figure 2). During feeding, an odontophore pushes the anterior end of the radula against a rocky substrate, then retractor muscles contract, pulling the radula along the substrate containing algal deposits, raking food into its mouth (Nesson and Lowenstam, 1996) (Figure 2A). A closer observation of the video suggests a differential loading on these teeth. The front of the tooth tip (leading edge) is loaded with the greatest mechanical load, but occasionally the tooth will snag on the substrate (i.e., rock or other surface) and rotate inwards towards the center of the radula (Figure 2A). The motion of the tooth and stylus during rasping was

schematically summarized using optical micrographs (Figure 2B). Here, only mechanical loading from bending and twisting are taken into account.

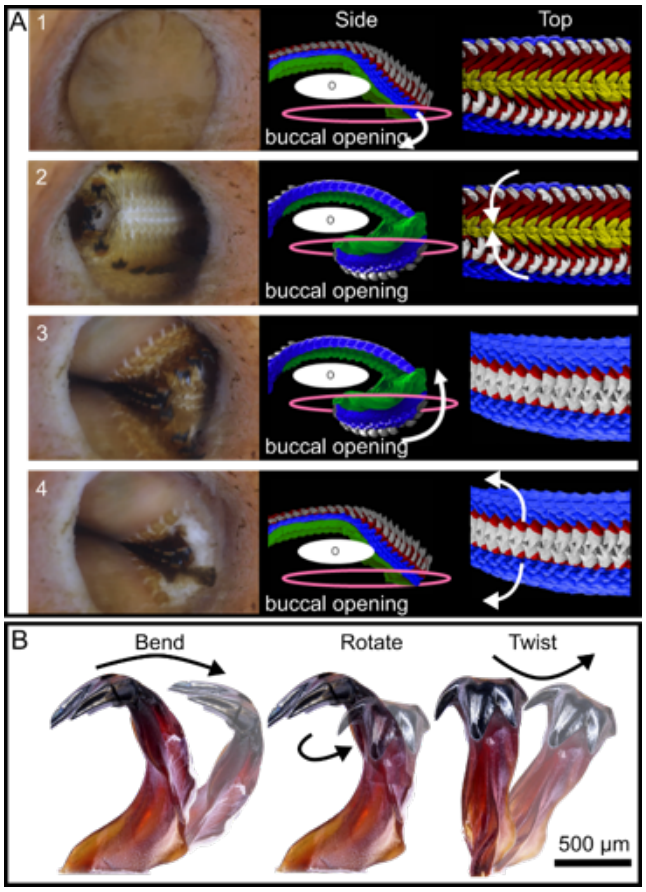

Figure 2. Rasping behavior of C. stelleri. A1. The radular membrane is a flexible support A2. that bends around an odontophore during feeding (white arrow). A3. Upon retraction through the buccal opening, the two rows of teeth are pulled together in a zipper-like manner, cutting through food and substrate alike. A4. Once retracted back into the mouth, the two rows of teeth can separate, releasing food and resetting the radula for the next rasping event. B. During retraction, the teeth are pulled together and scratching on the substrate causes a significant reorientation of the teeth. An overlay of optical micrographs shows that each tooth is loaded parallel to the long axis when the radula is pressed against the substrate, causing bending. Due to the 45˚ arrangement of major lateral teeth on the radular membrane, twisting occurs during retraction of the teeth into the mouth. The tooth is also able to rotate laterally as the flexible radula is bent around the odontophore during rasping.

The stylus is an essential part of the feeding system of chitons as it connects the ultrahard teeth with the flexible radular membrane and thereby enables the chiton to graze on rocky surfaces. Video analysis reveals the kinematics of the stylus during rasping and therefore helps to understand the direction of mechanical loading that is applied to the teeth. The rasping motion of *C. stelleri* is complex and involves four main steps. This leads to a complex distribution of positions in which different mechanical loads are applied to the teeth. This becomes more evident during feeding off of highly rough rocky substrates (Shaw et al., 2010), which yields a variation in tooth-rock contact and thus requires a flexible adaption. In order for the tooth to remove material from the substrate, adequate force must be applied through the stylus from the buccal musculature. Tensile forces must also be supported, as pulling, tearing, and ripping are

part of *C. stelleri*'s feeding behavior, demonstrated by whole branches of algae found in the animal's intestinal tract (Meeuse and Flügel, 1958). Structures that are bent predictably in a single direction are most resistant to bending when the mass is distributed far from the bending axis (Wainwright et al., 1982). Hence, the macromorphological architecture of the stylus and the tooth likely play an important role for effective rasping.

3.2. Macromorphological architecture

Optical and SEM micrographs (Figure 2B and Figure 3, inset) reveal that the styli of *C. stelleri* possess a complex macromorphological architecture. The stylus is a highly contoured cylinder-like structure, which, together with the tooth, resembles a 'C'-shape. Each stylus is approximately 1 mm long and 0.4 mm in diameter. Arrows in the inset from Figure 3 are used to highlight the directional motion referred in this study. The area of the stylus, which is connected with the radular belt is deemed the proximal end (bottom of the 'C'), whereas the top of the tooth is the distal end. The surface of the tooth that first makes contact with the substrate during rasping points towards the posterior end of the radular belt and is the leading edge of the tooth (inside of the 'C'). The opposite side towards the anterior end of the radular belt is the trailing edge of the tooth (backside of the 'C'). The side of the stylus and tooth that faces towards the center of the radular membrane is the medial side, while the side that faces the edge of the membrane is the lateral side.

µ-CT provides a detailed 3-dimensional macromorphological architecture of the stylus. The longitudinal section through the tooth and stylus as well as transverse cross-sections (perpendicular to the middle axis) at six different positions are shown in Figure 3. The results show that the stylus has a non-circular, cross-section that varies as a function of its length. In addition, the µ-CT scan highlights that the stylus is not completely solid, but rather a tube-like structure. A hollow pore canal is found at the core of the stylus, running from the radular belt at the lower stylus zone and terminating below the junction zone.

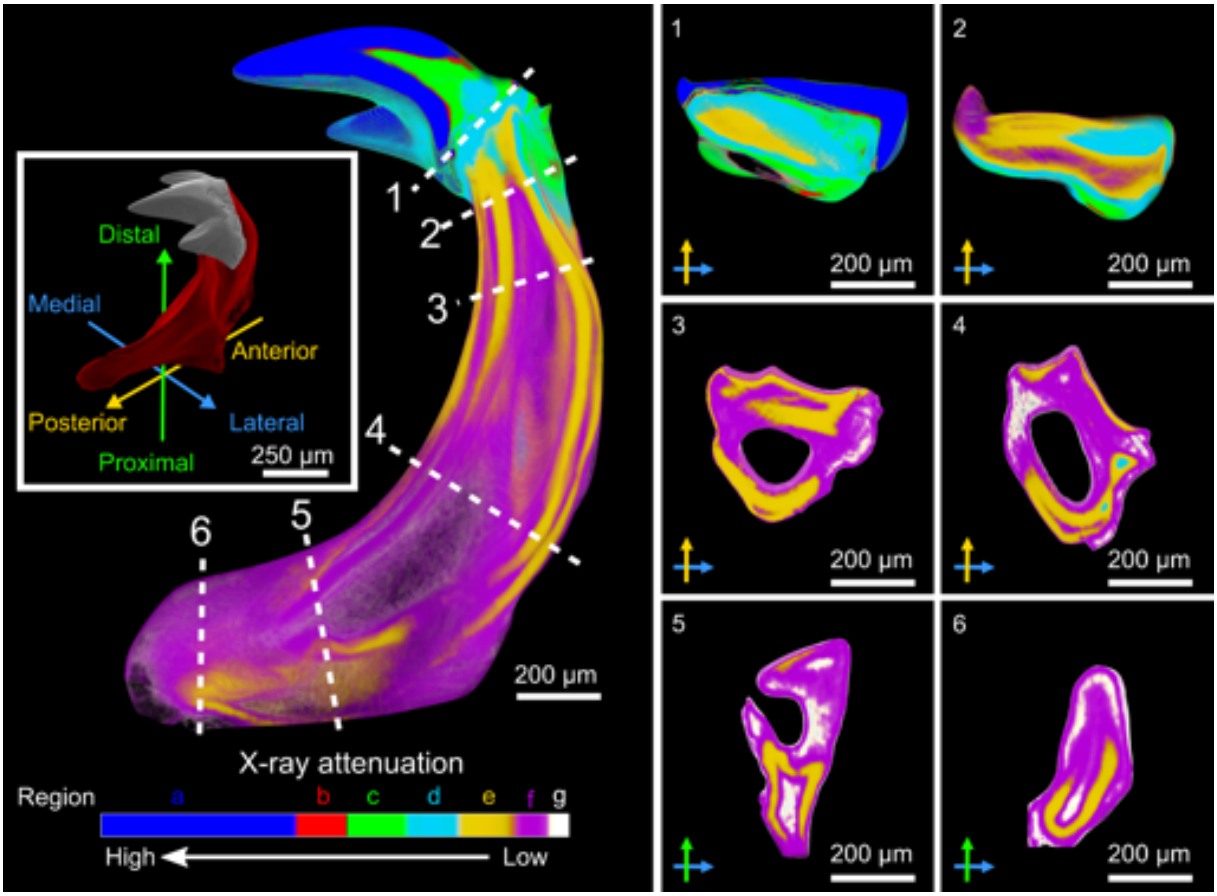

Figure 3. µ-CT scans reveal that the stylus is a non-circular cylinder (containing a large pore canal) with a varied cross-sectional shape along its long axis. (Left image) Longitudinal section through the mid-plane of a µ-CT scan of the stylus and tooth. Color bar identifies areas (a-g) of relative X-ray attenuation in the structure (blue and white are the highest and lowest attenuations, respectively). The inset shows the false colored SEM micrograph (grey is the tooth and red is the stylus). Colored arrows denote the orientation of the cross-sections with respect to the distal and proximal ends, the posterior and anterior directions and the medial and lateral orientations. 1-6: Transverse cross-sections were taken from different heights along the length of the stylus, as indicated in the longitudinal section (left).

The overall cross sections of each position (i.e., 1-6) are elongated. The centroid and second moment of area were calculated for each section to quantify the macroscopic morphology (Table 1). Based on these calculations, the stylus of the *C. stelleri* is found to twist along the length by 82˚. This is observed by comparing the orientation of the cross-sections at positions 1 and 5 (Figure 3). In addition, measurements (Table S1) show that the cross-sectional area of the stylus grows steadily from the proximal end (position 6) to the junction zone (position 1).

In order to provide mechanical support for the tooth, the macromorphology of the stylus is pivotal. The complex macromorphological architecture of the combined stylus-tooth structure resembles an arch, which distributes force throughout a larger volume of the structure, rather than concentrating the force at the tip (as observed in a straight morphology (van der Wal et al., 1999)). Curvature in mammalian bone, for example, can change axial compression to bending, increasing its functionality in response to multiple load directions. While a straight column can support axial loads of much greater magnitude than a curved column, this design jeopardizes the structure when bending predominates (Bertram and Biewener, 1988). Hollow beams are known

to be simultaneously flexible and robust against mechanical loading (Klein and Gänsicke, 2019). The highly contoured tubular shape of the stylus is optimized for this requirement as mass is only positioned where it is needed to fulfill the mechanical support function. Tubular structures consisting of materials with dissimilar properties are commonly found in Nature as they not only reduce weight, but also provide both stiffness and flexibility (Milwich et al., 2006; Zhao et al., 2010). For example, flying bird feathers are foam-filled cylinder-shaped lightweight materials tailored for withstanding mechanical load due to the aerodynamic drag during flying (Bachmann et al., 2012; Sullivan et al., 2016). In contrast, the pore canal in the stylus is open towards the proximal end of the stylus and is filled with body fluid and epithelial cells (Shaw et al., 2009). This not only reduces weight but may also minimize stress concentrations during rasping as the fluid can be released from the stylus into the surrounding epithelial tissue.

3.3. Nano-mechanical analysis

High-resolution nanoindentation mapping of polished longitudinal and transverse cross-sections (similar to those analyzed in µ-CT), reveal significant gradients in stiffness. Clearly, the longitudinal cross-section shows an increase in stiffness from the proximal end of the stylus, which is near the pore canal opening, to the distal region, which eventually is integrated through the junction zone, into the highly stiff tooth (Figure 4A). Interestingly, the stiffness of the "core" regions of the transverse cross sections is higher than those on the periphery in regions closer to the base of the stylus (i.e., proximal end), but is reversed (i.e., stiffer on the periphery) in regions 1 and 2 (approaching the junction zone). In fact, on the periphery of the junction zone, a region exists where the modulus values reach 23 GPa, which is close to the modulus of the chiton tooth core of 25 GPa (Weaver et al., 2010). This cross-section also shows cracking during sample preparation, which could be a sign for a remaining piece of tooth at the junction zone. The aforementioned observation is likely due to a combination of highly oriented, out of plane (from the transverse sections), and thus stiffer, alpha-chitin fibers located in the core of the stylus (Figure S1) and mineral that is likely being introduced into the tooth from the stylus. In fact, neat the distal end of the stylus, the modulus is significantly higher in the leading or trailing edges. The highest modulus was measured in the junction zone and appears to blend into the leading and trailing edges. This heterogenous modulus distribution and the region-specific nature of stiffness in the stylus contribute to the balance of stiffness and flexibility of the stylus.

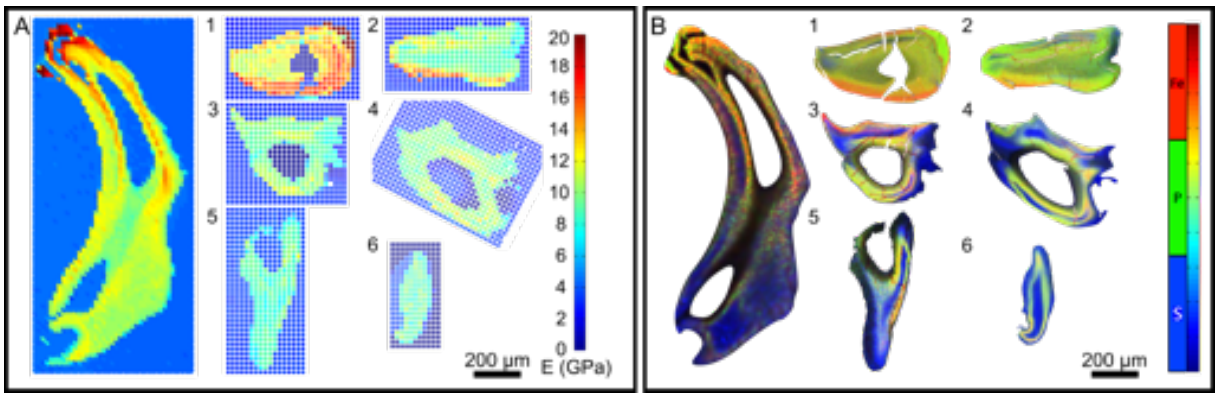

Figure 4. Nanoindentation reveals strong correlation between mechanical properties and composition hinting at the function of various specific elements found in the stylus. A. Nanoindentation on a longitudinal section and six

transversal cross-sections. This map shows a gradient along the length of the stylus, trending from 8 GPa in the lower stylus, to 23 GPa at the junction zone. Within transverse sections, the modulus can vary by 4 GPa within regions that are only 15 µm apart. Note: the maps are scaled to 20 GPa in order to enable comparison. Higher values are shown in darker red. B. EDS maps of the same longitudinal and transverse sections show that higher modulus values correlate with higher concentrations of iron and phosphorous. Lower modulus values correlate with a higher sulfur concentration and absence of iron and phosphorous.

Based on the nanoindentation experiments as well as the µ-CT scan data, the averaged reduced modulus (E_r) and the bending stiffness' (EI_x, EI_y) of the stylus at each cross-section position were calculated (Table 1).

Table 1. The information obtained by nanoindentation and µ-CT on the transversal cross-sections were used to calculate the averaged reduced modulus (E_r) and the bending stiffness (EI_x, EI_y) along the long axis of the stylus.

Cross-section	1.	2.	3.	4.	5.	6.
Averaged E_r (GPa)	18	16	15	14	12	12
E_{Ix}(Pa*m^4)	2.64E-07	1.47E-07	3.15E-07	1.92E-07	6.66E-08	2.98E-08
E_{Iy}(Pa*m^4)	9.71E-07	9.44E-07	4.69E-07	4.44E-07	4.08E-07	1.71E-07

One main function of the stylus is to anchor the tooth to the radula belt and thereby generate a connection between these two dissimilar materials. The stylus as a whole resembles a functionally graded material. SEM micrographs of the stylus showed, in addition, that alpha-chitin fibers run through the junction zone towards the tooth (Figure S1). Both, fibers and graded change in stiffness are enabling the strong attachment of the stylus to the tooth and the belt without generating sharp interfaces between the tooth and the stylus. Functional gradients combined with fiber-reinforced materials are a common principal in biological materials for the connection of dissimilar materials and reduce stress concentrations at the joint (Birman et al., 2013). The tooth attachment in the human periodontium, for example, includes two joints with graded stiffness: the connection between the alveolar bone and cementum and the interface between cementum and root dentin (Ho et al., 2007). These interfaces are also characterized by collagen fibers that run through the interface and form a fiber-reinforced material. Another example is the connection between tendon to bone (Thomopoulos et al., 2003). Here, the modulus changes in orders of magnitude within a small length scale and gradients in mineral content and fiber orientation were observed (Genin et al., 2009). A very steep gradient of mechanical properties was observed in the stylus, where the modulus changes from around 8 GPa to 23 GPa within the length of the stylus. A gradation in modulus, like that observed along the length of the stylus, has been shown to increase failure resistance dramatically in structural materials (Suresh, 2001). Stiffness is added to this structure due to ridges that appear at the leading and the trailing edges. In many biological and engineered structures, ridges are implemented and lead to higher stiffness (Klein and Gänsicke, 2019; Purslow and Vincent, 1978). Some examples include ridges of cortical material, which run along two-thirds of the avian feather rachis (Bachmann et al., 2012) and the junction of the spike and bulb in the stomatopod dactyl club (Weaver et al., 2012). Ridged structures in cacti have been found to increase the surface to volume ratio so as not to apply stress to the epidermis during swelling, while also increasing the flexure stiffness of higher aspect ratio plants (Mauseth, 2000). This

shows that the stylus has a complex multiscale morphology that is optimized not only for the attachment of the ultrahard tooth to the belt but also for mechanical support during rasping.

3.4. Regio-specific density distribution and elemental composition

In order to reveal the distribution of material in the stylus, X-ray attenuation data obtained by µ-CT were used (Davis et al., 2015; Davis et al., 2018; Gerward, 1993; Jackson and Hawkes, 1981). The color bar utilized in the µ-CT (Figure 3) correlates with the X-ray attenuation normalized to the density of the material. The density of magnetite is known to be 5.15 g/cm³ and represents the maximum attenuation (blue) while the density of air is 0.001225 g/cm³ and represents the minimum attenuation (black). Furthermore, the density of pure chitin is 1.425 g/cm^3. Starting from these values, the densities of the different regions within the tooth-stylus structure were interpolated. A typical phantom like X-ray imaging reference is not applicable for this high-density material. Thus, we interpolated the X-ray attenuation from known densities of the magnetite (upper end) and chitin (low end), respectively. These maps reveal seven (Figure 3, color bar a-g) spatially distinct regions of different density that run along the length of the stylus and into the tooth. These same regions coincide with those identified by nanoindentation and EDS.

The values for density obtained by X-ray attenuation in µ-CT scans and the moduli obtained by nanoindentation mapping show an overall gradient along the stylus long axis. The junction zone in the distal region, where the tooth is attached to the stylus is stiffer than the proximal region, where the stylus is attached to the flexible radula belt. In addition to this gradient, X-ray attenuation results show that there are distinct regions in which the mechanical properties are different due to different local material compositions. Furthermore, the bending stiffness' (Table 1) also show a similar trend, highlighting the fact that the stylus must be flexible enough to fold during retraction into the buccal cavity, while maintaining sufficient stiffness to transduce force to the tooth during rasping. The regions with higher densities are located closer to the junction zone and towards the trailing edge of the stylus, where a higher modulus is needed in order to enable mechanical support of the tooth. In contrast, the proximal regions of the stylus have a lower density and thereby are more flexible. Furthermore, the stylus is mainly composed of alpha-chitin fibers and proteins, with far less mineral than that in the tooth, and is thus less dense. In addition, the alpha-chitin fibers and proteins can provide stiffness. For example, chitin fibers partially combined with minerals are found in the exoskeletons of many marine organisms (e.g., crab, shrimp and squid) as well as in insects. These composite materials are both stiff and lightweight (Gunderson and Schiavone, 1989; Vincent and Wegst, 2004).

However, EDS was used to determine if spatially distinct elemental distributions in the chiton stylus affected the stiffness of the material in specific regions. The same polished sections used for nanoindentation mapping were utilized for elemental analysis (Figure 4B). In addition to C, O and N, varying quantities of Na, Cl, S, P, Ca, Mg, Fe, K, and Si were found (data not shown). Of these, we highlight iron, phosphorus and sulfur using false colored elemental X-ray maps: iron (red), phosphorus (green) and sulfur (blue). Longitudinal and transverse cross-sections reveal a strong correlation between the increase in reduced modulus and the presence of iron, phosphorous and sulfur. Although the stiffness is lower in the lower half of the stylus, the presence of sulfur likely provides a stiffening role via cross-linking of chitin fibers with proteins.

Iron and phosphorus, which are found in the tooth as mineral components (Weaver et al., 2010), are also present in the distal end of the stylus and are likely either amorphous or inorganic precursor species. In fact, transmission electron microscopy (TEM) and selected area electron diffraction (SAED) analysis of the stylus at the distal end reveals that there may be amorphous/nanocrystalline mineral present (Figure S1). This suggests that the stylus acts as a multifunctional structure that not only supports the tooth during rasping, but also enables iron and phosphorus transport, enabling biomineralization within the tooth.

3.5. Stress distribution in the stylus during rasping

The results obtained by μ-CT, X-ray attenuation and nanoindentation give insights to the macromorphological architecture and the local regiospecific mechanical properties of the stylus. These results reveal that the stylus is not a homogenous structure but has a higher modulus in the distal region and a lower modulus towards the proximal region. Within the tooth-stylus system, seven distinct regions with different material properties can be distinguished (Table S2). In order to understand the role of the varied regions within the stylus and to identify the stress distribution during the rasping process, finite element models (FEM) were used (Figure 5). Eight different rasping conditions were simulated (Figure 5A). The von Mises and pressure stress distributions are reported for cases 2, 6 and 8 (Figure 5B), while the linear stiffness was calculated as a function of loading direction (Figure 5C).

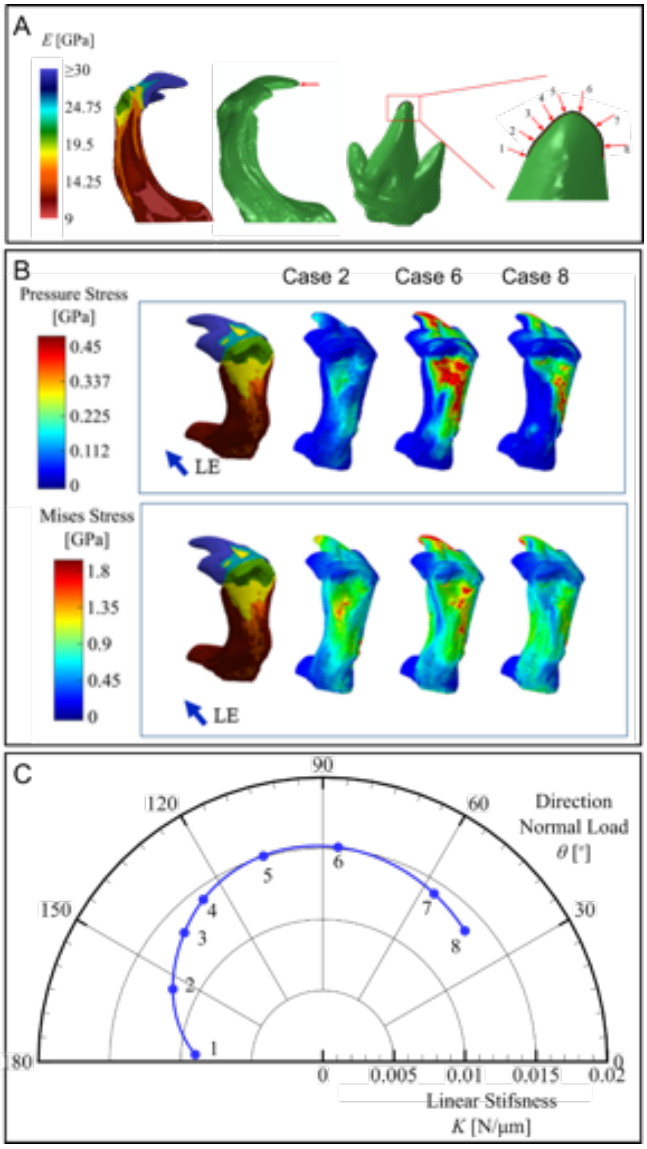

Figure 5. The effect of loading direction on stresses of a non-circular tube. Simulation of tooth tip loading direction variation during rasping, and the stylus stress concentrations: A. The diagram identifies loading directions for each case. Loading direction 1 applies force towards the medial direction. Loading direction 6 applies load to the tip of the tooth. Loading direction 8 applies force from the lateral direction. B. Pressure and von Mises Stress color maps for representative loading cases 2, 6 and 8. C. Linear stiffness as a function of the loading direction.

In addition, the stress distributions (Figure 6 and Figure S2) are compared with each of the cross-sections presented in Figure 4. The combination of the von Mises and pressure stress distributions provide information about the deviatoric and pressure components of the stress tensors for each loading condition. The von Mises and pressure stress maps in the structure show that the majority of stress is located in the shell of the tooth and the leading and trailing edges of the upper stylus (Figure 5B). Also, it is possible to identify that the maximum stress distribution is generally located directly along the leading and trailing edge surfaces in the upper stylus. However, the stress is shifted towards the medial (or midline) side at the tooth elbow due to the overall geometry and the marginal lateral tooth support on the distal side. The FE simulations

also show that larger stresses correlate with the same areas that have increased stiffness. Similar to other biological materials subjected to specific loading conditions, material distribution is not random but is likely organized to preserve the structural stability of the stylus during rasping (Figure S3).

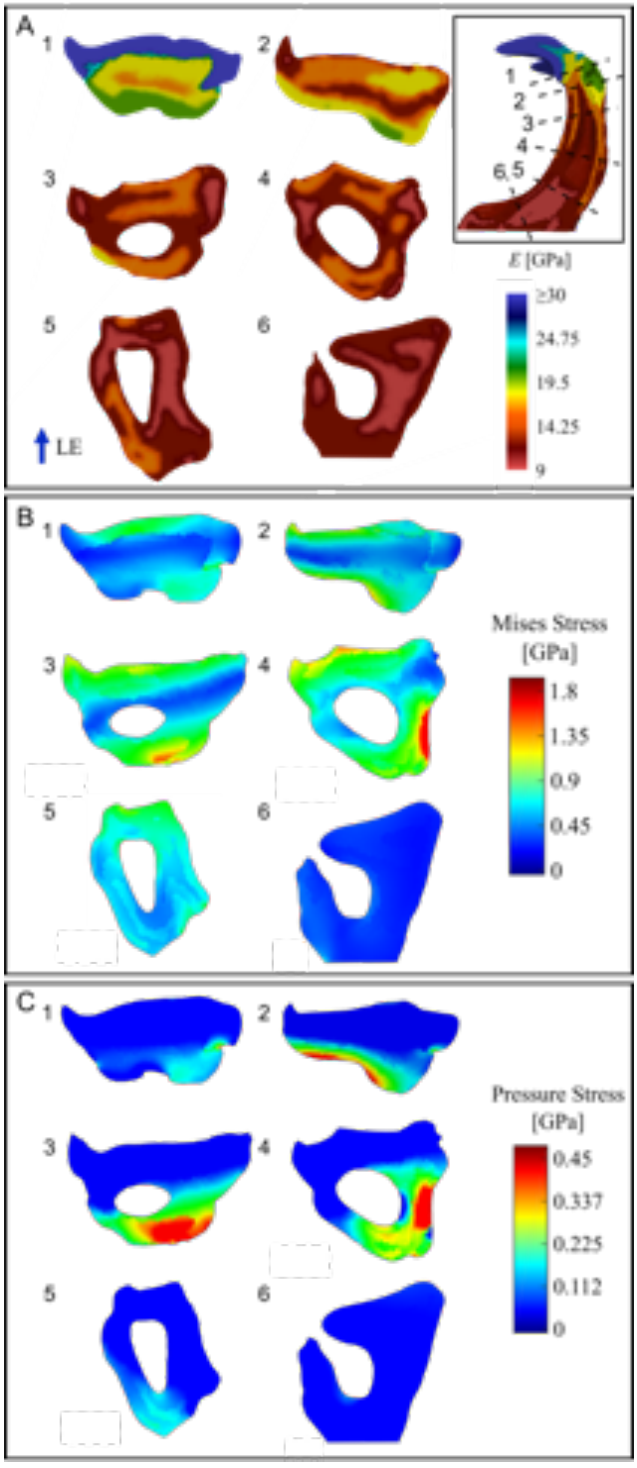

Figure 6. Comparison of stress distribution when a force is applied in case 6 (case 2 and case 8 are shown in Figure S2). A. Regio-specific distribution of the Elastic Modulus (E) along the stylus. B. Von Mises stress map. C. Pressure

stress map.

The results also show that the combination between shape and material distribution favor the loading directly at the tip of the tooth, or along the proximal direction. As loading deviates away from the tip (cases 2 and 8), the linear stiffness of the stylus decreases, which enables the stylus to freely rotate and bend as shown in the videos (see video file in supporting information, section S4). We hypothesize that this response allows for the safe release of the tooth during the rasping process, avoiding catastrophic damage. The finite element simulations show that the majority of stress is located in the same areas that have higher stiffness, primarily on the leading and trailing edges of the upper stylus. The stress is low towards the proximal end of the stylus because the marginal lateral tooth provides support and acts as a pivot point near the stylus elbow (Figure S4).

4. Conclusion and outlook

The stylus of *C. stelleri* is an example of a fiber-reinforced, functionally-graded structure that demonstrates effective integration of stiff and flexible components. With this combination of material properties, the stylus is able to maintain a firm connection between the soft radular belt and the ultrahard tooth cusp and transfers sufficient force from the radular musculature while minimizing the risk of catastrophic failure. The combination of high curvature and rotation of the major axis of its cross-section allows the stylus to delocalize stress during rasping events. Selectively denser regions in the upper stylus, enhanced by local fiber orientation parallel to its long axis and the presence of mineral components, provide both tensile and compressive strength to the leading edge and trailing edge, respectively. Utilizing the design principles provided by this multifunctional, flexible and lightweight natural composite may enable development of high-performance materials used in the medical, transportation, robotics, and defense industries.

5. References

Bachmann, T., Emmerlich, J., Baumgartner, W., Schneider, J.M., Wagner, H., 2012. Flexural stiffness of feather shafts: Geometry rules over material properties. Journal of Experimental Biology 215 (Pt 3), 405–415. DOI: 10.1242/jeb.059451.

Bertram, J.E.A., Biewener, A.A., 1988. Bone curvature: Sacrificing strength for load predictability? Journal of Theoretical Biology 131 (1), 75–92. DOI: 10.1016/S0022-5193(88)80122-X.

Birman, V., Genin, G.M., Thomopoulos, S. (Eds.), 2013. Structural interfaces and attachments in biology. Springer, New York, NY, XII, 388.

Brooker, L.R., Shaw, J.A., 2012. The chiton radula: A unique model for biomineralization studies, in: Seto J. (Ed.), Advanced Topics in Biomineralization. INTECH Open Access Publisher.

Caprino, G., 1984. Residual strength prediction of impacted CFRP laminates. Journal of Composite Materials 18 (6), 508–518. DOI: 10.1177/002199838401800601.

Chung, D.D.L., 2010. Composite materials: Science and applications. Springer, London, 371 pp.

Chung, H., Das, S., 2008. Functionally graded Nylon-11/silica nanocomposites produced by selective laser sintering. Materials Science and Engineering: A 487 (1-2), 251–257. DOI: 10.1016/j.msea.2007.10.082.

Davis, G.R., Evershed, A.N.Z., Mills, D., 2015. Characterisation of materials: Determining density using X-ray microtomography. Materials Science and Technology 31 (2), 162–166. DOI: 10.1179/1743284714Y.0000000618.

Davis, G.R., Mills, D., Anderson, P., 2018. Real-time observations of tooth demineralization in 3 dimensions using X-ray microtomography. Journal of Dentistry 69, 88–92. DOI: 10.1016/j.jdent.2017.11.010.

Genin, G.M., Kent, A., Birman, V., Wopenka, B., Pasteris, J.D., Marquez, P.J., Thomopoulos, S., 2009. Functional grading of mineral and collagen in the attachment of tendon to bone. Biophysical Journal 97 (4), 976–985. DOI: 10.1016/j.bpj.2009.05.043.

Gerward, L., 1993. X-ray attenuation coefficients: Current state of knowledge and availability. Radiation Physics and Chemistry 41 (4), 783–789. DOI: 10.1016/0969-806X(93)90326-P.

Gorb, S.N., 2008. Biological attachment devices: Exploring nature's diversity for biomimetics. Philosophical Transactions. Series A, Mathematical, Physical, and Engineering Sciences 366 (1870), 1557–1574. DOI: 10.1098/rsta.2007.2172.

Grunenfelder, L.K., Herrera, S., Kisailus, D., 2014a. Crustacean-derived biomimetic components and nanostructured composites. Small 10 (16), 3207–3232. DOI: 10.1002/smll.201400559.

Grunenfelder, L.K., Obaldia, E.E. de, Wang, Q., Li, D., Weden, B., Salinas, C., Wuhrer, R., Zavattieri, P., Kisailus, D., 2014b. Stress and damage mitigation from oriented nanostructures within the radular teeth of Cryptochiton stelleri. Advanced Functional Materials 24 (39), 6093–6104. DOI: 10.1002/adfm.201401091.

Gunderson, S., Schiavone, R., 1989. The insect exoskeleton: A natural structural composite. JOM 41 (11), 60–63. DOI: 10.1007/BF03220386.

Ho, S.P., Marshall, S.J., Ryder, M.I., Marshall, G.W., 2007. The tooth attachment mechanism defined by structure, chemical composition and mechanical properties of collagen fibers in the periodontium. Biomaterials 28 (35), 5238–5245. DOI: 10.1016/j.biomaterials.2007.08.031.

Huang, W., Restrepo, D., Jung, J.-Y., Su, F.Y., Liu, Z., Ritchie, R.O., McKittrick, J., Zavattieri, P., Kisailus, D., 2019. Multiscale toughening mechanisms in biological materials and bioinspired designs. Advanced Materials 31 (43), 1901561. DOI: 10.1002/adma.201901561.

Jackson, D.F., Hawkes, D.J., 1981. X-ray attenuation coefficients of elements and mixtures. Physics Reports 70 (3), 169–233. DOI: 10.1016/0370-1573(81)90014-4.

Kar, K.K.(E.), 2016. Composite materials: Processing, applications, characterizations. Springer Berlin Heidelberg, XVII, 686.

Kirschvink, J.L., Lowenstam, H.A., 1979. Mineralization and magnetization of chiton teeth: Paleomagnetic, sedimentologic, and biologic implications of organic magnetite. Earth and Planetary Science Letters 44 (2), 193–204. DOI: 10.1016/0012-821X(79)90168-7.

Klein, B., Gänsicke, T., 2019. Leichtbau-Konstruktion. Springer Fachmedien, Wiesbaden, XIV, 532.

Krumova, M, Klingshirn, C, Haupert, F., Friedrich, K., 2001. Microhardness studies on functionally graded polymer composites. Composites Science and Technology 61 (4), 557–563. DOI: 10.1016/S0266-3538(00)00228-1.

Lowenstam, H.A., Weiner, S., 1989. On biomineralization. Oxford University Press, 336 pp.

Macey, D.J., Brooker, L.R., 1996. The junction zone: Initial site of mineralization in radula teeth of the chiton Cryptoplax striata (Mollusca: Polyplacophora). Journal of Morphology 230 (1), 33–42. DOI: 10.1002/(SICI)1097-4687(199610)230:1<33:AID-JMOR3>3.0.CO;2-O.

Mallick, P.K., 2007. Fiber-reinforced composites: Materials, manufacturing, and design, 3rd ed. CRC Press, Hoboken, 640 pp.

Mauseth, J.D., 2000. Theoretical aspects of surface-to-volume ratios and water-storage capacities of succulent shoots. American Journal of Botany 87 (8), 1107–1115. DOI: 10.2307/2656647.

Meeuse, B., Flügel, W., 1958. Carbohydrases in the sugar-gland juice of Cryptochiton (Polyplacophora,

mollusca). Nature 181 (4610), 699–700. DOI: 10.1038/181699a0.
Meyers, M.A., Chen, P.-Y., Lin, A.Y.-M., Seki, Y., 2008. Biological materials: Structure and mechanical properties. Progress in Materials Science 53 (1), 1–206. DOI: 10.1016/j.pmatsci.2007.05.002.
Meyers, M.A., McKittrick, J., Chen, P.-Y., 2013. Structural biological materials: Critical mechanics-materials connections. Science (New York, N.Y.) 339 (6121), 773–779. DOI: 10.1126/science.1220854.
Milwich, M., Speck, T., Speck, O., Thomas Stegmaier, Heinrich Planck, 2006. Biomimetics and technical textiles: Solving engineering problems with the help of nature's wisdom. American Journal of Botany 93 (10), 1455–1465. DOI: 10.3732/ajb.93.10.1455.
Moffat, K.L., Sun, W.-H.S., Pena, P.E., Chahine, N.O., Doty, S.B., Ateshian, G.A., Hung, C.T., Lu, H.H., 2008. Characterization of the structure-function relationship at the ligament-to-bone interface. Proceedings of the National Academy of Sciences of the United States of America 105 (23), 7947–7952. DOI: 10.1073/pnas.0712150105.
Naleway, S.E., Porter, M.M., McKittrick, J., Meyers, M.A., 2015. Structural design elements in biological materials: Application to bioinspiration. Advanced Materials 27 (37), 5455–5476. DOI: 10.1002/adma.201502403.
Nemoto, M., Wang, Q., Li, D., Pan, S., Matsunaga, T., Kisailus, D., 2012. Proteomic analysis from the mineralized radular teeth of the giant Pacific chiton, Cryptochiton stelleri (Mollusca). Proteomics 12 (18), 2890–2894. DOI: 10.1002/pmic.201100473.
Nesson, M.H., Lowenstam, H.A., 1996. Biomineralization processes of the radula teeth of chitons, in: Kirschvink, J.L., Jones, D.S., MacFadden, B.J. (Eds.), Magnetite biomineralization and magnetoreception in organisms. A new biomagnetism. Springer, Boston, MA.
Pharr, G.M., Strader, J.H., Oliver, W.C., 2009. Critical issues in making small-depth mechanical property measurements by nanoindentation with continuous stiffness measurement. Journal of Materials Research 24 (3), 653–666. DOI: 10.1557/jmr.2009.0096.
Pompe, W., Worch, H., Epple, M., Friess, W., Gelinsky, M., Greil, P., Hempel, U., Scharnweber, D., Schulte, K., 2003. Functionally graded materials for biomedical applications. Materials Science and Engineering: A 362 (1), 40–60. DOI: 10.1016/S0921-5093(03)00580-X.
Purslow, P., Vincent, J.F.V., 1978. Mechanical properties of primary feathers from the pigeon. Journal of Experimental Biology 72 (1), 251–260.
Ricketts, E.F., Calvin, J., Hedgpeth, J.W., Phillips, D.W., 1985. Between pacific tides. Stanford University Press, 680 pp.
Shao, Z.S., 2005. Mechanical and thermal stresses of a functionally graded circular hollow cylinder with finite length. International Journal of Pressure Vessels and Piping 82 (3), 155–163. DOI: 10.1016/j.ijpvp.2004.09.007.
Shaw, J.A., Macey, D.J., Brooker, L.R., Clode, P.L., 2010. Tooth use and wear in three iron-biomineralizing mollusc species. The Biological Bulletin 218 (2), 132–144. DOI: 10.1086/BBLv218n2p132.
Shaw, J.A., Macey, D.J., Brooker, L.R., Stockdale, E.J., Saunders, M., Clode, P.L., 2009. The chiton stylus canal: An element delivery pathway for tooth cusp biomineralization. Journal of Morphology 270 (5), 588–600. DOI: 10.1002/jmor.10705.
Sullivan, T.N., Pissarenko, A., Herrera, S.A., Kisailus, D., Lubarda, V.A., Meyers, M.A., 2016. A lightweight, biological structure with tailored stiffness: The feather vane. Acta Biomaterialia 41, 27–39. DOI: 10.1016/j.actbio.2016.05.022.
Suresh, S., 2001. Graded materials for resistance to contact deformation and damage. Science (New York, N.Y.) 292 (5526), 2447–2451. DOI: 10.1126/science.1059716.
Thomopoulos, S., Birman, V., Genin, G.M., 2013. The challenge of attaching dissimilar materials, in: Birman, V., Genin, G.M., Thomopoulos, S. (Eds.), Structural interfaces and attachments in biology. Springer, New York, NY, pp. 3–17.

Thomopoulos, S., Williams, G.R., Gimbel J. A, Favata, M., Soslowsky, L.J., 2003. Variation of biomechanical, structural, and compositional properties along the tendon to bone insertion site. Journal of Orthopaedic Research 21 (3), 413–419. DOI: 10.1016/S0736-0266(03)00057-3.

Towe, K.M., Lowenstam, H.A., 1967. Ultrastructure and development of iron mineralization in the radular teeth of Cryptochiton stelleri (mollusca). Journal of Ultrastructure Research 17 (1), 1–13. DOI: 10.1016/S0022-5320(67)80015-7.

Udupa, G., Rao, S.S., Gangadharan, K.V., 2014. Functionally graded composite materials: An overview. Procedia Materials Science 5, 1291–1299. DOI: 10.1016/j.mspro.2014.07.442.

Vincent, J.F.V., Wegst, U.G.K., 2004. Design and mechanical properties of insect cuticle. Arthropod Structure & Development 33 (3), 187–199. DOI: 10.1016/j.asd.2004.05.006.

Wainwright, S.A., Biggs, W.D., Gosline, J.M., Currey, J.D., 1982. Mechanical design in organisms. Princeton University Press, 423 pp.

Wang, Q., Nemoto, M., Li, D., Weaver, J.C., Weden, B., Stegemeier, J., Bozhilov, K.N., Wood, L.R., Milliron, G.W., Kim, C.S., DiMasi, E., Kisailus, D., 2013. Phase transformations and structural developments in the radular teeth of Cryptochiton stelleri. Advanced Functional Materials 23 (23), 2908–2917. DOI: 10.1002/adfm.201202894.

Weaver, J.C., Milliron, G.W., Miserez, A., Evans-Lutterodt, K., Herrera, S., Gallana, I., Mershon, W.J., Swanson, B., Zavattieri, P., DiMasi, E., Kisailus, D., 2012. The stomatopod dactyl club: A formidable damage-tolerant biological hammer. Science (New York, N.Y.) 336 (6086), 1275–1280. DOI: 10.1126/science.1218764.

Weaver, J.C., Wang, Q., Miserez, A., Tantuccio, A., Stromberg, R., Bozhilov, K.N., Maxwell, P., Nay, R., Heier, S.T., DiMasi, E., Kisailus, D., 2010. Analysis of an ultra hard magnetic biomineral in chiton radular teeth. Materials Today 13 (1), 42–52. DOI: 10.1016/S1369-7021(10)70016-X.

Yaraghi, N.A., Guarín-Zapata, N., Grunenfelder, L.K., Hintsala, E., Bhowmick, S., Hiller, J.M., Betts, M., Principe, E.L., Jung, J.-Y., Sheppard, L., Wuhrer, R., McKittrick, J., Zavattieri, P.D., Kisailus, D., 2016. A sinusoidally architected helicoidal biocomposite. Advanced Materials 28 (32), 6835–6844. DOI: 10.1002/adma.201600786.

Zhao, L., Ma, J., Wang, T., Xing, D., 2010. Lightweight design of mechanical structures based on structural bionic methodology. Journal of Bionic Engineering 7 (4), S224-S231. DOI: 10.1016/S1672-6529(09)60239-0.

6. Acknowledgements

We acknowledge funding from the Air Force Office of Scientific Research, Award # FA9550-12-1-0249 and Award # FA9550-19-1-0286, and the Army Research Office, Award # W911NF1910347 and Award # W911NF-16-1-0208. We thank the Central Facility for Advanced Microscopy and Microanalysis at UC Riverside for providing electron microscopy equipment. R.N., T.Y., A.A. and D.K. also would like to thank to the support from Institute of Global Innovation Research (GIR) at TUAT.

Supporting information

S1. Microstructural analysis

S1.1. Scanning electron microscopy

Dehydrated (in ethanol to 100%) radula parts and styli were glued onto aluminum SEM pin mounts (12 mm diameter) covered with conductive carbon tape. In order to provide internal microstructural details, dehydrated styli were glued between two metal discs (atomic force microscopy specimen discs, 12 mm diameter, TED Pella, USA) using Loctite super glue liquid professional (Henkel, USA) and hardened overnight at room temperature. Subsequently, the metal disks were manually pulled apart to rupture the stylus and the resulting sections were attached to aluminum SEM pin mounts (12 mm diameter) via conductive carbon tape. All samples were sputter coated (Cressington 108 Auto, Cressington Scientific Instruments, UK) with a thin layer of palladium and platinum for 60 sec at 20 mA and subsequently imaged using a SEM (Mira3, Tescan, Czech Republic) operated at 10 keV.

S1.2. Transmission electron microscopy

In order to investigate localized fiber orientation of styli, chiton radulae were dissected from chitons, fixed in 2.5% glutaraldehyde, serially dehydrated in ethanol to 100% and critically point dried. Radula were then embedded in an epoxy resin (Fiberglast, USA), sectioned to 80 nm using an ultra-microtome (Leica, USA) with a diamond knife (45˚ MT, TED Pella, USA), and mounted on a TEM grid.

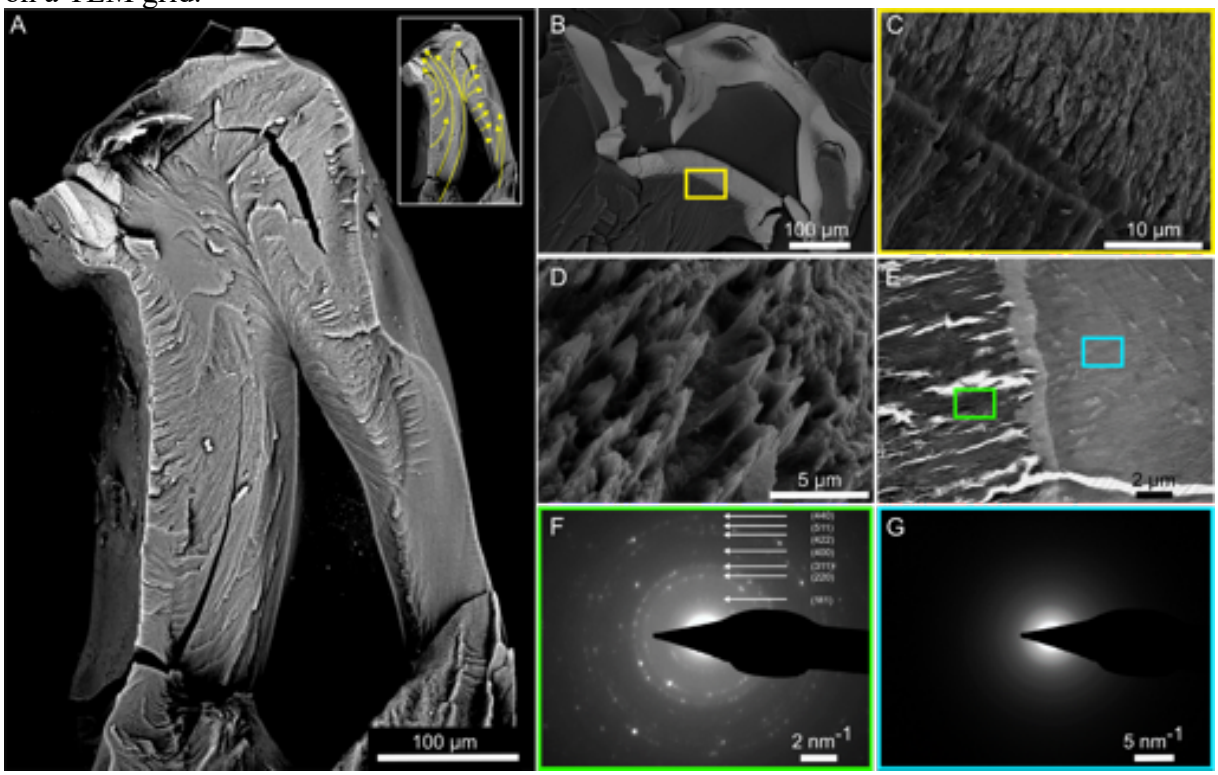

Figure S7. Electron microscopy of fractured or ultramicrotomed sections of the stylus reveal highly ordered fiber sheets with various orientations that contribute to the outstanding mechanical properties of the stylus and provide the base for the effective support of the teeth during rasping. A. Scanning electron micrograph of a longitudinally

fractured section along the mid plane of the stylus, with small remnants of the tooth present on the leading edge (higher contrast) at the junction zone. The inset of (A) maps the primary fiber directions in this cross section. B. Scanning electron micrograph of a coronal fractured surface of the tooth (at the junction zone), with residual mineral from tooth present. C. Higher magnification electron micrograph (from the yellow box in (B), highlighting fibers transcending the stylus and passing through the junction zone into the shell of the tooth. D. An electron micrograph of a transverse fractured surface at the junction zone showing highly oriented fibers passing through the junction zone and into the shell of the tooth. E. Transmission electron micrograph of an ultramicrotomed section revealing structural features on both sides of the junction zone. F. Selected area electron diffraction (SAED) from the green boxed region (inside the tooth) reveals a diffraction pattern indexed as crystalline magnetite while G., the SAED from the blue boxed region (inside the stylus), shows very faint diffraction rings, indicative of amorphous/nanocrystalline material. E.

S2. Additional analysis of μ-CT and X-ray attenuation information

Table S2. Transverse cross-sections obtained from the μ-CT scans were used to calculate the cross-sectional area (A), the second moment of area (I_x, I_y).

Cross-section	1.	2.	3.	4.	5.	6.
A (m^2)	0.0184	0.0161	0.0147	0.0134	0.0115	0.0084
I_x (m^4)	1.46E-17	9.18E-18	2.10E-17	1.37E-17	5.55E-18	2.48E-18
I_y (m^4)	5.40E-17	5.90E-17	3.13E-17	3.18E-17	3.40E-17	1.43E-17

Table S3. X-ray attenuation and nanoindentation data reveal seven different regions within the stylus with distinct densities and modulus. Region a is the magnetite shell of the tooth, which has the highest modulus and density, whereas region g is located at the proximal end of the stylus where the stylus is attached to the flexible radula belt. These values were used for the generation of the model used for FE simulations.

Region	a	b	c	d	e	f	g
Density (g/cm^3)	5.15	2.75	2.37	2.75	1.90	1.63	1.425
E_r (GPa)	70	25	20	18	16	12	9

S3. Additional finite element data

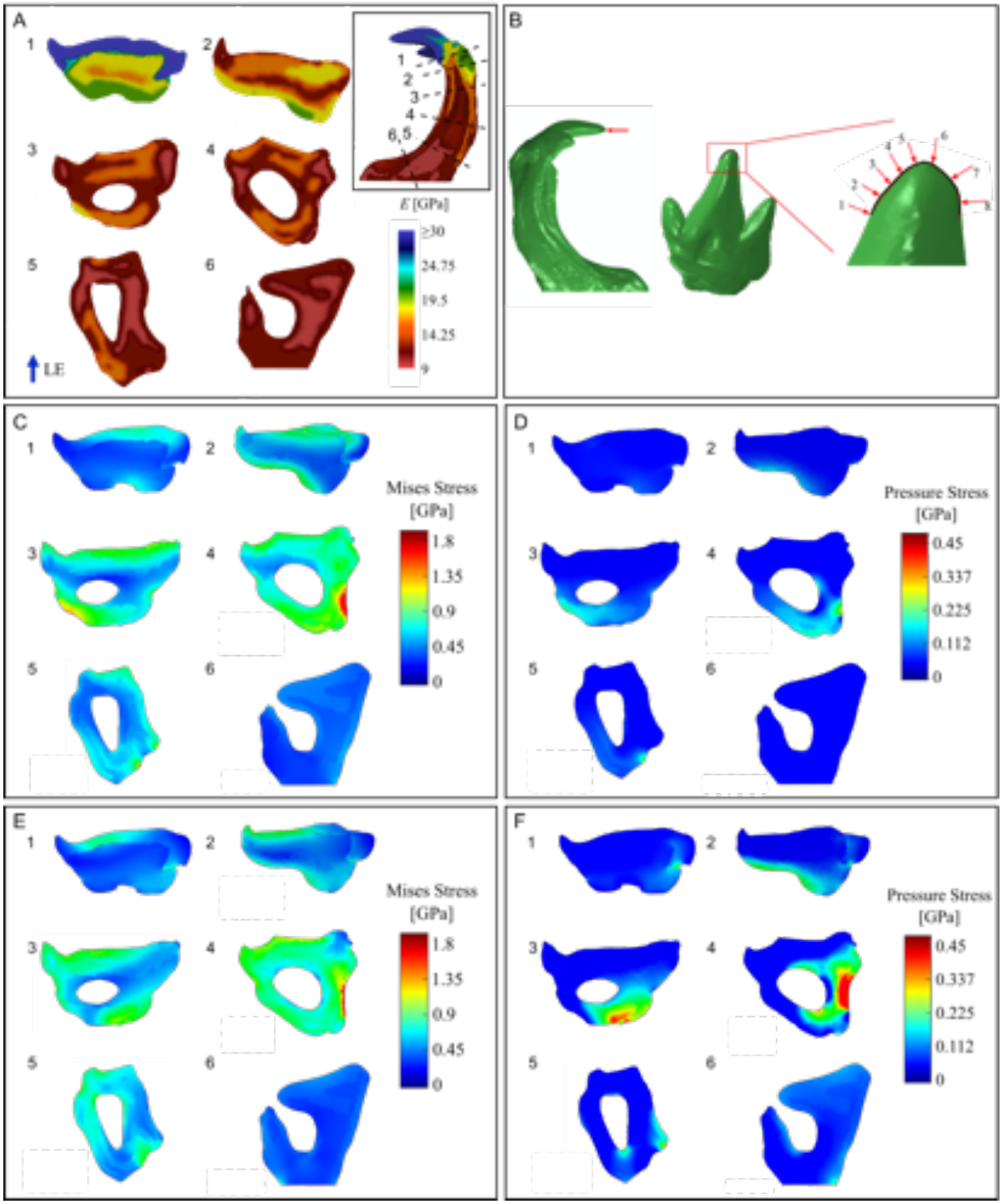

Figure S8. The effect of loading direction on stresses of a non-circular tube. Simulation of tooth tip loading direction variation during rasping, and the stylus stress concentrations: A. gives an overview of the FE model and the different cross-sections (1-6). B. The schematic shows loading directions for each case. Loading direction 1 applies force

towards the medial direction. Loading direction 5 applies load to the tip of the tooth. Loading direction 8 applies force from the lateral direction. C. and D. shows the cross-sections when force is applied in case 2 and E. and F. for case 8, respectively.

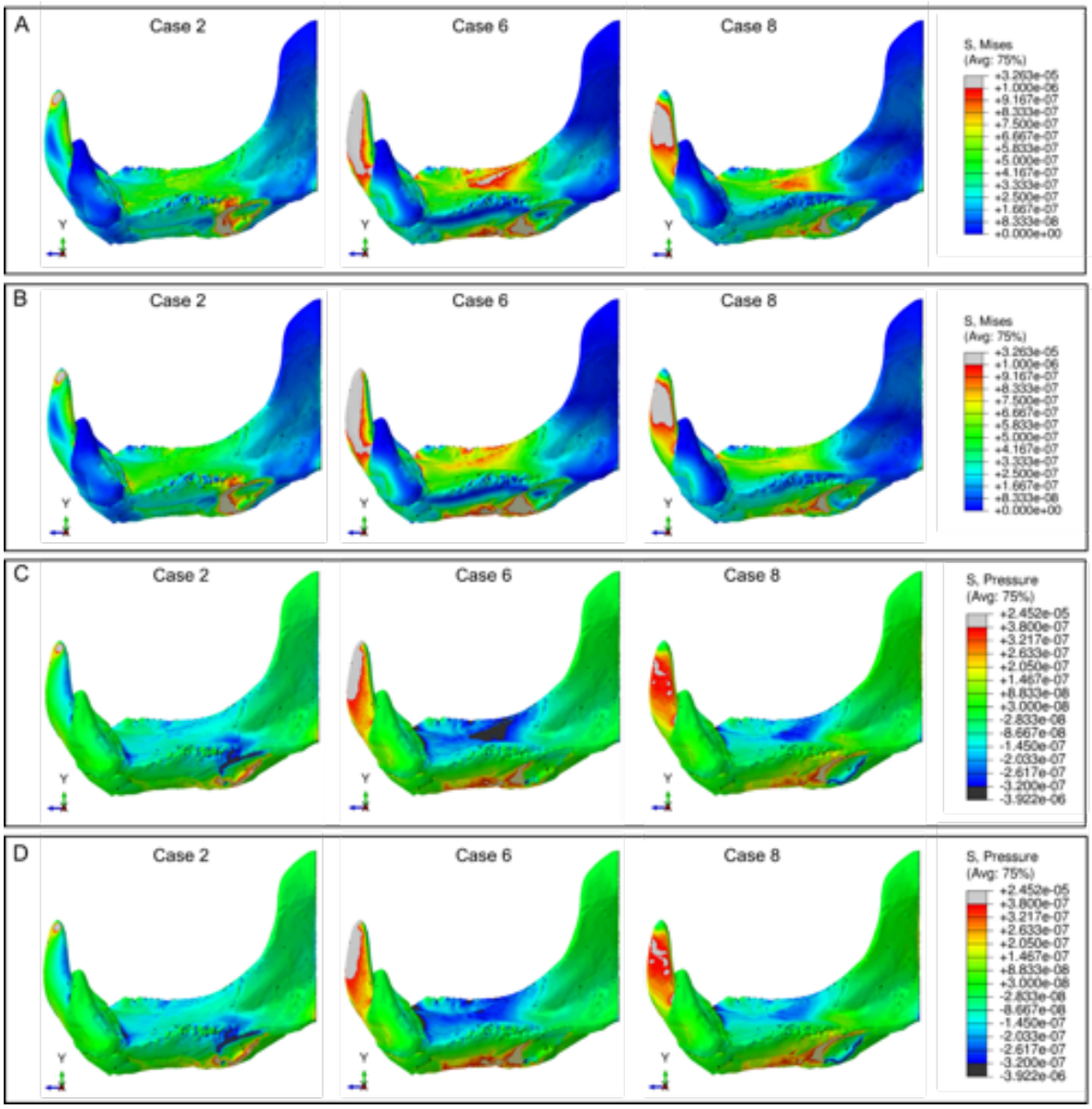

Figure S9. Comparison of the von Mises and pressure stress distribution in the stylus for A. and C. The model in which the material properties were distributed in the different distinct regions and B. and D. A model, which had homogenous material properties using an average E-modulus.

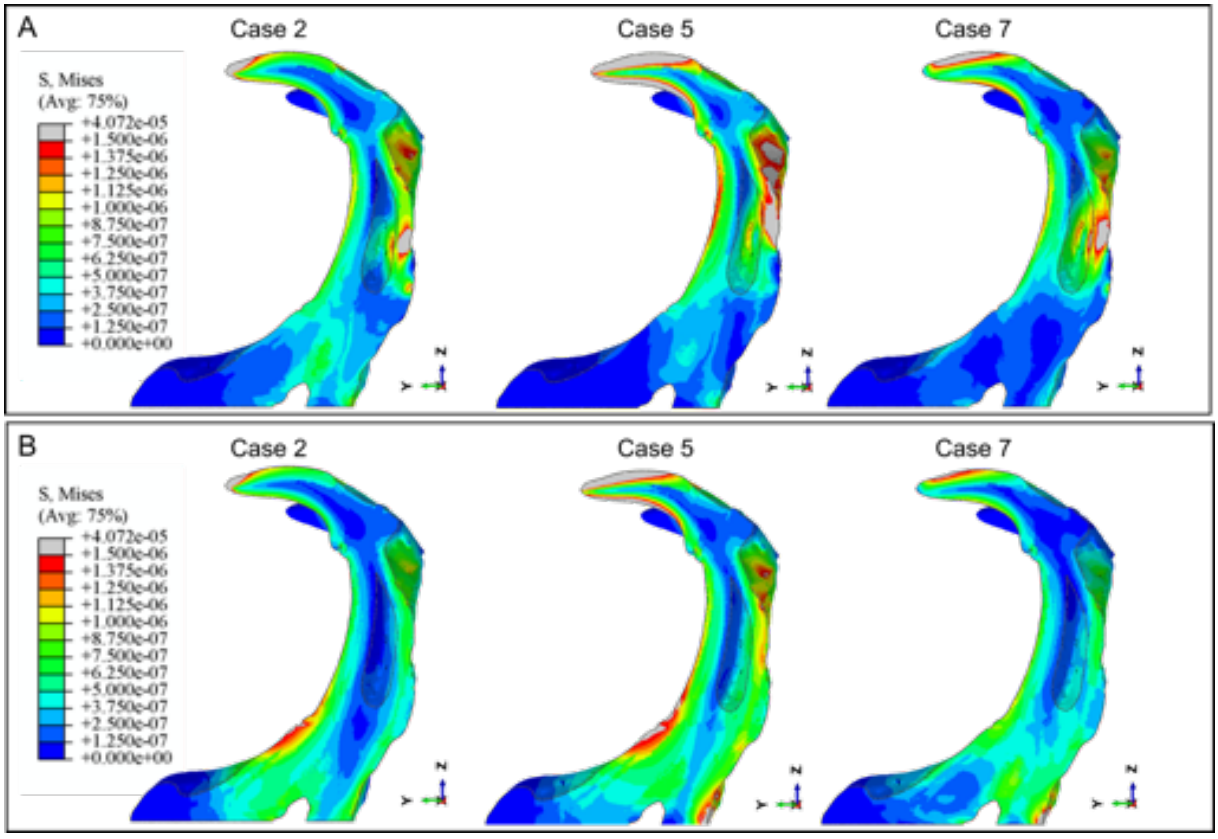

Figure S10. Differences in the Von Mises stress concentrations for a stylus, A. with and B. without the marginal teeth when a force is applied in cases 2, 5 and 7.

S4. Video analysis of *C. stelleri's* rasping behavior

The rasping behavior of these chitons was observed by analyzing the videos taken while grazing on an acrylic tank of an artificial sea water system.
Video file S4_Cstelleri_rasping-behavior.

Supported Personnel and Collaborations:
Training, Education, and Outreach Achievements

1. Mr. Taifeng Wang, was a Ph.D. student working on the project. He was mentored by Kisailus.

2. Dr. Anna Pohl was a postdoc partially supported on this project. She was mentored by Kisailus. We have had both high school and community college students tour our lab in the past year (until February 2020).

3. Julia M. McCoey and Robert W. de Gille were Ph.D. students who I helped to mentor during this project. They are at the University of Melbourne.

Dr. Michiko Nemoto is a former Kisailus post-doc and now a collaborator in this project. She is now a professor at Okayama University. She was mentored as a professor by Kisailus.

Dr. David Simpson and Dr. Lloyd Hollenberg are collaborators at University of Melbourne.

Dr. Jeremy Shaw is a collaborator at the University of Western Australia.

Dr. Omar Avila-Poveda is a collaborator at the Universidad of Sinaloa in Mexico.

Publications:

"Multiscale toughening mechanisms in biological materials and bioinspired designs," W. Huang, D. Restrepo, J.Y. Jung, F.Y. Su, Z. Liu, R.O. Ritchie, J. McKittrick, P. Zavattieri, D. Kisailus, Advanced Materials, 31 (43) (2019) 1901561. DOI: 10.1002/adma.201901561

"Quantum magnetic imaging of iron biomineralisation in teeth of the chiton *Acanthopleura hirtosa*," J. McCoey, M. Matsuoka, R. de Gille, L. Hall, J. Shaw, J.P. Tetienne, **D. Kisailus**, L. Hollenberg, D. Simpson, *Small Methods*, **4** (3) (2019) 2070010. DOI: 10.1002/smtd.201900754

One manuscript is in review:
"Radular Stylus of *Cryptochiton stelleri*: A Multifunctional Lightweight and Flexible Fiber-Reinforced Composite," Anna Pohl, Steven A. Herrera, David Restrepo, Ryo Negishi, Jae-Young Jung, Chris Salinas, Richard Wuhrer, Tomoko Yoshino, Joanna McKittrick, Atsushi Arakaki, Michiko Nemoto, Pablo Zavattieri, David Kisailus, *Journal of the Mechanical Behavior of Biomedical Materials*, ***in review.***

One additional manuscript is in preparation.

Presentations:

"Synthesis, Phase Transformation and Structural Development in Magnetic Biocomposites", **Invited talk.** Materials Research Society Spring Meeting, Phoenix, AZ, April 15, 2020.

"Biological Crystallization of Ultrahard Teeth and Translation to Multi-functional Materials", **Invited talk.** The Minerals, Metals and Materials Society Annual Meeting, San Diego, CA, February 26, 2020.

"Multiscale Architectures in the Exoskeletal Armor of a Crush Resistant Insect", **Invited talk.** The Minerals, Metals and Materials Society Annual Meeting, San Diego, CA, February 24, 2020.

"Biologically Inspired Multi-Functional Materials," **Invited seminar.** Lawrence Livermore National Labs. Livermore, CA. February 14, 2020.

"The Tooth-Stylus-Belt Radula System of Chitons: an Inspiration for Multimaterial and Multifunctional Structures," Gordon Research Conference on Multifunctional Materials. Ventura, CA. January 19-24, 2020.

"Phase Transformation of Iron-based Mineral in the Ultrahard and Wear-resistant Teeth of Cryptochiton Stelleri," Gordon Research Conference on Multifunctional Materials. Ventura, CA. January 19-24, 2020.

"Biological Synthesis and Mechanics of Ecologically Diverse Ultrahard Teeth of Chitons," **Invited talk.** 8th International Conference on Mechanics of Biological Materials. Waikoloa Beach, Hawaii. December 15 – 19, 2019.

"Biological Synthesis and Mechanics of Ecologically Diverse Ultrahard Teeth of Chitons," **Invited talk.** Joint Conference of the 12th International Marine Biotechnology Conference and the 12th Asia Pacific Marine Biotechnology Conference. Shizuoka, Japan. September 9 – 13, 2019.

"Biologically Inspired Multi-Functional Composites," **Invited talk.** 10th Pacific Rim International Conference on Advanced Materials and Processing (PRICM10). Xian, China. August 18-22, 2019.

"Biological Crystallization of Ultrahard Teeth and Translation to Multi-Functional Materials," **Invited talk.** 19th International Conference on Crystal Growth and Epitaxy (ICCGE-19). Keystone, Colorado, July 28–August 2, 2019.

"Biological Crystallization of Ultrahard Teeth and Translation to Multi-Functional Materials," **Invited talk.** Collaborative Conference on Materials Research. Seoul, South Korea. June 25-29, 2019.